SEARCH FOR EXOTIC MESONS IN $\pi^+\pi^-\pi^0$ DECAY

By

Ji Li

A Thesis Submitted to the Graduate

Faculty of Rensselaer Polytechnic Institute

in Partial Fulfillment of the

Requirements for the Degree of

DOCTOR OF PHILOSOPHY

Major Subject: Physics

Approved by the
Examining Committee:

Gary Adams, Thesis Adviser

Dennis Weygand, JLAB Adviser

Jim Napolitano, Member

Daniel Sperber, Member

Paul Stoler, Member

Rensselaer Polytechnic Institute
Troy, New York

December 2003
(For Graduation December 2003)

CONTENTS

LIST OF TABLES

LIST OF FIGURES

ACKNOWLEDGMENT

I would like to take this opportunity to thank all the people who have contributed to the success of this work and who have supported me over the past five years.

Great appreciation goes to Prof. Gary Adams for his financial support and guidance. Without his support, this work could not have been done. I would also like to express my gratitude to Dr. Dennis Weygand who has guided me through each step of this analysis. Great thanks also has to go to John Cummings and Dennis Weygand for providing the partial wave analysis program used in this work.

I have to thank Lei Guo and Mina Nozar for their excellent work in detector calibration and data processing, which paved the way to the success of this analysis. I would also like to thank them and my other friends at RPI, Matthew Bellis, Maurizio Ungaro and Minghui Lu, for the intriguing physics discussions we had and for the friendship they offered. Thanks, guys! I have to thank Paul Eugenio and Alexander Ostrovidov for providing me the FSU grid computing resource.

I would like to thank all the members of my graduate examination committee, the members of the CLAS collaboration and the staff in the physics department at RPI for their help over the years.

I have to thank my family for their support during my stay in the United States. And lastly, but most importantly, I have to thank my wife, Shiqin, for her love, sacrifice and support.

ABSTRACT

SEARCH FOR EXOTIC MESONS IN $\pi^+\pi^-\pi^0$ DECAY

Ji Li

December 2003

Directed by Professor Gary S. Adams

Results from a partial wave analysis on the $\pi^+\pi^-\pi^0$ system produced in the reaction $\gamma p \rightarrow p\pi^+\pi^-\pi^0$ with beam energy in the range [4.8, 5.5] GeV/c are presented. The data were collected in CLAS experiment E01-017(G6C) at the Thomas Jefferson National Accelerator Facility. The partial wave analysis showed photo-excitation of an $I^G J^{PC} = 1^-1^{-+}$ exotic isovector resonance. A mass dependent analysis was performed and yielded $M = 1690 \pm 5 \pm 7\, MeV/c^2$ and $\Gamma = 268 \pm 14 \pm 42\, MeV/c^2$ for this state. An exotic isoscaler signal with $I^G J^{PC} = 0^-2^{+-}$ was also seen in the partial wave analysis with $M = 2021 \pm 17 \pm 6\, MeV/c^2$ and $\Gamma = 184 \pm 25 \pm 26\, MeV/c^2$. A mass dependent fit was applied to other non-exotic signals as well, including $I^G J^{PC} = 1^-1^{++}$ and 0^-1^{--}. Resonance parameters were extracted for those states also.

CHAPTER 1
INTRODUCTION AND HISTORICAL REVIEW

1.1 The Standard Model

Over the past decades, tremendous progress has been made in particle physics. The *standard model*, formulated in the 1970s, has been firmly established based on a series of important discoveries. In the standard model, *leptons* and *quarks* are the most basic building blocks of the universe. There are six leptons and six quarks. Table 1.1 lists the fundamental fermions of the standard model.

Leptons	spin = 1/2		**Quarks**	spin = 1/2	
Flavor		**Charge**	**Flavor**		**Charge**
ν_e	electron-neutrino	0	u	up	2/3
e	electron	−1	d	down	−1/3
ν_μ	muon-neutrino	0	c	charm	2/3
μ	muon	−1	s	strange	−1/3
ν_τ	tau-neutrino	0	t	top	2/3
τ	tau	−1	b	bottom	−1/3

Table 1.1: Fundamental fermions of the Standard Model.

The standard model also comprises interactions between these constituent fermions. There are four types of interaction in nature: strong interactions, electromagnetic interactions, weak interactions and gravitational interactions. In the standard model, these interactions are described in terms of the exchange of mediating bosons, the *gauge bosons.* The basic interactions and their mediators are listed in table 1.2.

1.2 Strong Interaction, Color and Gluon

The strong interactions are responsible for binding quarks together to form *hadrons.* The hadrons are divided further into two categories based on their sta-

Interaction	Rel. Strength	Mediator
strong	1	gluon
electromagnetic	10−2	photon
weak	10^{-7}	$W^{\pm}, Z^0$
*gravity**	10^{-39}	graviton

Table 1.2: The interactions and gauge bosons. **Gravity* and the graviton are listed here for completeness even though they are *not* part of the standard model.

tistical properties: *baryons* which are fermions and *mesons* which are bosons. The strong interaction is a short-range force, its typical interaction range is on the order of one Fermi.

The strong interaction proceeds via mediating bosons called *gluons.* Like the photon, the gluon is a neutral, massless vector particle of spin-parity $J^P = 1^-$. However, the gluons differ from the photons greatly in that they can interact between themselves. The origin of this self-interaction is the *color* charges the gluons carry. In the theory of the strong force, *Quantum Chromodynamics(QCD)*, a quark carries one of three colors(say red, green and blue) and its antiquark carries the corresponding anti-color. The word *color* is just a name for an internal degree of freedom. Figure 1.1 (b) shows an example of the strong interaction between a red quark and a blue quark through the exchange of a blue-antired gluon. Since the gluons also carry color, they have self-interaction with triple(or quadruple) gluon vertices as shown in figure 1.1 (c). For comparison, figure 1.1 (a) shows the electromagnetic interaction between two electrons via one-photon exchange. Since the photon is electrically neutral, first order interactions between photons do not exist.

1.3 Symmetries and Groups

In this section, I will give a brief introduction to some of the concepts and terminology of group theory that are relevant to later discussion. Important symmetry relations in particle physics are also discussed.

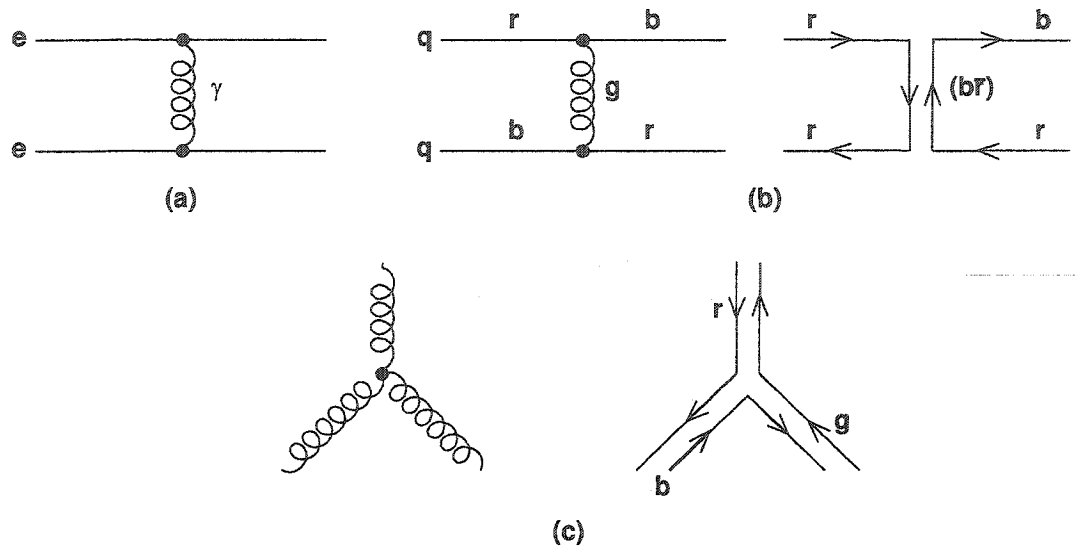

Figure 1.1: (a) Electromagnetic interaction by one-photon exchange. (b) Strong interaction by gluon exchange. The diagram on the right shows the flow of color. (c) Self-interaction of gluons.

1.3.1 The $SU(2)$ Group and Isospin

$SU(2)$ denotes the special unitary group in two dimensions. The rotation group serves as an excellent example of the $SU(2)$ group. The algebra of the $SU(2)$ group is the well-known commutation relation

$$[J_i, J_j] = \sqrt{-1}\epsilon_{ijk}J_k \tag{1.1}$$

where $\epsilon_{ijk} = 1(-1)$ if ijk are a cyclic(anti-cyclic) permutation and $\epsilon_{ijk} = 0$ otherwise.

Isospin is another example of $SU(2)$ symmetry. The idea of isospin came about because the proton and the neutron have almost exactly the same mass which suggests that they can be viewed as two manifestations of the same particle called the *nucleon*. The nuclear force does not distinguish the two. Each nucleon was then postulated to have isospin $I = \frac{1}{2}$, with $I_3 = \pm\frac{1}{2}$ for protons and neutrons respectively. For a composite nucleon-nucleon system, the total isospin can be either 1 or 0. Symbolically, one may write the decomposition of this system as

$$2 \otimes 2 = 3 \oplus 1 \tag{1.2}$$

that is to say, in the irreducible representation, it forms a triplet and a singlet. Isospin is approximately conserved for light quark hadrons. The significance of this invariance is that nuclear physics should be the same among the three members of the iso-triplet. This approximate symmetry of the strong interaction comes about because the perturbative masses of the up and down quarks are both small and approximately equal.

1.3.2 Finite Groups: P-, C- and G-parity

Finite groups by definition are groups which contain only finite number of elements. The finite symmetry groups that are of importance to our project are *parity*(P), *particle-antiparticle conjugation*(C) and *G-parity*(G). Each of these groups has only two elements, and the allowed eigenvalues for the corresponding operator are ± 1.

Parity is the reflection operation through the origin. Parity is conserved in strong and electromagnetic interactions. The weak interaction does not conserve parity.

C-parity, or charge conjugation, reverses the sign of the charge and magnetic moment of a particle, leaving all other coordinates unchanged. Therefore, C-parity brings a particle into its anti-particle and vise versa. Strong and electromagnetic interactions are invariant under the charge conjugation operation. Only neutral bosons can be C-parity eigenstates.

The physical meaning of G-parity is charge-conjugation(C) followed by a 180 degree rotation around the I_2 axis in isospin space [36].

$$G = e^{-i\pi I_2} C \tag{1.3}$$

The reason for introducing this concept is because charged particles are not C parity eigenstates. For instance, a C operation transforms $\pi^+(I_3 = 1)$ into $\pi^-(I_3 = -1)$.

$$C|\pi^+\rangle \rightarrow |\pi^-\rangle \neq |\pi^+\rangle \tag{1.4}$$

The rotation as described above transforms π^- back into π^+,

$$e^{-i\pi I_2}|\pi^-\rangle = \eta|\pi^+\rangle \tag{1.5}$$

where η is an arbitrary phase. G-parity is approximately invariant in strong interaction because it involves the isospin.

1.3.3 The $SU(3)$ Group and Color Symmetry

$SU(3)$ denotes the special unitary group in three dimensions. The fundamental representation of $SU(3)$ is a triplet. The three color charges mentioned in section 1.2 form a fundamental representation of the $SU(3)$ symmetry group. The generators may be taken to be eight linearly independent traceless hermitian 3×3 matrices. Conventionally, these matrices are denoted by $\lambda_i, i = 1, \ldots, 8$, known as the Gell-Mann matrices. The decomposition into the irreducible representation is an extension of equation (1.2) of the $SU(2)$,

$$3 \otimes \bar{3} = 8 \oplus 1 \tag{1.6}$$

that is the nine states divide into an octet and a singlet. Under $SU(3)$ operations, members of the octet transform among themselves but they do not mix with the singlet. The color $SU(3)$ symmetry of the strong interaction is assumed to be exact. Equation (1.6) will also be used to treat the meson decomposition in the flavor $SU(3)$ group to be discussed later.

1.4 QCD and Confinement

Quantum Chromodynamics(QCD) is a gauge field theory describing the color $SU(3)$ group. The gauge invariant Lagrangian of QCD can be written as [61]

$$\pounds_{QCD} = \bar{q}\left(i\gamma^\mu\partial_\mu - m\right)q - g\left(\bar{q}\gamma^\mu T_a q\right)G^a_\mu - \frac{1}{4}G^a_{\mu\nu}G^{\mu\nu}_a \tag{1.7}$$

where q is the colored quark wave function and the gluon field tensor G_μ takes the form

$$G^a_{\mu\nu} = \partial_\mu G^a_\nu - \partial_\nu G^a_\mu - g f_{abc} G^b_\mu G^c_\nu \tag{1.8}$$

Since the phase of the quark color fields can be changed arbitrarily yet the Lagrangian must remain invariant under these local phase transformations, a total of eight gluon fields is needed, i.e. a runs from 1 to 8. Also, local gauge invariance demands the gluons to be massless, just like the photons in QED.

The coupling constant of QCD, $\alpha_s = \frac{g^2}{4\pi}$, is a function of the four-momentum transfer Q^2. At short distances, corresponding to large Q^2, α_s is small and the strong interaction can be dealt with by perturbation methods. This property of the strong interaction is referred to as *asymptotic freedom.*

On the other side, decreasing Q^2 gives rise to a linear quark-quark potential, $V(r) \sim r$, which becomes so strong as the distance becomes larger that perturbation theory loses its validity. This linear potential binds the quarks and the gluons within the hadrons and leads to an astonishing phenomenon of QCD: *confinement.* The manifestation of QCD confinement in the physical world is that quarks and gluons are coupled only to color singlet states, i.e., no free quarks can be observed.

In situations involving only heavy quarks, this linear potential is usually manifested into the functional form [61, 82, 59]

$$V(r) = -\frac{4}{3}\frac{\alpha_s}{r} + kr \tag{1.9}$$

where $k \sim 0.18\,GeV^2$ is obtained from fitting to the data. This is the so-called static potential and it works relatively well for hadrons composed of heavy quarks. However mesons in the light quark sector, which is the primary topic of this project, are relativistic quantum systems and this manifestation does not apply. Because of the non-perturbative nature of QCD at large distances, simplified phenomenological models are necessary to study light mesons.

1.5 Constituent Quark Model and Light Meson Spectroscopy

Studies of the meson spectra via strong decays of hadrons provide valuable insight regarding QCD confinement. This has led to various phenomenological models such as the *constituent quark model.*

The study of hadrons using the constituent quark model follows the work of Gell-Mann [58] and Zweig [95]. At that time, only three quarks, namely $Up(u)$, $Down(d)$ and $Strange(s)$, were proposed. The constituent quark model assumes a many-body origin for the quark potential, yielding a constituent(quasi-particle) description. Thus each quark interacts with a phenomenological potential and has an effective mass that is larger than the quarks in the standard model. In the early quark model, all three flavors of quarks have similar mass, combined with the assumption that the strong interaction is indifferent to color, this introduces a symmetry within the light quark sector, normally referred to as flavor $SU(3)$[1].

In the constituent quark model, mesons are quark-antiquark bound states. For three flavors of quarks(and their antiquarks), one should expect families of mesons containing nine possible combinations of $q\bar{q}$ bound state(nonet). Recalling equation (1.6), we would expect to see the nonet decomposing into octet and singlet. This decomposition is illustrated in figure 1.2.

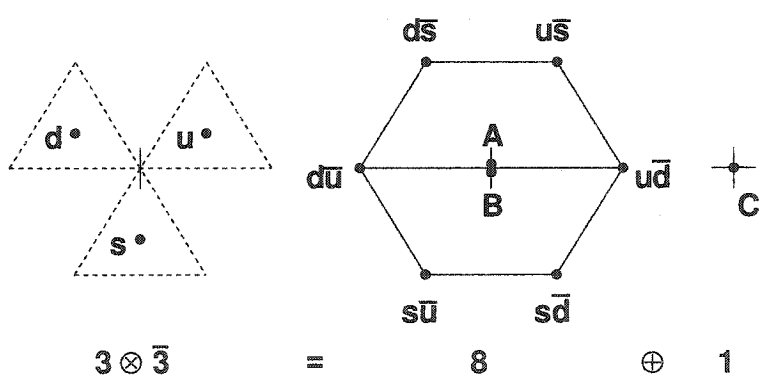

Figure 1.2: The flavor SU(3) decomposition of the light meson nonet in the $I_3 - Y$ plane. $A = \sqrt{\frac{1}{2}}(u\bar{u} - d\bar{d})$, $B = \sqrt{\frac{1}{6}}(u\bar{u} + d\bar{d} - 2s\bar{s})$, $C = \sqrt{\frac{1}{3}}(u\bar{u} + d\bar{d} + s\bar{s})$.

[1]Now we know that the masses of the u, d and s quarks are not exactly the same. Therefore the flavor $SU(3)$ symmetry is approximate

Looking at the light meson spectra, this is indeed the case. Table 1.3 lists the first family of the pseudoscalar mesons and their quark content according to the constituent quark model. Clearly, members of the octet all have mass below 500 MeV/c^2 and the singlet has a mass on the order of 1 GeV/c^2. The mass differences between the octet members indicate that flavor $SU(3)$ is not an exact symmetry. A similar regularity is also observed in the vector meson nonet.

Meson	Quark combination	Mass(MeV/c^2)
π^+	$u\bar{d}$	140
π^-	$d\bar{u}$	140
π^0	$\frac{1}{\sqrt{2}}(d\bar{d} - u\bar{u})$	135
K^+	$u\bar{s}$	494
K^0	$d\bar{s}$	498
K^-	$\bar{u}s$	494
$\bar{K}^0$	$\bar{d}s$	498
η	$\frac{1}{\sqrt{6}}(u\bar{u} + d\bar{d} - 2s\bar{s})$	549
η'	$\frac{1}{\sqrt{(3)}}(u\bar{u} + d\bar{d} + s\bar{s})$	958

Table 1.3: Pseudoscalar mesons and their quark contents.

The constituent quark model has shown great success in correlating a large amount of data. Figure 1.3 shows the current constituent quark model assignment of the light mesons [39]. There are a number of detailed reviews of the light mesons [59].

1.6 Characteristic Quantum Numbers

In this section, we summarize various quantum numbers which will be used extensively in the following discussions[36]. Conventionally, a meson(a quark-antiquark bound state) is labeled by $I^G J^{PC}$, where I is the isospin, and J is the total angular momentum of that state [2]. The relations between these quantum numbers are the following.

The parity of the meson is given by

$$P = (-)^{L+1} \tag{1.10}$$

[2]Sometimes the spectroscopic notation $n\,^{2s+1}L_J$ is also used.

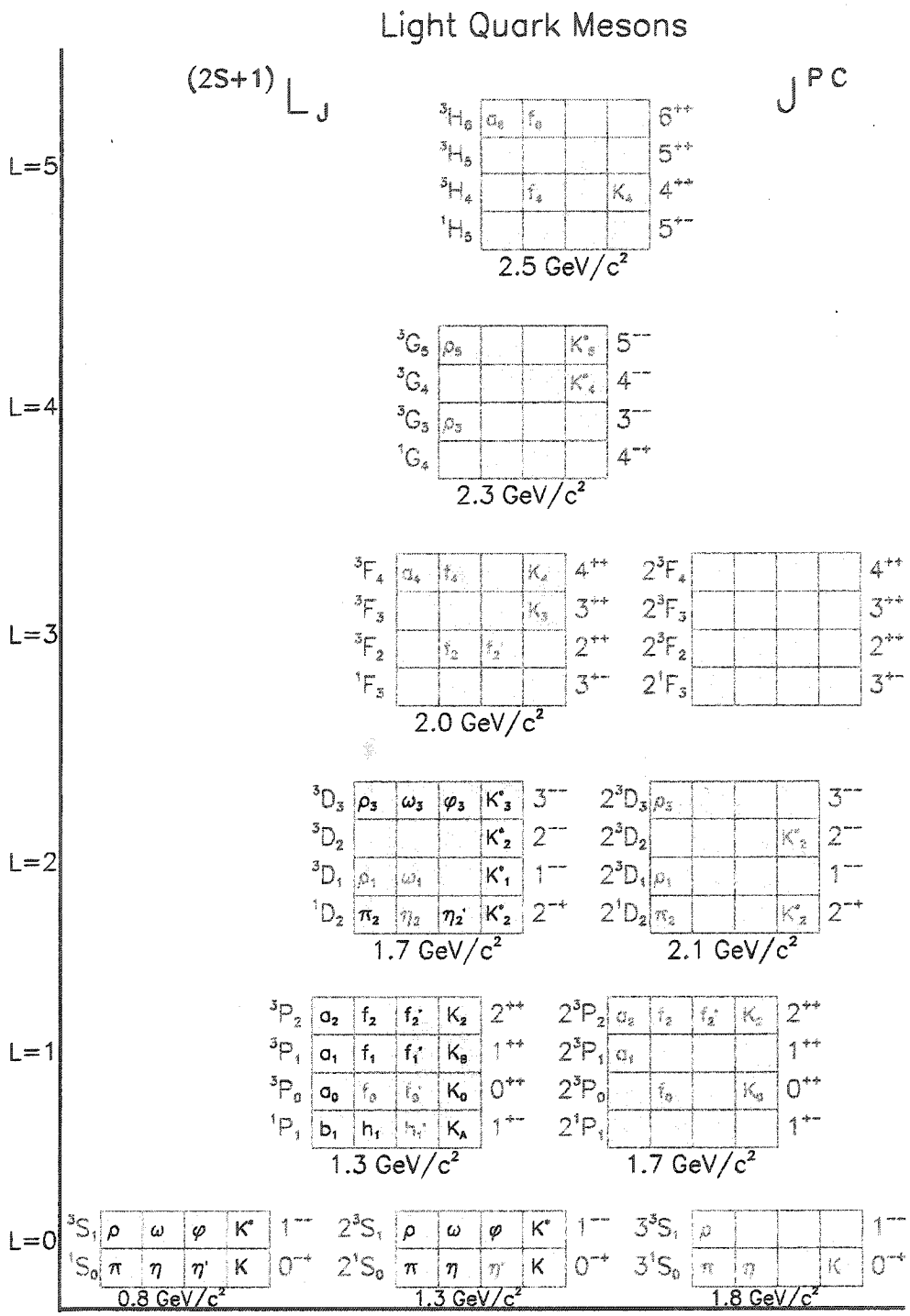

Figure 1.3: The $q\bar{q}$ spectrum of states. The orbital angular momentum of the nonet is plotted on the vertical axis, while the towers of radial excitations are shown on the horizontal axis. This figure is taken from reference[39].

where L is the orbital angular momentum between the $q\bar{q}$ pair. The factor $(-)^L$ comes from the space inversion in the angular part of the $q\bar{q}$ wavefunction $Y_{LM}(\theta, \phi)$. The minus sign arises because the quark and the antiquark have opposite intrinsic parity.

A neutral meson is a C-parity eigenstate. The eigenvalue of the C operator can be deduced by first replacing $q \leftrightarrow \bar{q}$ then interchanging their positions and spins [61],

$$C = -(-)^{S+1}(-)^L = (-)^{L+S} \tag{1.11}$$

the minus sign comes from interchanging two fermions. The factor $(-)^{S+1}$ comes from the symmetry of the $q\bar{q}$ composite spin states. And the $(-)^L$ is as before. S is the total spin of the $q\bar{q}$ pair.

The eigenvalues of G-parity are readily obtained from its definition(cf section 1.3.2),

$$G = (-)^{L+S}(-)^I = (-)^{L+S+I} = C(-)^I \tag{1.12}$$

here $(-)^{L+S}$ comes from the C-parity and $(-)^I$ comes from the rotation in isospin space.

Simple arithmetic shows that certain J^{PC} combinations are forbidden by the constituent quark model. For instance,

$$J^{PC} = 0^{+-}, 0^{--}, 1^{-+}, 2^{+-}, \ldots \tag{1.13}$$

These J^{PC} combinations are called unusual quantum numbers, or *exotic* quantum numbers.

1.7 Exotic Mesons and the Flux-Tube Model

The quark model has yielded great success. However QCD demands a much richer spectrum of the mesons. These extra mesonic states, known as the *hybrids*($q\bar{q}g$, where g denotes a gluon) and the *glueballs*(ggg), are attributed to the additional degree of freedom carried by the dynamic gluons inside the mesons. Multiquark states such as $qq\bar{q}\bar{q}$ are also allowed by QCD. Hybrids and glueballs, as well

as multi-quark states are collectively called *exotic mesons.*

The search for mesons beyond the constituent quark model has drawn a great deal of interests from both the theoretical and the experimental side. Several QCD-motivated phenomenological models have been proposed [26, 92, 93, 94, 32, 23, 31, 28]. All these models try to incorporate explicitly the gluonic degree of freedom into the quark-antiquark interaction picture.

The most commonly adopted model in this field so far is the *flux-tube model* of Isgur and Paton [64]. In the flux-tube model, the strong self-interactions between gluons are represented by $q\bar{q}$ pairs held together by a cylindrical tube of color flux, hence the name *flux tube.* The cylindrical configuration was based on the idea of Kogut and Susskind [69]. In their study, they showed that in describing the gluonic degree of freedom, the cylindrical assumption over a spherical one is more desirable because the energy is proportional to the length instead of the volume of the color field, which leads to a linear confining potential as required by QCD. Lattice QCD calculation, figure 1.4, also showed the formation of flux tubes between quark-antiquark pairs [20].

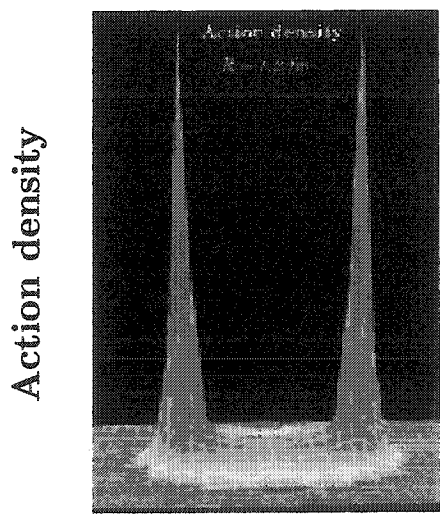

Figure 1.4: Lattice QCD simulation showing condensation of color field lines between the quark and the anti-quark [20]. The energy density is plotted on a two-dimensional grid.

In the flux tube picture, the conventional mesons are produced by excitations of a $q\bar{q}$ pair with the flux tube in its ground state. Being a physical object, the flux

tube itself can also be excited which brings in another degree of freedom. Pictorially, one may think of the excitation of the flux tube as rotation of a string around the $q\bar{q}$ axis. This additional degree of freedom lifts the limitation on the J^{PC} quantum numbers imposed by the constituent quark model as described in the last section. Thus mesons with exotic quantum numbers are allowed in the flux tube model.

The decay of a mesonic state occurs in the flux-tube model when the flux tube breaks [70]. It is usually assumed that the resulting $q\bar{q}$ pair is created in a relative $J^{PC} = 0^{++}$ configuration. To calculate the decay amplitude of a meson state, harmonic-oscillator wave functions are used. For the decay of a hybrid meson, certain selection rules therefore arise.

For a hybrid meson A decaying to two S-wave mesons B and C, the decay amplitude is proportional to a parameter $\Delta = \beta_B - \beta_C$[40]. The parameter β is defined in the harmonic-oscillator assumption to be the same as the rms relative momenta of the quarks [70]. If $\beta_B = \beta_C$ then the decay amplitude is zero. This was the original approximation made in the flux-tube model [64] which led to the selection rule that hybrid mesons do not decay to two S-wave mesons such as $\rho\pi$, but rather decay to P-wave/S-wave states such as $b_1(1235)\pi$ and $f_1(1285)\pi$.

A more sophisticated approach which allows the βs to differ for different mesons was carried out by Close and Page in their extended calculation [40]. In this extended flux-tube model, hybrid mesons can decay into two S-wave mesons such as $\rho\pi$ but not two identical mesons such as $\pi\pi$, $\rho\rho$, or $K\bar{K}$.

The flux-tube model has also been used to examine the conventional mesons. The amplitudes of all known $q\bar{q}$ meson decays are compared, and the flux tube model predictions are in excellent agreement with the data [70].

For the $J^{PC} = 1^{-+}$ isovector($I = 1$) hybrid, the mass is predicted by the flux tube model to be in the 1.8 to 2.0 GeV/c^2 range [24]. The decay ratios for a state with mass 1.6 GeV/c^2 are predicted to be [81],

$$b_1(1235)\pi : f_1(1285)\pi : \rho(770)\pi : \eta(1295)\pi : K^*K = 24 : 5 : 9 : 2 : 0.8 \qquad (1.14)$$

while at $2.0\,GeV/c^2$,

$$b_1(1235)\pi : f_1(1285)\pi : \rho(770)\pi : \eta(1295)\pi : \rho(1450)\pi = 43 : 10 : 16 : 27 : 12 \tag{1.15}$$

It is clear that even though $b_1(1235)\pi$ is predicted to be the dominant decay mode, the $\rho\pi$ channel has the second largest branching ratio and it may become important if phase space or experimental acceptance limits the decay of the 1^{-+} hybrid to the $b_1(1235)\pi$ channel. Considerable variation exists in the predicted decay widths of the hybrid mesons.

Different approaches can be used to search for these exotic meson states. In general, one could either look for an over-population of states in the constituent quark model assignment or look for mesonic resonances carrying exotic quantum numbers as shown in the previous section. The first approach is more difficult because the hybrid states can mix with the conventional $q\bar{q}$ states, and also the hybrid states can simply be indistinguishable from the $q\bar{q}$ states. The latter approach is more promising. In this approach, $J^{PC} = 1^{-+}$ is of special interest. It is expected to be one of the lowest lying exotic meson states, and its width is predicted to be much narrower than that of the 0^{+-} which makes it easier to identify in a spectroscopic study.

1.8 Previous Observation of the Exotic Mesons

Recent experiments at BNL, CERN and IHEP have accumulated compelling evidence for isovector 1^{-+} exotic meson states. A state was identifed as 1^{-+} in the E852 experiment at BNL in the $\eta\pi$ channel [37] with a mass of $1370 \pm 16^{+50}_{-30}\,MeV/c^2$ and a width of $385 \pm 40^{+65}_{-105}\,MeV/c^2$. The Crystal Barrel collaboration at CERN reported a similar state in $\eta\pi$ channel from two different experiments [3, 4]. This state was also observed by VES at IHEP in the $\eta\pi$ channel [51] with a mass of $1316 \pm 12\,MeV/c^2$ and a width of $287 \pm 25\,MeV/c^2$.

Another higher lying 1^{-+} state was first reported by BNL in the $\rho\pi$ channel [5, 38] with a mass of $1593 \pm 8^{+29}_{-47}\,MeV/c^2$ and a width of $168 \pm 20^{+150}_{-12}$. Also at BNL, a 1^{-+} state was observed in the $\eta'\pi$ channel [65] with a mass of $1597 \pm 10^{+45}_{-10}\,MeV/c^2$

and a width of $340 \pm 40 \pm 50\, MeV/c^2$. At VES, a combined fit to intensities in the $\rho\pi$, $\eta'\pi$ and $\omega\pi\pi$ systems [68] resulted in a Breit-Wigner shape with mass $1600\, MeV/c^2$ and width $300\, MeV/c^2$. Table 1.4 lists previous experimental results on the 1^{-+} exotic meson states.

Exp.	Beam/Target	Channel	Mass(MeV/c^2)	Width(MeV/c^2)
VES	π^-/Be	$\eta\pi$	1316 ± 12	287 ± 25
		$\eta'\pi$	N/A	N/A
		$\rho\pi$, $\eta'\pi$, $\omega\pi^-\pi^0$	1600	300
E852	π^-/p	$\eta\pi$	$1370 \pm 16^{+50}_{-30}$	$385 \pm 40^{+65}_{-105}$
		$\rho\pi$	$1593 \pm 8^{+29}_{-47}$	$168 \pm 20^{+150}_{-10}$
		$\eta'\pi$	$1597 \pm 10^{+45}_{-10}$	$340 \pm 40 \pm 50$
		$f_1\pi^\dagger$	$1709 \pm 24 \pm 41$	$403 \pm 80 \pm 115$
		$b_1\pi^\dagger$	1664 ± 8	185 ± 25
CBAR	$\bar{p}d$	$\eta\pi$	$1400 \pm 20 \pm 20$	$310 \pm 50^{+50}_{-30}$
	$\bar{p}p$	$\eta\pi$	1360 ± 25	220 ± 90

Table 1.4: Experimental results on the 1^{-+} exotic meson states. † to be published.

In an earlier photon beam experiment conducted at SLAC [42], a narrow peak in $\pi^-\pi^+\pi^+$ mass at $1775\, MeV/c^2$ was observed. It was speculated to be an 1^{-+} candidate. However, due to low statistics a partial wave analysis could not be performed on those data.

1.9 Photoproduction of Exotic Mesons

There is a wealth of data on light meson production taken from fixed target experiments using hadron beams(primarily π and K). However, little is known about the photoproduction of light-quark mesons. Table 1.5 is a partial summary of existing photoproduction data [39]. Experience has shown that new probes often lead to new discoveries and this is also expected to be true for the photon.

Model dependent calculations indicate that the J^{PC} exotic mesons should be produced copiously in photoproduction [7, 8]. Compared to the pseudoscalar beams such as π and K, the photon as a probe is very different. In the pseudoscalar meson beams the valence quarks q and $\bar{q}$ have their spins anti-aligned($S = 0$) whereas in

Reaction	$E_\gamma\,(GeV)$	Events	Ref.
$\gamma p \to p\pi^+\pi^-$	9.3	3500	[21]
$\gamma p \to p\pi^+\pi^-$	19.3	20908	[1]
$\gamma p \to p\pi^+\pi^-\pi^0$	2.8	2159	[21]
$\gamma p \to p\pi^+\pi^-\pi^0$	4.7	1606	[21]
$\gamma p \to p\pi^+\pi^-\pi^0$	9.3	1195	[21]
$\gamma p \to p\pi^+\pi^-\pi^0$	$4.7 - 5.8$	3001	[54]
$\gamma p \to p\pi^+\pi^-\pi^0$	$6.8 - 8.2$	7297	[54]
$\gamma p \to n\pi^+\pi^+\pi^-$	$4.7 - 5.8$	1723	[54]
$\gamma p \to n\pi^+\pi^+\pi^-$	$6.8 - 8.2$	4401	[54]
$\gamma p \to n\pi^+\pi^+\pi^-$	$16.5 - 20$	3781	[43]
$\gamma p \to p\pi^+\pi^-\pi^0$	$20 - 70$	14236	[15]
$\gamma p \to p\pi^+\pi^-\pi^+\pi^-$	$4 - 6$	~ 330	[48]
$\gamma p \to p\pi^+\pi^-\pi^+\pi^-$	$6 - 8$	~ 470	[48]
$\gamma p \to p\pi^+\pi^-\pi^+\pi^-$	$8 - 12$	~ 470	[48]
$\gamma p \to p\pi^+\pi^-\pi^+\pi^-$	$12 - 18$	~ 380	[48]
$\gamma p \to p\pi^+\pi^-\pi^+\pi^-$	$15 - 20$	6468	[2]
$\gamma p \to p\pi^+\pi^-\pi^0\pi^0$	$20 - 70$	8100	[16]
$\gamma p \to p\pi^+\pi^+\pi^-\pi^-\pi^0$	19.5	2553	[29]
$\gamma p \to \Delta^{++}\pi^-\pi^+\pi^-$	$4 - 6$	~ 200	[48]
$\gamma p \to \Delta^{++}\pi^-\pi^+\pi^-$	$6 - 8$	~ 200	[48]
$\gamma p \to \Delta^{++}\pi^-\pi^+\pi^-$	$8 - 12$	~ 200	[48]
$\gamma p \to \Delta^{++}\pi^-\pi^+\pi^-$	$12 - 18$	~ 200	[48]
$\gamma p \to p\omega$	$4.7 - 5.8$	< 1600	[54]
$\gamma p \to p\omega$	$6.8 - 8.2$	< 1200	[54]
$\gamma p \to p\omega$	4.7	1354	[21]
$\gamma p \to p\omega$	9.3	1377	[21]
$\gamma p \to p\phi$	4.7	136	[21]
$\gamma p \to p\phi$	9.3	224	[21]
$\gamma p \to na_2^+$	$4.7 - 5.8$		[54]
$\gamma p \to na_2^+$	$6.8 - 8.2$		[54]
$\gamma p \to na_2^+$	19.5	~ 100	[43]

Table 1.5: A partial compilation of existing photoproduction data. Notice the small event numbers.

the photon, via the *vector dominance model*(VDM) [3], their spins are aligned($S = 1$). According to the flux tube model, the incident photon can be viewed as a vector meson with its flux tube in the ground state. After scattering, if its flux tube is excited to the first excited state and the quark spins remain aligned, the resulting system can have J^{PC} combinations of 0^{+-}, 0^{-+}, 1^{+-}, 1^{-+}, 2^{+-} and 2^{-+}. The combinations 0^{+-}, 1^{-+} and 2^{+-} are exotic quantum numbers. It is also worth mentioning that the photon beam is the only one that can be easily prepared in the laboratory that is of vector nature.

1.10 This Experiment

Almost all of the earlier light meson photoproduction experiments suffer from low statistics. G6C at Jefferson Lab was specifically designed to produce a large amount of data so that a partial wave analysis(PWA) can be performed. The focus of the G6C experiment is to study the light meson systems in the $1-2\,GeV/c^2$ mass region from γp interactions at $5.5\,GeV/c$.

In this dissertation, I will present the partial wave analysis result for the final state $\pi^+\pi^-\pi^0$. This is an interesting channel because it can couple to the exotic quantum numbers, and no confirmed experimental evidence has been reported for the exotic mesons in photoproduction. Also it is a neutral channel so that both isovector and isoscalar mesons can be studied.

[3]The vector dominance model [57, 82] states that in photon induced hadronic interactions, the photon couples electromagnetically to a vector meson, ρ, ϕ or ω. The coupling ratio is determined by the quark contents of these vector mesons. Specifically,

$$\rho = \frac{1}{\sqrt{2}}(u\bar{u} - d\bar{d}) \rightarrow \frac{1}{\sqrt{2}}(\frac{2}{3} + \frac{1}{3}) = \frac{1}{\sqrt{2}}$$

$$\omega = \frac{1}{\sqrt{2}}(u\bar{u} + d\bar{d}) \rightarrow \frac{1}{\sqrt{2}}(\frac{2}{3} - \frac{1}{3}) = \frac{1}{3\sqrt{2}}$$

$$\phi = s\bar{s} \rightarrow -\frac{1}{3} = -\frac{1}{3}$$

note that the coupling constants are the reciprocal, therefore we have

$$\rho : \omega : \phi = 9 : 1 : 2$$

1.11 Organization

In Chapter 2, I will provide a description of the experimental apparatus. Chapter 3 describes data processing and event selection as well as the general feature of the data. The partial wave analysis formalism and result are discussed in Chapter 4. In Chapter 5, results from the mass dependent analysis are presented. Final discussion and conclusions are given in Chapter 6.

CHAPTER 2
EXPERIMENTAL APPARATUS

This chapter describes the functionality of individual detector element used in this experiment as well as the basic characteristics of the accelerator. The trigger setup for experiment G6C will also be discussed. The running condition for this experiment is summarized in table 2.2 at the end of this chapter.

2.1 CEBAF

The *Continuous Electron Beam Accelerator Facility*(CEBAF), located in the *Thomas Jefferson National Accelerator Facility*(TJNAF), is a recirculating linear electron accelerator using super-conducting radio-frequency(RF) cavities, as sketched in figure 2.1. A beam of $67\,MeV$ pre-accelerated electrons are injected into one of the parallel linear accelerators(linacs) connected by five recirculation arcs on both ends. Each time the electrons passing through the linacs their energies are increased by ΔE, where ΔE is close to $600\,MeV$ depending on the linac settings. At the end of the linacs, the electrons can be extracted from any of the five passes. With typical linac settings, the electron beam energies available to the end stations range from $1.2\,GeV/c$ to $6.0\,GeV/c$ in multiples of $1.2\,GeV/c$.

The electrons circulate in bunches with a pulse separation of $0.67\,ns$. Upon exiting the linacs, they are separated into three beams each with $499\,MHz$ frequency. Therefore the three experimental halls are seeing electrons in bunches that are separated by $2.004\,ns$. This is the so-called RF time-bucket, which plays very important role in particle identification and event reconstruction.

2.2 Hall B

Experimental Hall B is one of the three end stations dedicated to physics research. It houses two major detector systems, the *CEBAF Large Acceptance Spectrometer*(CLAS) and the *Hall-B Bremsstrahlung tagging system*(Tagger), as shown

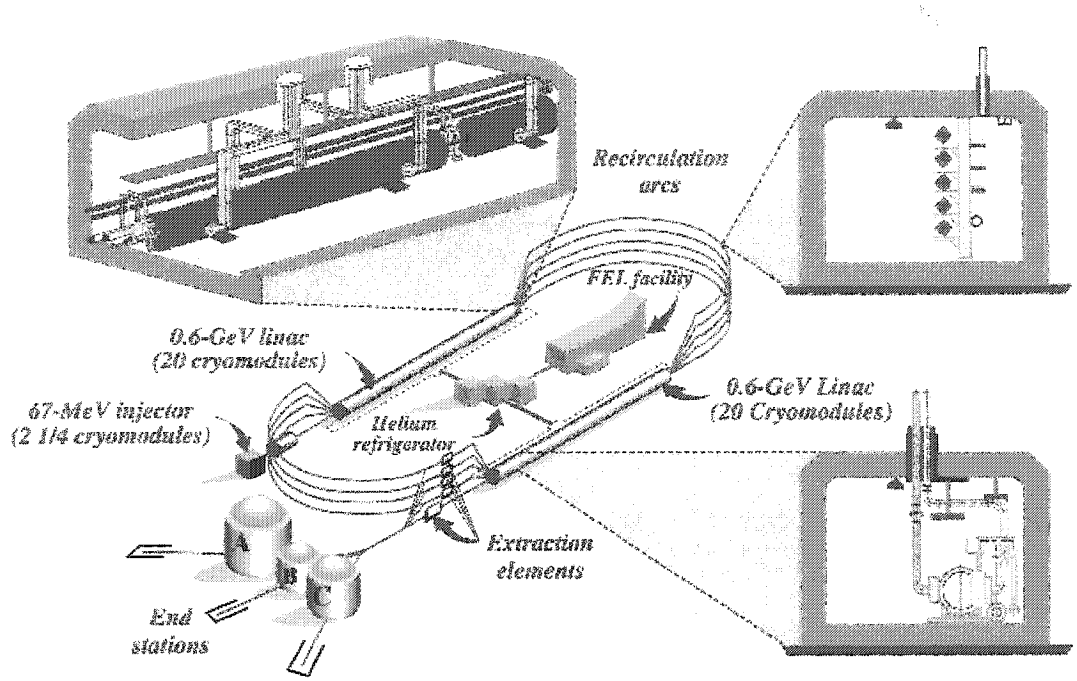

Figure 2.1: Accelerator configuration.

in figure 2.2. Both electron-beam and photon-beam experiments are conducted in Hall B.

2.2.1 CLAS

CLAS is one of the major detector systems in Hall B used by both electron-beam and photon-beam experiments. It has six instrumented sectors that are symmetric in azimuthal angle about the beam line. Figure 2.3 shows the mid-plane view of CLAS. To achieve the scientific goals of Hall B, CLAS was designed with the following considerations [96].

- Large angular and momentum detection range
  - for charged particles, $8^\circ \leq \theta \leq 142^\circ$, $0^\circ \leq \phi \leq 360^\circ$
  - for neutral particles, $8^\circ \leq \theta \leq 45^\circ$, $0^\circ \leq \phi \leq 360^\circ$
  - momentum detection range for charged particles $0.1 \leq p \leq 4.0\, GeV/c$
  - energy detection range for photons $E \geq 50\, MeV$

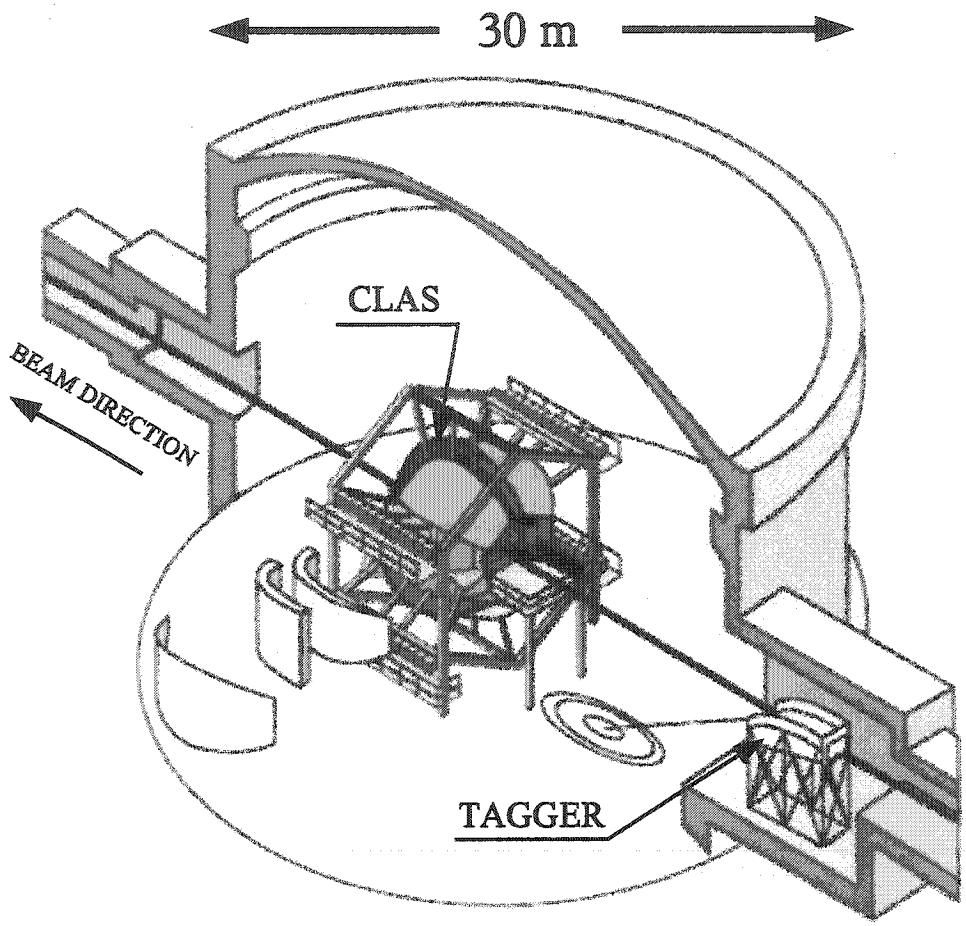

Figure 2.2: Picture of the experimental Hall B. The electron beam from the accelerator enters the hall from the right-hand side of the picture.

- Good angular and momentum resolution
  - momentum resolution $\delta p/p \approx 0.5\%$ at small θ
  - momentum resolution $\delta p/p \approx 1.0\%$ at large θ
  - angular resolution $\delta\theta \approx 1.0\, mrad$
- High luminosity
  - electron beam luminosity $L \approx 10^{34} cm^{-2} s^{-1}$
  - photon beam intensity $I \approx 10^{7} s^{-1}$

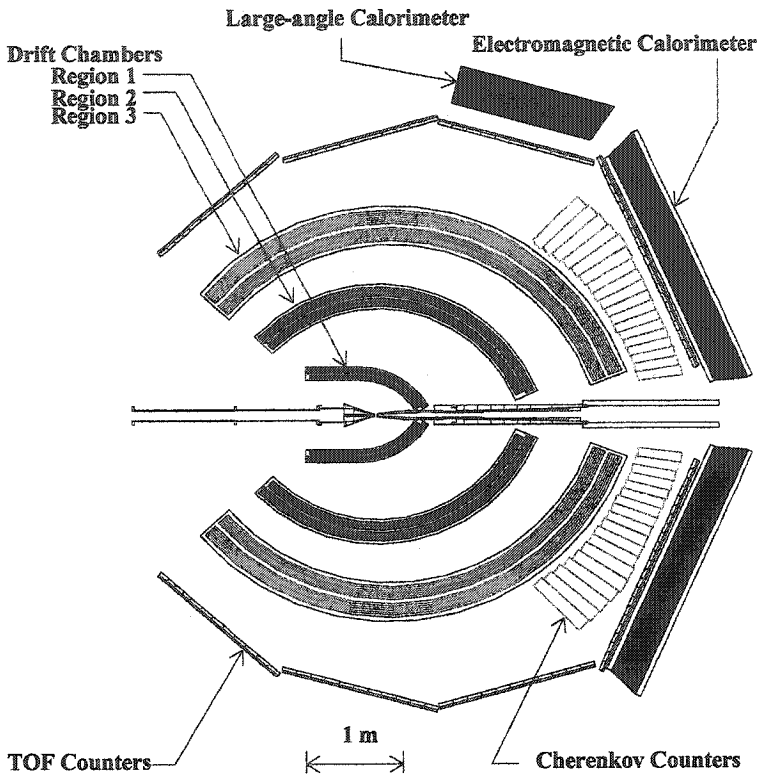

Figure 2.3: The mid-plane view of CLAS.

2.2.1.1 Target

The target used in this experiment is a cylindrical liquid hydrogen(LH_2) cell. It is about $3\,cm$ in diameter and $18\,cm$ in length. The specification of the target is listed in figure 2.7. During most CLAS experiments, the target is placed in the center of the CLAS detector. In our experiment, since we are interested in t-channel meson production at low momentum transfer, the target was displaced by one meter upstream relative to its normal position [4]. This displacement increases the negative particle(π^- and K^-) acceptance significantly.

2.2.1.2 Start Counter

The start counter(ST) [91] is a set of three independent thin scintillators surrounding the target cell. Each set is arranged to cover two adjacent CLAS sectors.

[4]This target position was optimized for the reaction channel $\gamma p \to \pi^+\pi^+\pi^- n$ in which all three charged pions are going forward in the laboratory reference frame.

The scintillators are bent to form a hexagonal cone(the *nose* region) and a hexagonal tube(the *leg* region). A photomultiplier tube is attached to the end of each leg. Figure 2.4 sketches one of the completed segments. The start counter produces a fast timing signal as an input to the level–1 CLAS trigger. This signal, when used in coincidence with the signal from the tagger, reduces the accidental trigger rate significantly. Working in conjunction with the time-of-flight counter and the tagger in particle identification, the start counter pinpoints the RF time bucket(2.004 ns interval) that gives rise to the hadronic event.

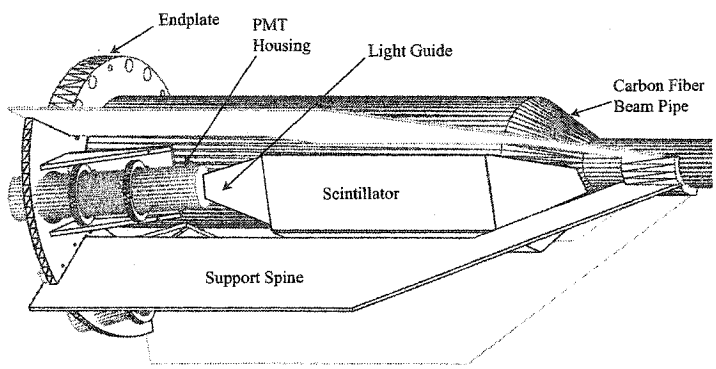

Figure 2.4: Sketch of the Start Counter.

2.2.1.3 Main Torus Magnet

The magnetic field for CLAS is generated by six superconducting toroidal coils. The magnets are placed in 60° intervals in azimuthal angle about the beam line. The maximum field is about 2.0 Tesla(peak field 3.5 Tesla at conductors). The polarity is such that positive particles bend away from the beam line and negative particles bend toward the beam line.[5] The magnetic field essentially leaves the azimuthal angle of the charged particles unaltered [79]. During the G6C run, the torus magnet current was set at 1938 Amp, which is $\sim$ 50% of the maximum value. This is the so-called *half field* setting. Lowering the magnetic field makes charged particles bend less, and thus increases the small-angle acceptance of the negative particles.

[5]The polarity of the magnetic field can be reversed if desired by the experimental setup.

2.2.1.4 Drift Chambers

The tracking system consists of three regions, labeled R1, R2 and R3. Each region is equipped with six drift chambers(DC) corresponding to the six CLAS sectors [79, 22, 30, 85]. Figure 2.5 shows the cross section of the drift chambers. Each chamber covers a polar angular range of 134° and an azimuthal angular range of 50°. The R1 and R3 chambers are placed outside of the magnetic field.

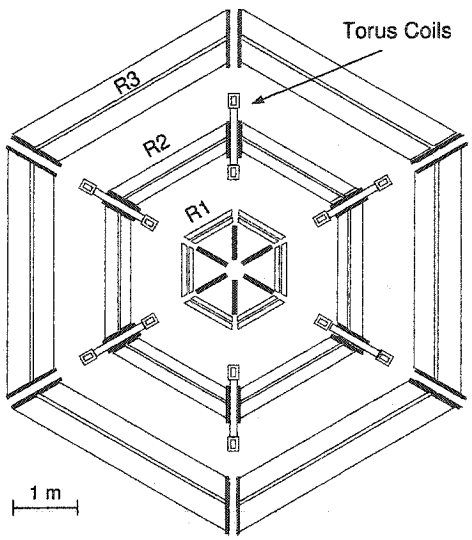

Figure 2.5: The cross section of the Drift Chambers. The laboratory reference frame is so defined that the Z-axis is along the beam line pointing into the paper, and the X-axis points to the left.

The wires in each chamber are divided into two super-layers. Each super-layer consists of six layers of drift cells each formed with one sense wire surrounded by six field wires in a hexagonal arrangement. There are a total 35, 148 drift cells. The wires in the first super-layer of each region are arranged axially with respect to the magnetic field, and the wires in the other super-layer of each region are oriented at a 6° stereo angle with respect to the axial wires to provide the azimuthal information. The sense wires are 20 μm diameter gold-plated tungsten, and the field wires are 140 μm diameter gold-plated aluminum. The field wires are held at high voltage in the experiment.

The drift chambers are filled with a gas mixture of 90% Ar and 10% CO_2. The drift velocity of the avalanche electrons is approximately 4 $cm/\mu s$.

2.2.1.5 Time-of-Flight Counter

The Time-of-Flight(TOF) system [88] is used for triggering and for particle identification. It comprises a total of 342 plastic scintillators, 57 per sector, with one photomultiplier attached to each end of every scintillator. The scintillators are placed outside of the drift chambers and the Cerenkov counters, as shown in figure 2.3. The scintillators are $5.08\,cm$ thick and their lengthes vary from $32\,cm$ in the downstream direction to $450\,cm$ at very large angles. The width of the scintillators is $15\,cm$ in the very forward and very backward directions and it is $22\,cm$ in the middle. The scintillators are arranged into four planes and are parallel to the axial wires of the drift chambers. The last eighteen strips are joined into nine pairs which leaves 48 electronic channels per sector. The Time-of-Flight system covers an angular range in θ_{LAB} between $8\,^\circ$ and $142\,^\circ$. The average timing resolution for pions ranges from $150\,ps$ in the forward direction to about $300\,ps$ at the backward angles.

2.2.1.6 Forward Electromagnetic Calorimeter

The *Forward Electromagnetic Calorimeter*(EC) [10] was used to measure the energy deposition and the positions of neutral particles(neutrons and photons). There are six sectors in the calorimeter, corresponding to the six CLAS sectors. Each sector covers polar angles between 8° and 45°.

Each sector consists of 39 layers of lead-scintillators, a total of sixteen radiation lengths of material. The scintillators in each layer are $10\,cm$ thick and they are interleaved with $2.3\,mm$ thick lead sheats. Each scintillator layer is divided into thirty-six $10\,cm$ wide parallel strips. The scintillator strips in each layer are oriented at 120° with respect to the strips in the previous layer, thus forming one of three *views*(u, v and w views). The electromagnetic calorimeters are placed beyond the time-of-flight counters, as shown in figure 2.3.

2.2.1.7 Other CLAS Detectors

Other major CLAS detectors include the Cerenkov Counter(CC) [6] for electron-pion identification and the Large Angle Calorimeter(LAC) for neutral particle detection at large angles. These detectors are not used in this experiment.

2.2.2 Bremsstrahlung Tagging System

The photon beam in Hall B is prepared from the Bremsstrahlung radiation of energetic electrons traversing a thin radiator. The radiator is made of high atomic number material(usually gold) and has a width on the order of $\sim 10^{-4}$ radiation length. The tagging system [77, 90] is designed to tag photon energies over the range from 20% to 95% of the incident electron beam energy, and is able to operate with electron beam energy up to $6.1\,GeV/c$. Table 2.1 lists the running condition of the tagger for this experiment.

E_0	$5.744\,GeV$
Electron beam current	$40/50\,nA$
Radiator	$10^{-4}\,r.l.$
T-counter	$1-12$
Tagged photon energy	$4.83-5.5\,GeV$
Tagged photon flux	$10^7\,s^{-1}$

Table 2.1: The running condition of the tagger for the G6C experiment.

The geometry of the tagger is shown in figure 2.6. A single, uniform field dipole magnet is combined with a hodoscope containing two layers of plastic scintillators to detect both the energy and the arrival time of the scattered electrons. The first layer, called the E-plane, contains 384 narrow scintillators(E-counters). The E-plane is aligned along the focal plane of the dipole magnet. Each scintillator in the E-plane overlaps with its neighbors by one-third of their widths and provides an energy resolution of $0.1\%\,E_0$, where E_0 is the incident electron energy. Behind the E-plane is the second layer of scintillators called the T-plane. The T-plane contains 61 overlapping scintillators(T-counters). Each scintillator is $2\,cm$ thick with phototubes attached by solid light guides at both ends. The timing resolution for the T-counters is $300\,ps$(FWHM) or better.

The signal of an event is a set of times from both the E-counters and the T-counters measured with FASTBUS TDCs. The output signals from the T-counter constant-fraction discriminators are fed into the Master OR(MOR) logic after passing through the E-T coincident logic module. The MOR logic is a simple cascade of outputs of the AND gates into fast OR gates. The output of the MOR signals that

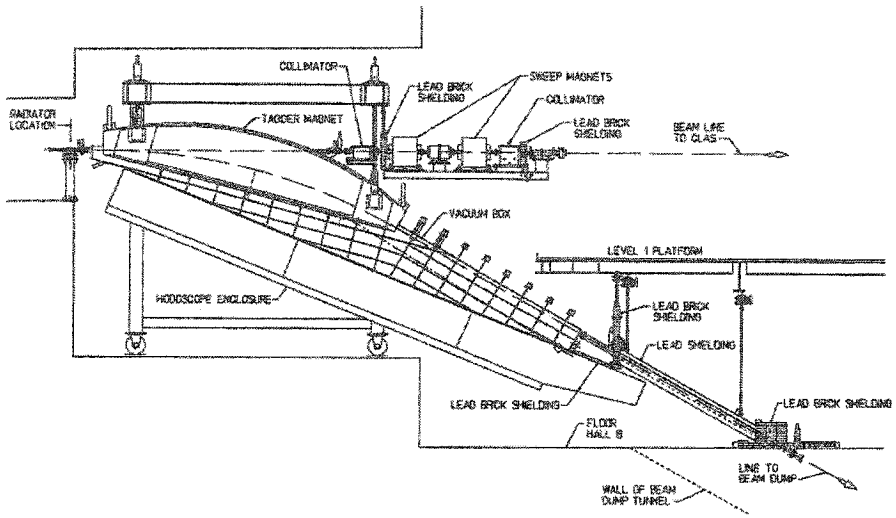

Figure 2.6: An elevation view of the Hall B bremsstrahlung tagging system. The over all length of the magnet is about 6 meters.

a photon has been registered for the CLAS level–1 trigger [90, 12].

2.3 Experimental Trigger Setup

In CLAS photon beam experiments, the level–1(L1) trigger is produced by a coincidence of the *photon trigger* [87] from the tagger spectrometer and the *CLAS trigger* [27, 47] which registers a hadronic event. These two sets of signals are combined in the *trigger supervisor*(TS). The CLAS trigger is a logic combination of CLAS detector signals including signals from the time-of-flight(TOF) counters and the electromagnetic calorimeter(EC). The photon trigger contains signals from the Master OR(MOR) as described in the last section and signals from the start counter(ST).

In this experiment we required charged tracks in two different CLAS sectors in the CLAS trigger. Since all the channels being studied in this experiment are multi-particle channels, requiring two charged tracks in CLAS does not bias the trigger. On the photon trigger side, we triggered on the first twelve T-counters in the Master OR(MOR) and required two-out-of-three start counter sectors.

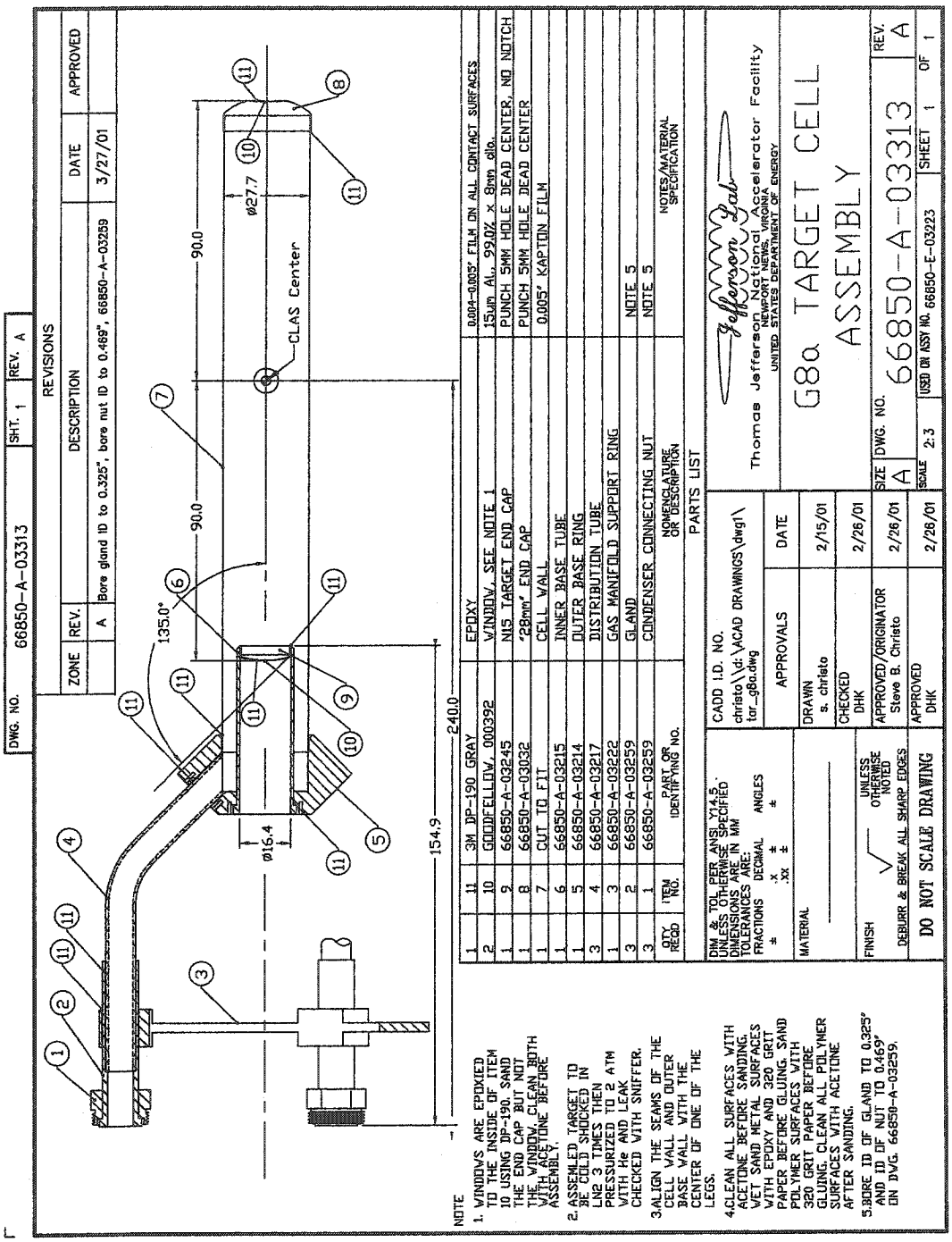

Figure 2.7: Specification of the g8a/g6c target.

2.4 Detector Calibration

The major detectors(DC, TOF, Tagger) were calibrated by the G6C group members right after the data were taken, following the standard CLAS calibration procedures. The time-of-flight system and the electromagnetic calorimeters were calibrated by Mr. Lei Guo [89] and the drift chambers were calibrated by Dr. Mina Nozar [72]. The tagger was calibrated by me using my newly developed tagger calibration software package [12, 74]. The quality of the calibrations meets the standard CLAS requirement as specified in reference [12, 74, 89, 72].

2.5 Summary of Running Conditions

E_0	$5.744\,GeV$
Electron beam current	$40/50\,nA$
Radiator	$10^{-4}\,r.l.$
T-counter used	$1-12$
Taggeed photon energy	$4.83-5.5\,GeV$
Tagged photon flux	$\sim 10^7\,s^{-1}$
Number of tagged photon	3.59×10^{12}
Sensitivity‡	2.743 events per pb
Tagger magnet current	$2097\,A$
Collimator	$2\,mm$ diameter passive
Target position	$-100.0\,cm$
Torus magnet current	$1938\,A$
Trigger	MOR(1-12) & ST(2/3) & Two-charged-particle
Event rate	$\sim 1.5\,k\,s^{-1}$
DAQ live time	$\sim 85\%$

Table 2.2: Summary of running conditions for CLAS experiment E01-017(G6C). ‡ The sensitivity is calculated as $\mathcal{S}=\frac{1.27\times18\,cm}{10^{12}\,pb\times30\,cm}\times N_\gamma$, where N_γ is the total number of beam photons and $18\,cm$ is the length of the target.

CHAPTER 3
DATA REDUCTION

3.1 Overview

The event information, for instance the raw TDC and ADC readings, from the CLAS detector and the tagger is converted by the data acquisition system(DAQ) and stored in *raw banks* in *BOS* format. In the off-line analysis, the raw banks are fed into the event reconstruction program called *a1c* along with the detector geometry parameters and calibration constants which are stored in the calibration database. The beam reconstruction, charged particle tracking, momentum measurement of neutral and charged particles, event vertex fitting, event timing reconstruction and particle identification are performed by a1c. This process is referred to as *data cooking.* Upon exiting a1c, the reconstructed events are written into the *cooked banks*, which are then ready for topological selection and other data selection procedures.

3.2 Event Vertex and Beam Energy Cut

Events with reconstructed vertices outside of the target cell were removed at an early stage of the event filtering. Due to the narrow photon beam, the event vertex distribution in the x and y directions are narrower than the diameter of the target cell. The vertex cut is defined as,

$$x^2 + y^2 < 1.4^2, \ -109.0 < z < -92.0 \tag{3.1}$$

where (x, y, z) are the coordinates of the event vertex in centimeters. Figure 3.1 shows the event vertex distributions after this cut.

A cut on the beam photon energy was also applied prior to other kinematic cuts, to match the trigger conditions. Events associated with beam photon energy in the range

$$4.83 < E_\gamma < 5.5 \tag{3.2}$$

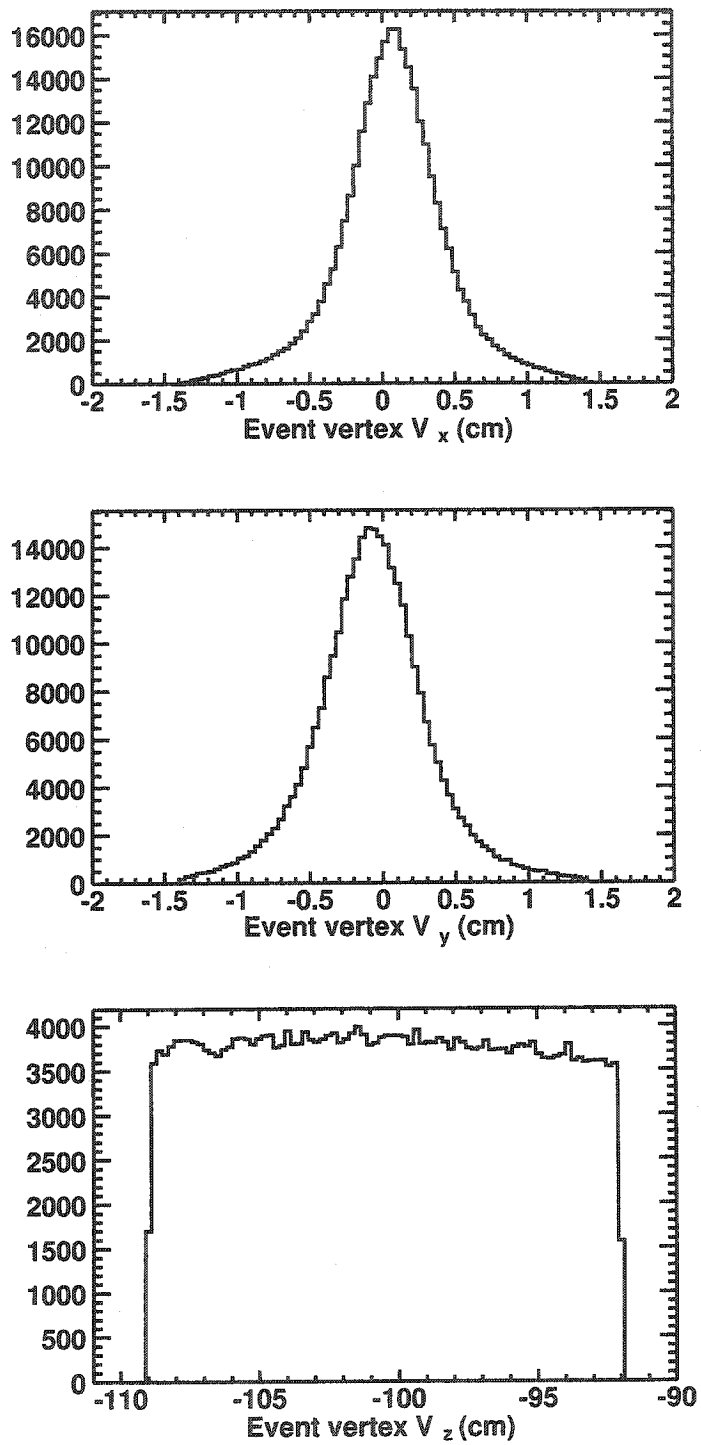

Figure 3.1: Event vertex distributions in the x, y and z directions. Due to collimation, the x and y distributions are narrower than the diameter of the target cell.

were kept, where E_γ represents the beam energy in GeV. Figure 3.2 shows the beam photon energy spectrum.

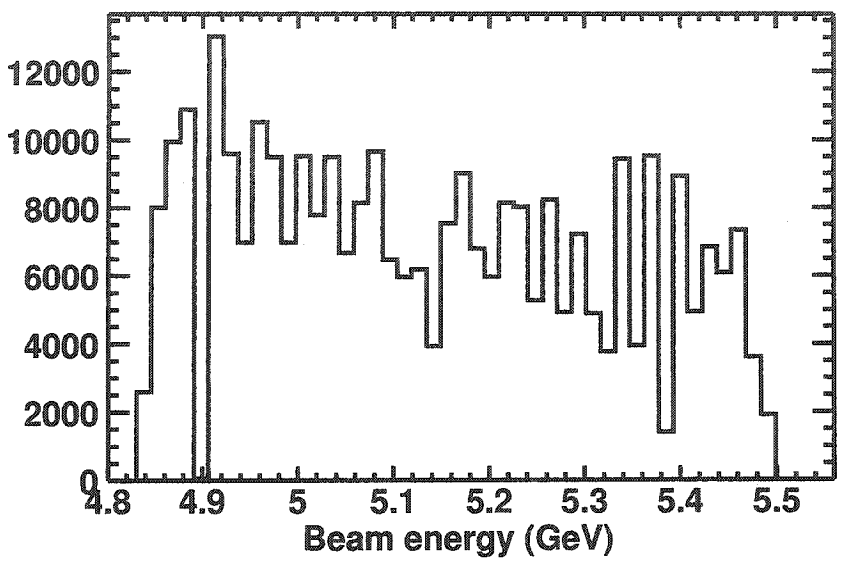

Figure 3.2: Beam photon energy spectrum. Notice the depleted regions corresponding to inefficient tagger T-counter paddles. The same distribution is mimicked in generating Monte Carlo events for the partial wave analysis.

3.3 Vertex Timing Cut

In CLAS photon-beam experiments, the start time of a hadronic event is determined by the tagger and the start counter(ST) while the flight time of charged particles is measured by the time-of-flight(TOF) counters. To ensure that the charged particles in an event were indeed produced by the tagged photon, it is necessary to compare the time of that event at the event vertex as measured by the tagger(v_time) and by the start counter(st_v_time). In obtaining these two times, the propagation time of the beam photon and the charged particles are taken into account. The difference of these two times for a given event should fall within the beam pulse separation time($2.004\,ns$), therefore the timing cut is defined as

$$|v\_time - st\_v\_time| \leq 1.002\,ns. \tag{3.3}$$

Figure 3.3 shows this time difference after the vertex timing cut.

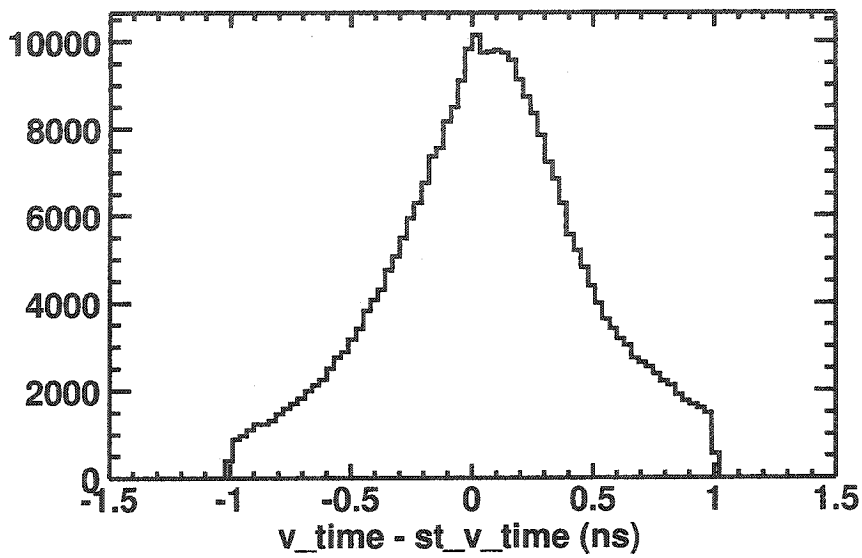

Figure 3.3: Difference between event vertex time as measured by the tagger and by the start counter. The propagation time of the beam photon and the charged particle in the target cell are taken into account in calculating these two times. The cut value is determined by the accelerator radio frequency(RF) time structure($2.004\,ns$).

3.4 Missing Momentum Cut

The reaction channel we are interested in is

$$\gamma p \rightarrow p\pi^+\pi^-(\pi^0) \tag{3.4}$$

where the π^0 in parenthesis denotes it is a missing particle and needs to be reconstructed with the missing momentum technique. The primary background in this case is two-pion production

$$\gamma p \rightarrow p\pi^+\pi^- \tag{3.5}$$

The measured total cross sections for these two reactions at photon energy $\sim 5\,GeV$ are of the same order of magnitude with reaction (3.5) about 40% lager

than reaction (3.4) [6] [19]. Since the π^0 mass is very small, with finite resolution it is hard to distinguish these two reaction channels by looking only at the missing mass off of the $p\pi^+\pi^-$ system. Figure 3.4 shows the missing mass squared distribution. The shaded region in this plot contains events from both reactions.

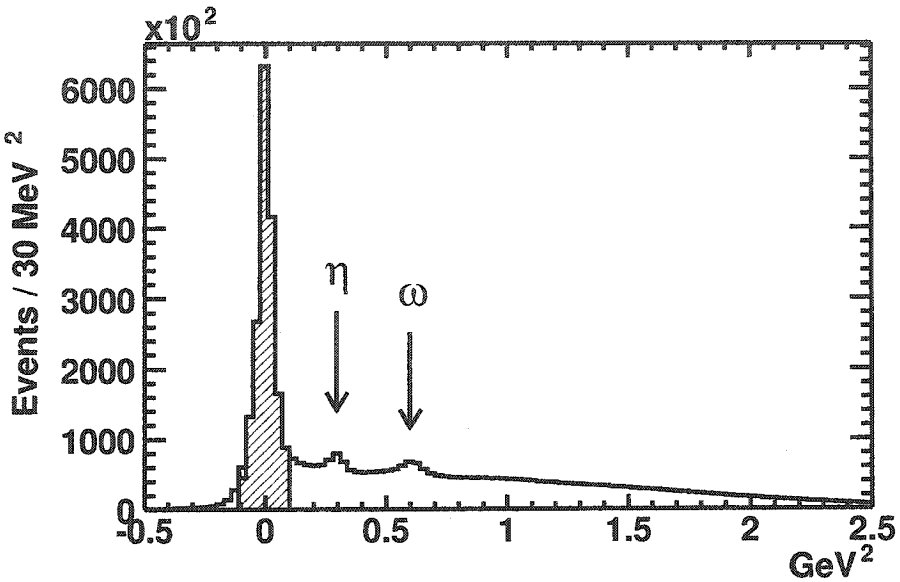

Figure 3.4: Missing mass squared(mm^2) off of the $p\pi^+\pi^-$ system. The two small peaks at $\sim 0.3\,GeV^2$ and $\sim 0.6\,GeV^2$ are identified as the η and the ω, respectively. The shaded region contains both events from the missing π^0 and events from the exclusive two-pion production.

To distinguish the events from these two reactions, one has to rely on the momentum carried by the missing particle(*missing momentum*). The missing momenta in the transverse and parallel directions relative to the z axis are defined as,

$$mmPz = \sum_i p_z^i \tag{3.6}$$

$$mmPt = \sqrt{(\sum_i p_x^i)^2 + (\sum_i p_y^i)^2} \tag{3.7}$$

[6] At $E_\gamma = 5.25\,GeV$, the cross section for reaction (3.5) is $0.019 \pm 0.001\,(10^{-27}\,cm^2)$, the cross section for reaction (3.4) is $0.0135 \pm 0.015\,(10^{-27}\,cm^2)$.

where the superscript i runs over all measured particles, including the beam photon and the target proton, in equation (3.4). The momenta of the particles on the right hand side of equation (3.4) bear a minus sign.

Figure 3.5 shows the missing momentum for events in the shaded region in figure 3.4. Two groups of events are clearly seen in this plot. The events that

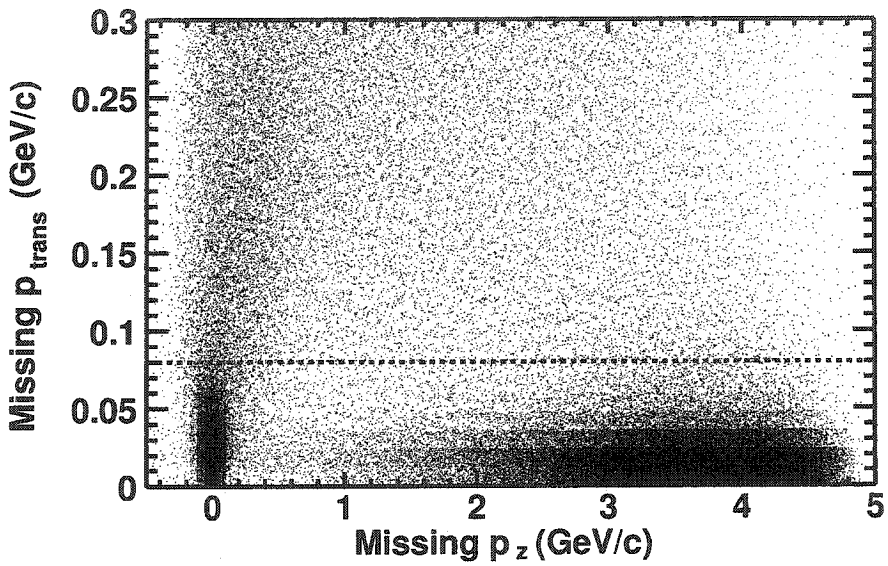

Figure 3.5: The momentum carried by the missing particle(*missing momentum*) for events in the shaded region in figure 3.4. On the vertical axis is the missing momentum in the transverse direction relative to the beam line. On the horizontal axis is the missing momentum in the z direction. The dashed line marks the missing momentum cut. Events below the dashed line are rejected.

accumulate at large missing P_z come from mis-identified beam photons [7]. The events in the condensed region around the origin come from the exclusive two-pion production reaction (3.5), in which case there is no particle missing thus the missing

[7]Mis-identified beam photon means this event was caused by an untagged, low-energy photon but assigned a tagged, high-energy photon in the reconstruction. Since the beam photon is nearly along the z direction, this misidentification adds excessive p_z but little p_{trans} to the system.

momenta in both directions are small. A missing momentum cut of

$$mmPt \geq 80\, MeV/c \tag{3.8}$$

was therefore applied to reject these two categories of events. The shaded region in figure 3.6 shows the mm^2 distribution after the missing momentum cut.

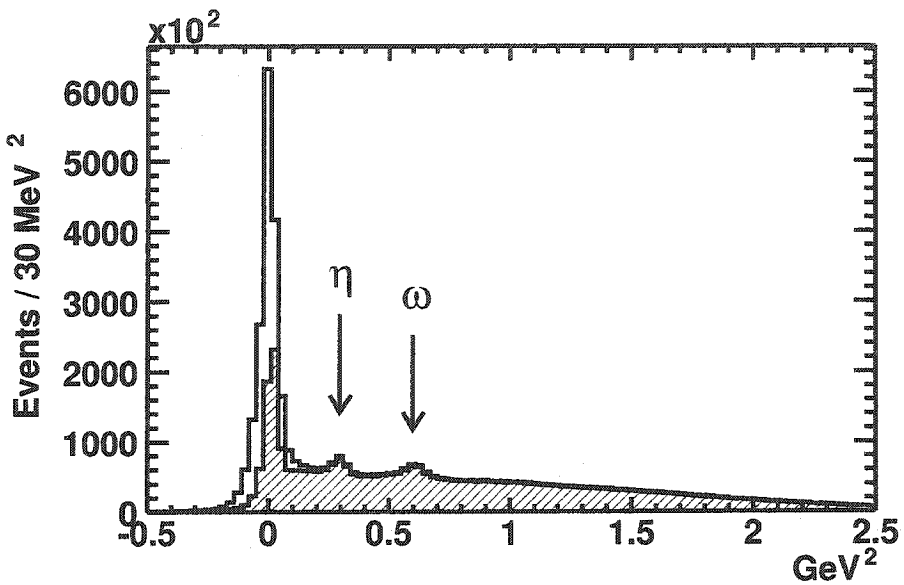

Figure 3.6: The mm^2 off of the $p\pi^+\pi^-$ system. Events in the shaded region passed the missing momentum cut.

Another source of topological background is multi-π^0(primarily two-π^0) production. The missing momentum cut can not get rid of these events. To suppress background of this kind, we required the number of photons measured in the electromagnetic calorimeters(EC) to be less than three.

3.5 Momentum Correction

Due to the finite resolution of the charged particle tracking system and the limited capability of the tracking algorithm, the reconstructed four-momenta of the charged particles have both systematic and statistical uncertainties. The primary goal of the momentum correction is to take out the systematic uncertainty in an

empirical manner.

The G6C experiment ran with a two-charged-particle trigger, as mentioned in the last chapter, which makes the momentum correction a bit complex. The momentum correction procedure discussed here was specifically designed for this experiment. A multi-step, *bootstrapping* procedure was used for obtaining the momentum correction coefficients.

In this procedure, the correction coefficients for different particles are obtained from a sequence of different reaction channels. Consider the reaction,

$$\gamma p \rightarrow X(mp) \tag{3.9}$$

where mp denotes a missing particle which is either a stable particle such as a pion or a narrow resonance such as an ω, and X is the particle under investigation. Assuming CLAS measures the angles right, one can then calculate the three-momentum, $p_{calculate}$, of X by demanding that the missing mass of mp equal the nominal value. The difference between the measured three-momentum, $p_{measure}$ and the calculated three-momentum

$$\delta p = p_{measure} - p_{calculate} \tag{3.10}$$

is fitted with the functional form [8]

$$\delta p = F_0 + F_1 \cos\theta + F_2 p_{measure} + F_3 \cos^2\theta + F_4 p_{measure}^2 + F_5 p_{measure} \cos\theta \tag{3.11}$$

where θ is the polar angle in the laboratory reference frame, and the Fs are the correction coefficients. The six CLAS sectors are fitted separately, therefore for a given particle there are six sets of Fs.

In each step the correction obtained in the previous step is applied first. Table 3.1 lists the reaction channels used for obtaining the correction coefficients for different particles and the *order* in which these steps were carried out.

In the process of studying the momentum correction, we also found that the photon beam energy was slightly mis-measured. Therefore a $+0.2\%$ correction on

[8]The choice of the functional form was arbitrary. The ϕ dependency is dropped out of the function because study shows it is weak.

Step	Reaction	Corr. Applied On	Coefficients Obtained For
1	$\gamma p \to p(\omega)$	—	$X = p$
2	$\gamma p \to p\pi^+(\pi^-)$	p	$X = \pi^+$
3	$\gamma p \to p(\pi^+)\pi^-$	p, π^+	$X = \pi^-$

Table 3.1: Reaction channels used for obtaining the momentum correction coefficients.

the measured beam energy was also applied on an event-by-event basis. Figure 3.7 shows the effect of the momentum correction.

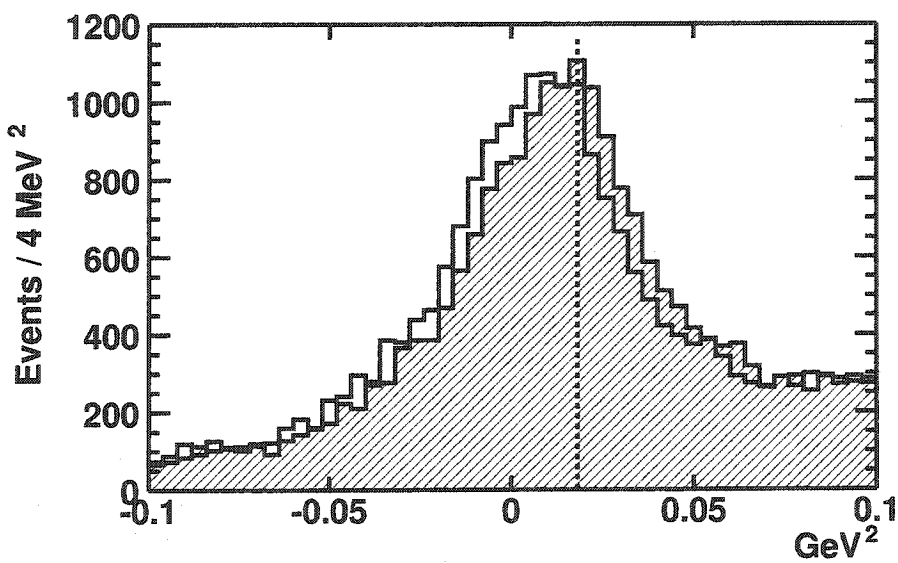

Figure 3.7: The mm^2 off of $p\pi^+\pi^-$. The peak shows the missing π^0. The shaded histogram is for events after the momentum correction. In this case, the momenta of the proton, π^+ and π^- as well as the photon beam energy were corrected. The dashed line indicates the nominal value of the π^0 mass.

It is clear that the missing π^0 peak is shifted systematically to the right direction. However, the width of the missing π^0 peak did not improve significantly. This suggests that our momentum correction procedure handles the systematic errors fairly well but other means are needed to make the overall mass resolution better.

3.6 Missing Mass Cut

A cut around the missing π^0 mass was applied on the momentum corrected data to pick out events that are topologically consistent with reaction (3.4). Figure 3.8 shows the mm^2 off of the $p\pi^+\pi^-$ system after the momentum correction. A Gaussian plus second-order polynomial function was fitted to the missing π^0 peak, yielding $0.012\,GeV^2$ for the mean and $0.021\,GeV^2$ for the σ of the Gaussian. A $\pm 2\sigma$ cut around the mean value was used as indicated by the two dashed lines in the plot. Based on this fit, we estimate a background contamination of $\sim 28\%$ surviving the cut. These events are subject to the kinematic fitting discussed in the next section.

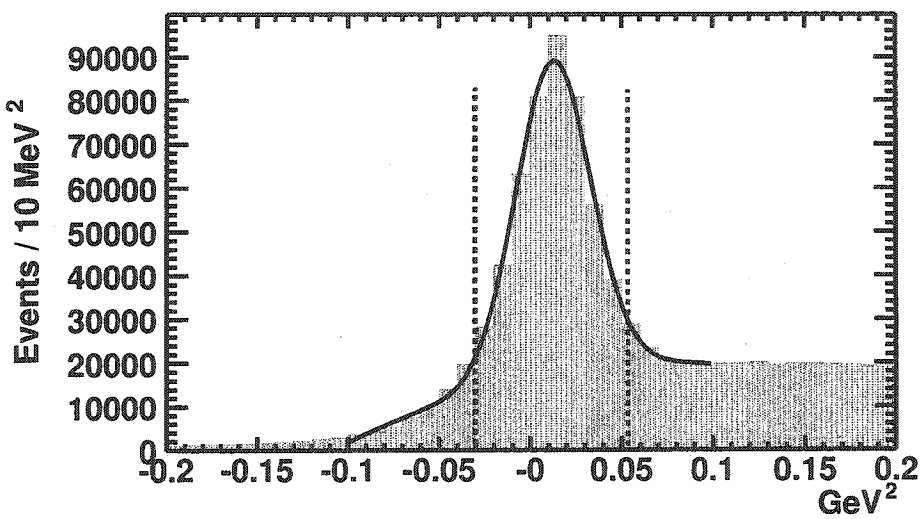

Figure 3.8: The mm^2 off of $p\pi^+\pi^-$. Events in this plot have passed all the cuts described in the previous sections. A Gaussian plus second-order polynomial fit was performed on the missing π^0 peak. The dashed lines show the $\pm 2\sigma$ cut around the mean of the Gaussian.

3.7 Kinematic Fitting

To improve the mass resolution and help reject topological background events, a kinematic fit was performed on the momentum corrected data. This is a con-

strained least χ^2 fit with correlated errors taken into account [76, 86].

The advantage of performing a kinematic fit is twofold. First, the χ^2 of the fit can be converted into a probability that our hypothesis about the reaction is incorrect, which then enables us to decide statistically whether or not to accept an event as an instance of the hypothesized reaction(*hypothesis testing*). Second, we obtain a better estimate of the kinematic variables because the fitted momenta are physically consistent, as required by the constraining equations(*parameter estimating*).

3.7.1 The Formalism

The algorithm used for the kinematic fitting is that of Roe [86]. The χ^2 is constructed, for measuring m variables $x_i, i = 1, \ldots, m$, as

$$\chi^2 = \sum_{j=1}^{m}\sum_{i=1}^{m}(x_{0i} - x_i)(\Lambda^{-1})_{ij}(x_{0j} - x_j) \tag{3.12}$$

where the x_0s are the true values, and Λ is the moment matrix.

If there are also c constraints, let the constraint equations be

$$f^k(\vec{y}, \vec{x}) = 0, \; k = 1, \ldots, c \tag{3.13}$$

here the $y_i, i = 1, \ldots, u$, represent u unknown parameters which correspond to the momenta of the missing particle. Then the χ^2 definition is modified by means of Lagrange multipliers to

$$\chi^2 = \sum_{j=1}^{m}\sum_{i=1}^{m}(x_{0i} - x_i)(\Lambda^{-1})_{ij}(x_{0j} - x_j) + 2\sum_{k=1}^{c} p_k f^k(\vec{y}, \vec{x}) \tag{3.14}$$

where the p_k are the Lagrange multipliers.

In our case, the reaction we are interested in is

$$\gamma p \rightarrow p\pi^+\pi^-(\pi^0) \tag{3.15}$$

where the π^0 in parenthesis indicates it is missing. The three-momenta of the measured particles are identified as $\vec{x}$ of equation (3.14). The three-momenta of

the missing π^0 form the unknown vector $\vec{y}$. And four-momentum conservation at the event vertex provides four constraint equations [9]. The number of degrees of freedom(NDF) for this particular fit is one(that is, four constraints less three missing variables), or a 1-c fit in the jargon.

Although this looks complicated, it is actually a linear fit and the minimization is carried out by iterative matrix inversion. The minimization procedure is very well documented in reference [86].

A useful relation, called a *pull*, is defined as [86]

$$\frac{(x_i - x_i^*)}{\sqrt{\sigma^2_{unfitted} - \sigma^2_{fitted}}} \tag{3.16}$$

where x_i^* are the fitted values. It can be shown that if the errors are Gaussian distributed and there is no systematic bias, the pulls should be normally distributed with mean 0 and variance 1. In reality the pulls are often not normally distributed, which indicates that either the errors are badly estimated(the variance is not 1) or there is systematic error unaccounted for(the mean is not 0).

The goodness of the fit is checked with the pulls and with the χ^2-Confidence Level(CL) curve as in usual least χ^2 fits [76, 86, 60].

3.7.2 Estimate of the Errors

The crucial part in the kinematic fitting is to estimate the errors correctly. Incorrectly estimated errors can result in badly distributed pulls and confidence level. Because the tracking errors from the CLAS charged particle tracking program only include the intrinsic uncertainty of the drift chambers, they are often much smaller than any realistic estimate. For instance, the multiple scattering of the charged particles in the target cell and in the start counter as well as in the drift chambers are not taken into account in calculating the tracking errors.

We adopted an empirical approach for a better estimation of the errors on the charged particles. We assumed the errors on the measured three-momentum of a

[9]Since the particle identification(PID) is done separately, for each particle, only the three-momentum is being fitted. The energy of each particle is then calculated from its three-momentum and its mass. However, energy conservation at the event vertex still counts as one constraint.

particle come solely from the measurement of the magnitude of the three-momentum. And we further assumed the error is proportional to the measured three-momentum magnitude,

$$\sigma_{|\vec{p}|} = F \times |\vec{p}| \tag{3.17}$$

where $\vec{p}$ is the measured three-momentum, and F is an empirical constant to be determined later. Thus uncertainties in the B field are accounted for on an event by event basis.

One can then swim this error into the three components of $\vec{p}$ using the measured angles by following the normal error transformation method [76, 86]. This gives a 3×3 error matrix for a single particle with correlations among p_x, p_y and p_z [10]. In forming the final covariance matrix for the kinematic fit, these single particle error matrices are joined on the diagonal,

$$\begin{pmatrix} \Sigma_1 & 0 & 0 & 0 \\ 0 & \Sigma_2 & 0 & 0 \\ 0 & 0 & \ddots & 0 \\ 0 & 0 & 0 & \Sigma_m \end{pmatrix} \tag{3.18}$$

where $\Sigma_i, i = 1, \ldots, m$, are the single particle error matrices, and the $0s$ are 3×3 null matrices.

The value of F appearing in equation (3.17) is determined empirically. Each time the kinematic fitter was run a different value of F was tested. After the fit, the pulls as defined in the last section were checked along with the confidence level distribution. The value we eventually adopted is $F = 0.1\%$.

3.7.3 Fit Result and Confidence Level Cut

Figure 3.9 shows the *confidence level*(CL) distribution from the kinematic fit. The accumulated events at low confidence level are mostly events of wrong topologies. A 10% confidence level cut is used to cut out those events. This cut will also reject 10% of the 'good' events on a statistical basis. Since the Monte Carlo

[10] This correlation is still artificial. A different approach which parametrizes the errors in the sector coordinate system probably is more conceptually satisfactory.

events are also subject to the same cut, this cut will not bias our analysis. A rise at high confidence level in the plot indicates that for some of the events our estimated errors are larger than their true values, that is, a small fraction of the events is measured with well-known B field.

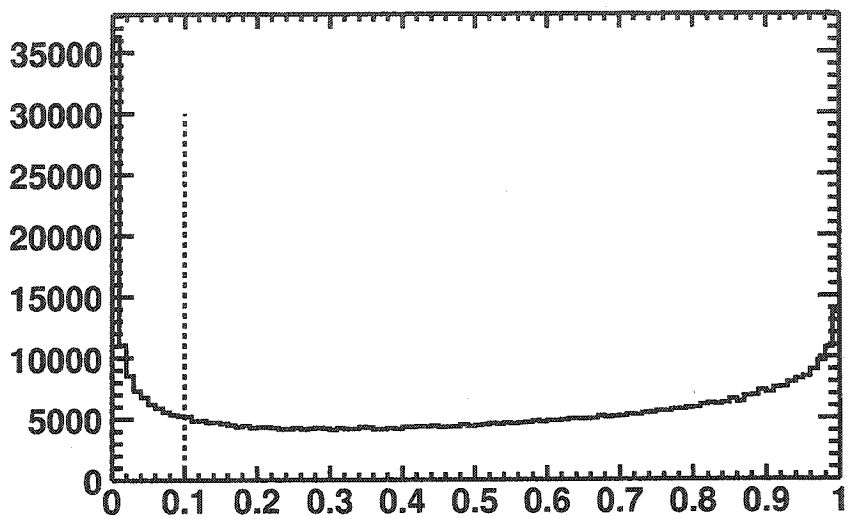

Figure 3.9: Confidence level of the kinematic fit. The dashed line marks the 10% confidence-level cut. The accumulated events at low confidence level are mostly events from reactions other than the hypothesized one. The rise at high confidence level indicates the errors for some of the events are estimated larger than their true values.

Figure 3.10 shows an example of the pull distribution. Shown in this plot is the pull for p_x of the proton. The dashed line is a Gaussian fit. The events in the middle that deviate from a Gaussian distribution correspond to the events at high confidence level in figure 3.9. The mean of this Gaussian fit is 1.2×10^{-3} which suggests that the systematic error is small. All the other pulls are similarly distributed. The small systematic errors demonstrate from another point of view that the momentum correction described in the last section did a fairly good job.

Figure 3.11 shows a comparison of the $\pi^+\pi^-\pi^0$ effective mass in the $\omega(782)$ region, before and after the kinematic fit, for events passed the confidence level cut.

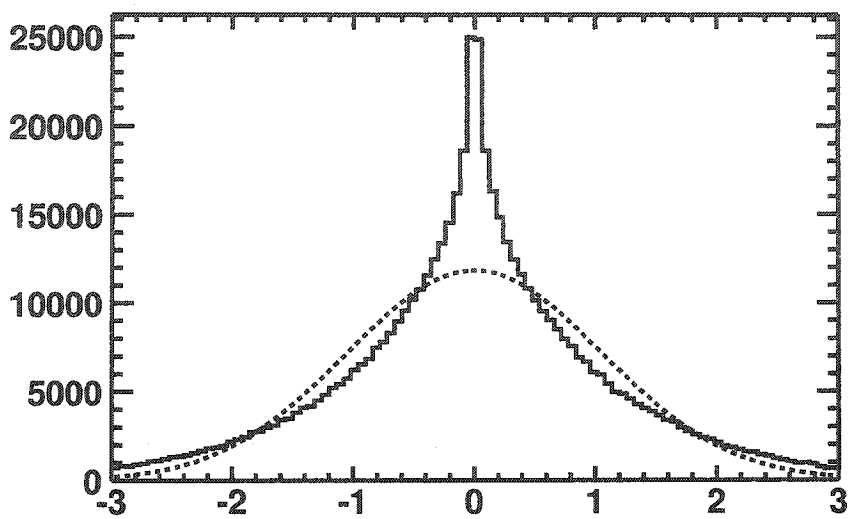

Figure 3.10: An example of the pull distribution from the kinematic fit. Shown in this plot is the pull for p_x of the proton. The events in the middle that deviate from a Gaussian distribution correspond to events with errors estimated larger than their true values. The mean of the Gaussian fit(the dashed line) is 1.2×10^{-3}.

An improvement in the width of the $\omega(782)$ peak is clear. Figure 3.12 shows a Breit-Wigner plus a second-order polynomial fit to the $\pi^+\pi^-\pi^0$ effective mass. The centroid of the Breit-Wigner is 784 MeV/c^2 and the width is 58 MeV/c^2. This fit is only semi-quantitative because the fit parameters depend on the parametrization of the background. However, it does give us a handle on estimating the mass resolution. Compared with the 8 MeV/c^2 width of the $\omega(782)$, our estimate of the $\pi^+\pi^-\pi^0$ effective mass resolution is about 60 MeV/c^2(FWHM). This mass resolution will be considered in choosing the mass bin size in the partial wave analysis.

3.8 $p\pi$ Mass and Baryon Cut

The reaction we are interested in is t-channel meson production, as depicted in diagram 3.13. In this reaction, the incident photon scatters off the spectator proton, producing a mesonic resonance R which then decays to the $\pi^+\pi^-\pi^0$ final

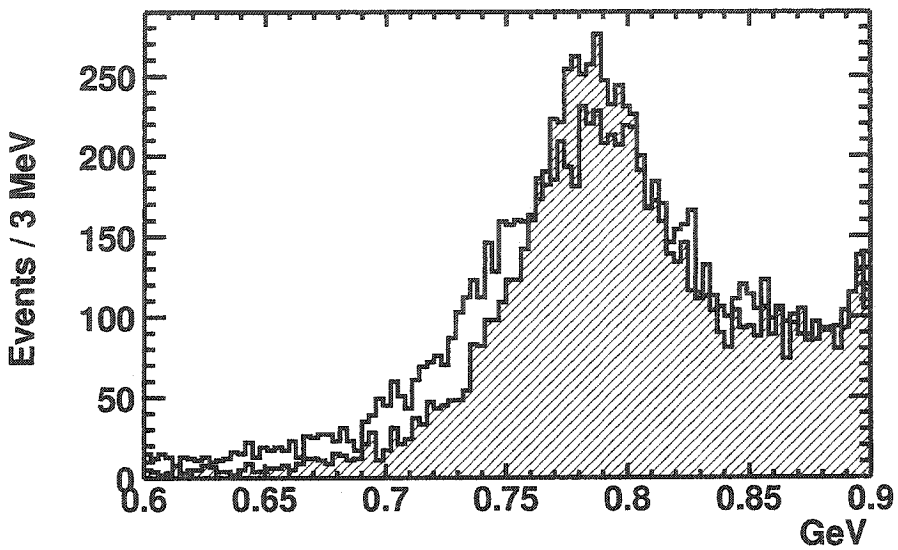

Figure 3.11: The effective mass of the $\pi^+\pi^-\pi^0$ system. The shaded histogram are events *after* the kinematic fit. A 10% confidence level cut is applied in both histograms. An improvement in the width of the $\omega(782)$ peak is clearly seen.

state. However, other diagrams do exit, such as the reaction shown in diagram 3.14. In this diagram, the incident photon excites the target proton to a Δ or an N^* which in-turn decays to a proton and a pion. At the meson vertex, a mesonic resonance is also produced but it decays into a two-pion final state. Reactions of this kind are referred to as *baryon background channels* in our study. Figure 3.15 shows the three $p\pi$ invariant mass combinations from the data. The $\Delta^{++}(1232)$ is evident in the $p\pi^+$ mass spectrum. In the $p\pi^0$ mass spectrum, the $\Delta^+(1232)$ is seen along with two small bumps around $1530\,MeV/c^2$ and $1650\,MeV/c^2$. The $\Delta^0(1232)$ shows up in the $p\pi^-$ mass spectrum only as a shoulder, but the states at $1530\,MeV/c^2$ and $1650\,MeV/c^2$ are relatively stronger than those in the $p\pi^0$ combination.

In principle, these two categories of reactions co-exist and they interfere with each other. This interference poses difficulties in our partial wave analysis. Therefore we want to reject events associated with diagram 3.14 without hurting events produced according to diagram 3.13. Figure 3.16 shows the correlation between the $p\pi$ system and their corresponding $\pi\pi$ system. Events with $p\pi$ effective mass less

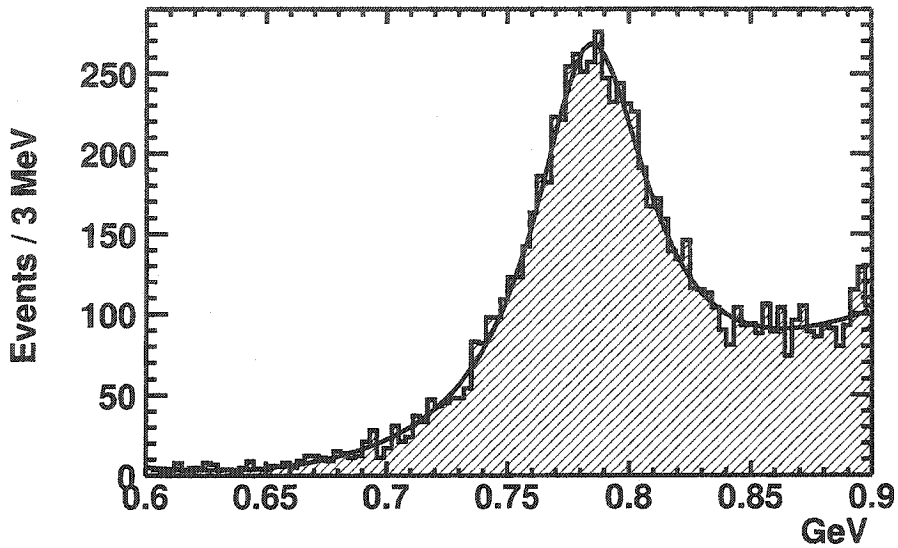

Figure 3.12: A Breit-Wigner plus second-order polynomial fit to the $\pi^+\pi^-\pi^0$ effevtive mass. The parameters of the Breit-Wigner function are $M_0 = 784\,MeV$, $\Gamma = 58\,MeV$. This suggests the three-pion effective mass resolution for this reaction channel is about $60\,MeV$.

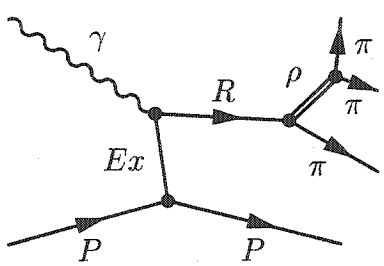

Figure 3.13: Feynman diagram for reaction $\gamma p \rightarrow p\pi^+\pi^-\pi^0$

than $1350\,MeV/c^2$ were rejected as indicated by the dashed lines in figure 3.16. This cut is referred to as the *baryon cut.* The shaded histograms in figure 3.15 show the $p\pi$ mass spectra after the baryon cut.

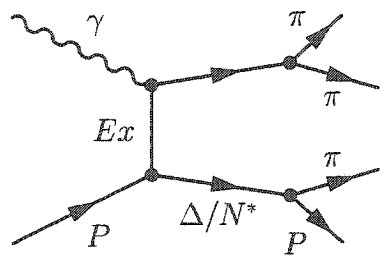

Figure 3.14: Feynman diagram for background reaction

3.9 The t' Distribution

The four-momentum transfer, $|t'|$, is defined as [83]

$$t' = t - t_{min} \tag{3.19}$$

where

$$t = (P^{\mu}_{target} - P^{\mu}_{recoil})^2 \tag{3.20}$$

and t_{min} is the value of t when the scattering angle is equal to 0. In reaction (3.4), t_{min} is given by

$$t_{min} = W_R^2 - 2E_\gamma E_R + 2p_\gamma p_R \tag{3.21}$$

where W_R is the mass of the $\pi^+\pi^-\pi^0$ system.

Figure 3.17 shows the $|t'|$ distribution from the data. It peaks strongly at low $|t'|$, which is consistent with the peripheral production picture sketched in diagram 3.13. A t' *cut* of

$$-1.0 < t' < -0.1\, GeV^2 \tag{3.22}$$

was applied. High t' events were rejected in order to achieve the smallest possible t' range for determining the t-averaged production amplitudes. Very low t' events were also rejected because those events correspond to low energy recoil protons, and low energy protons usually have bad tracking resolution and poorly determined acceptance in CLAS.

The t'-dependence of a peripheral production usually takes the form [83].

$$\frac{d\sigma}{dt'} = Ae^{-b|t'|} \tag{3.23}$$

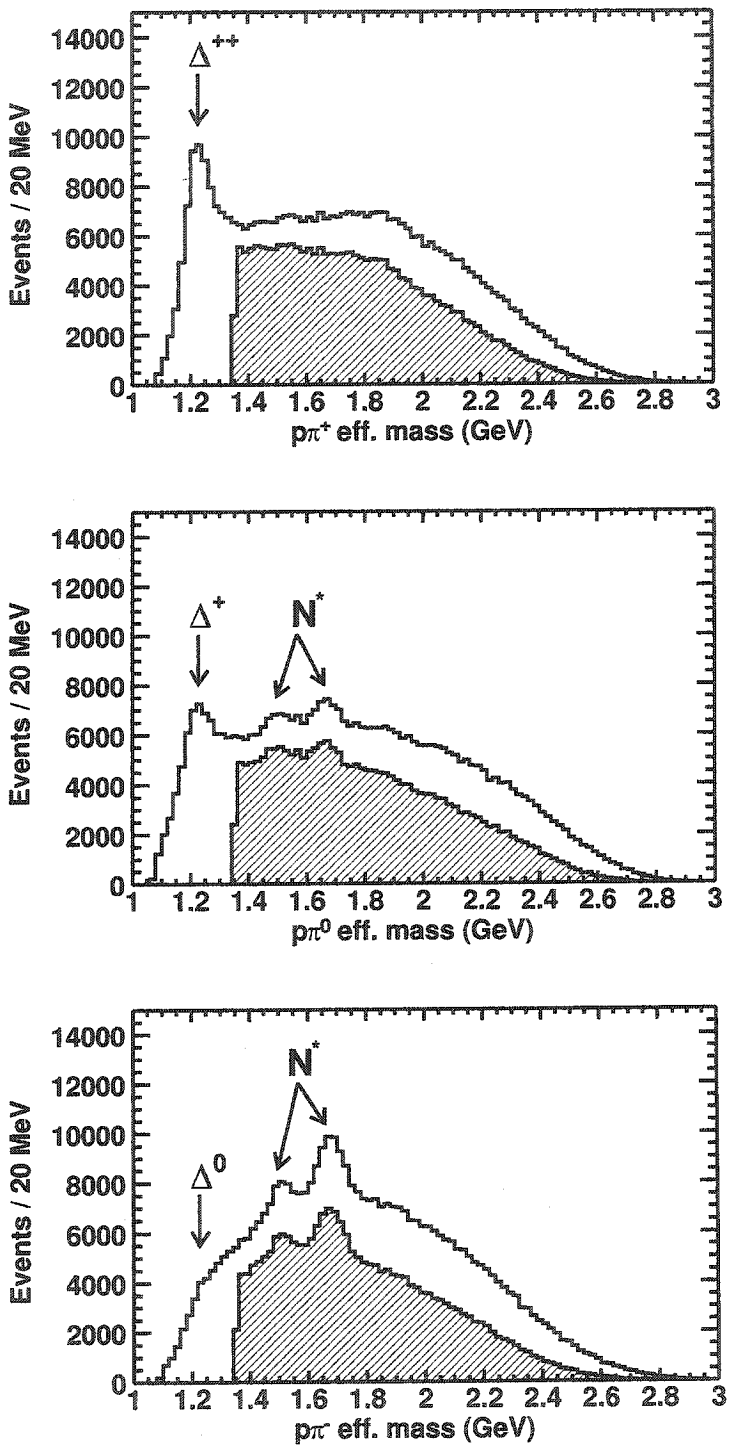

Figure 3.15: The mass spectra of three different $p\pi$ combinations. The shaded regions contain events after the baryon cut.

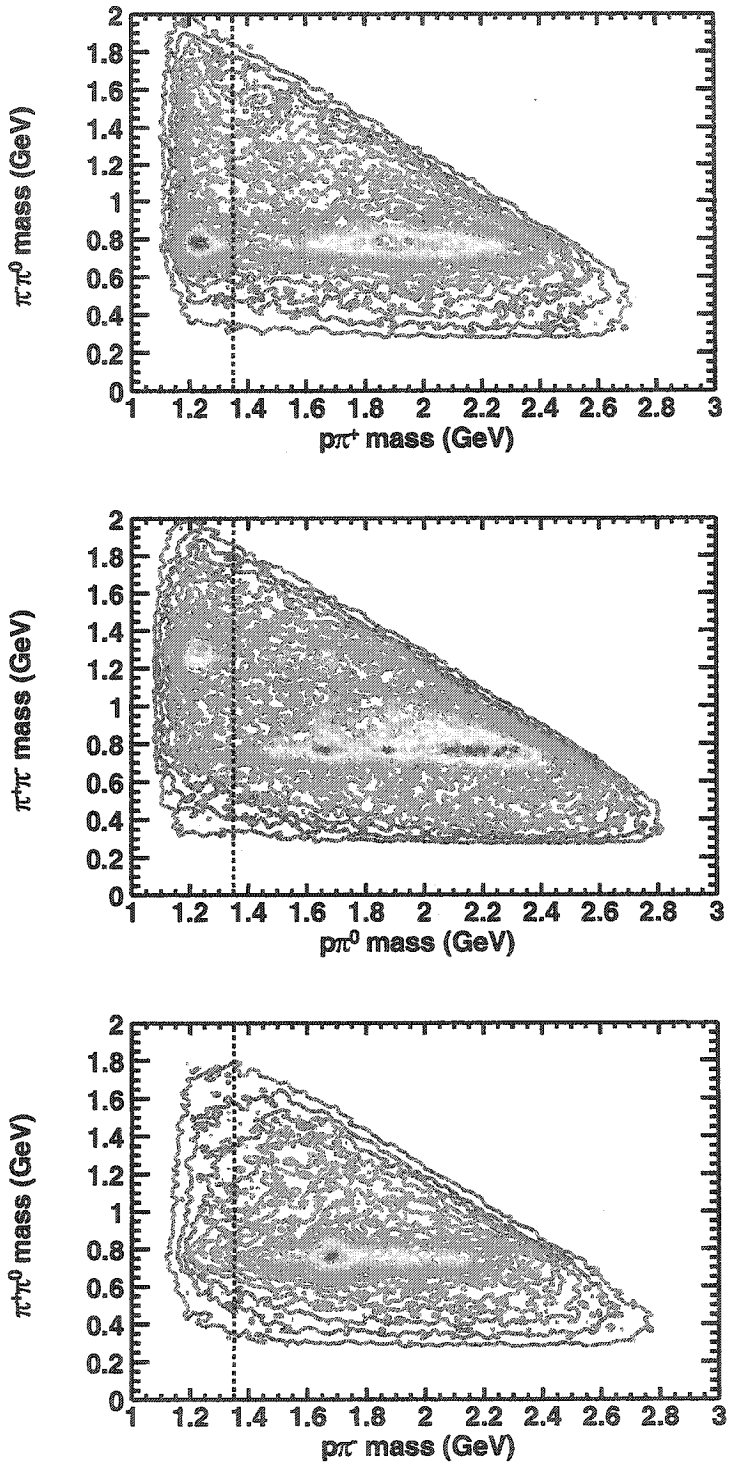

Figure 3.16: Correlation between the $p\pi$ system and their corresponding $\pi\pi$ system, as suggested by diagram 3.14. The $\Delta^{++}(1232)$ in the top plot is clearly correlated with the $\rho^-(770)$. The middle plot shows a correlation between the $\Delta^+(1232)$ and the $f_2(1270)$.

An exponential fit to figure 3.17 gives a slope of $b = 1.2\,GeV^{-2}$.

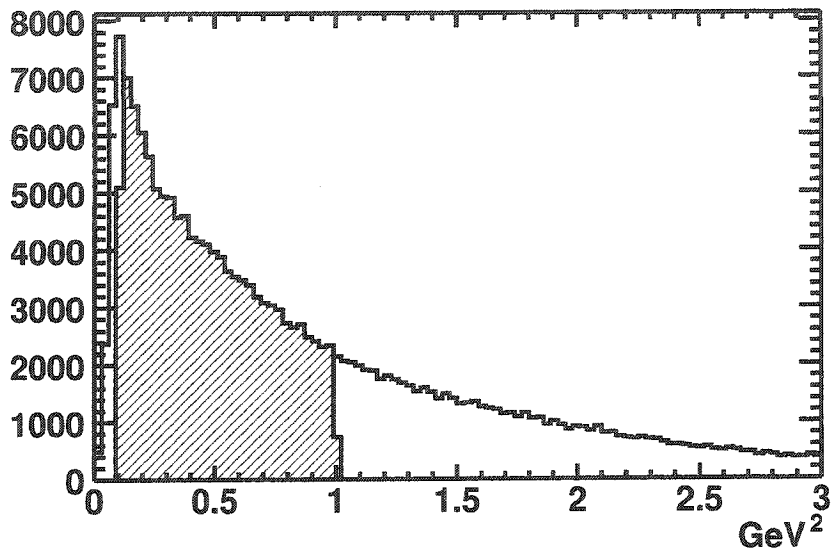

Figure 3.17: The four momentum transfer, $|t'|$, distribution. It is strongly peaked at low $|t'|$ which is consistent with a peripheral production picture. Events outside of the shaded region are rejected as a result of the t' cut.

3.10 $\pi\pi$ Mass Spectra

The $\pi\pi$ system effective masses are shown in figure 3.18. The shaded regions contain events after the baryon cut and the t' cut. The $\rho^{\pm,0}(770)$ dominate in all three combinations. In the $\pi^+\pi^-$ system, the $f_2(1270)$ is also present. However, after the baryon cut and the t' cut, the f_2 peak is reduced significantly. This is consistent with the observation in the middle plot in figure 3.16 — the f_2 is highly correlated with the $\Delta^+(1232)$.

3.11 $\pi^+\pi^-\pi^0$ Mass Sepctrum

Figure 3.19 shows the $\pi^+\pi^-\pi^0$ mass spectrum. Events before and after(shaded histogram) the baryon cut and the t' cut are shown in the same plot. The $\omega(782)$ dominates the spectrum below $1000\,MeV/c^2$, as expected. In the $1300\,MeV/c^2$

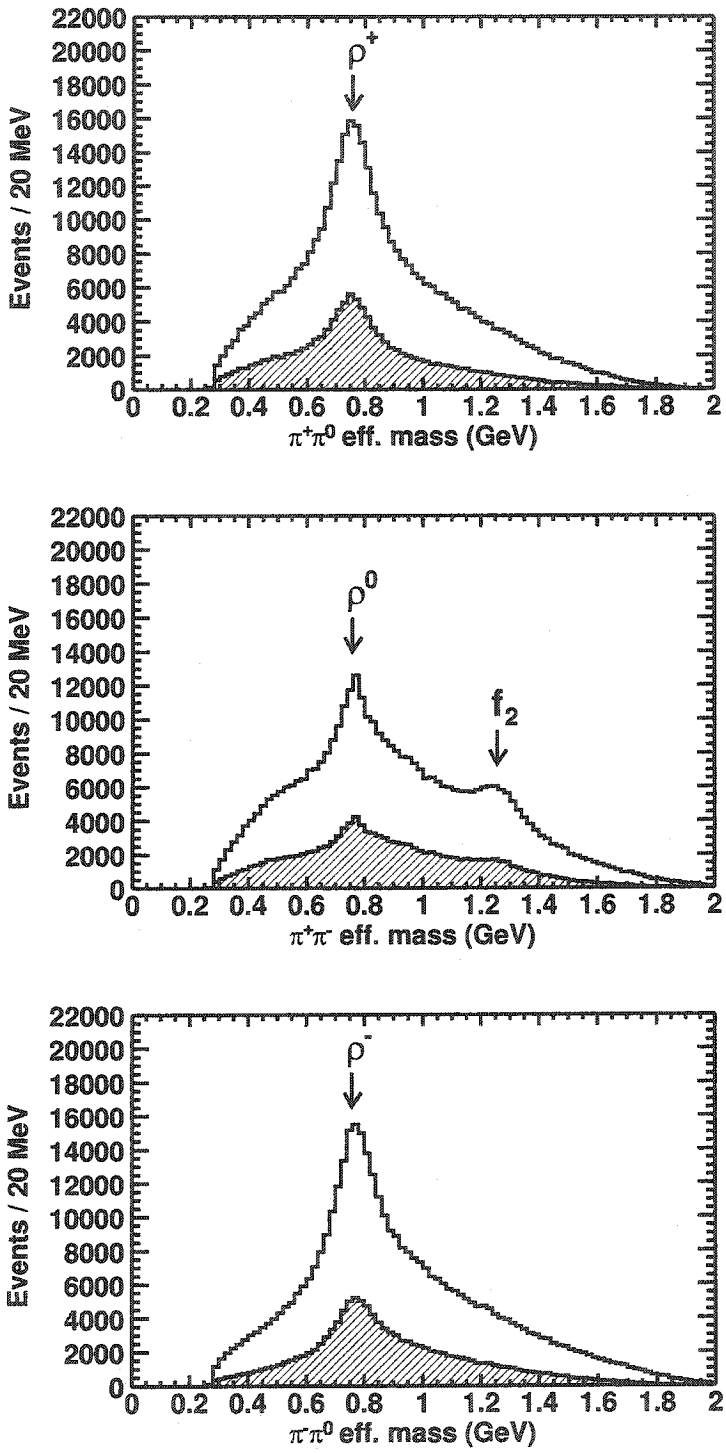

Figure 3.18: The di-pion system mass spectra. $\rho(770)$ dominates the spectrum in all cases. The $f_2(1270)$ is also seen in the $\pi^+\pi^-$ system. The shaded histograms contain events after the baryon cut and the t' cut. The f_2 strength is significantly reduced by these two cuts.

region, the combination of $a_1(1260)$ and $a_2(1320)$ is clearly seen. An enhancement around 1700 MeV/c^2 indicates the possible presence of $\pi_2(1670)$, $\omega(1650)$, $\omega_3(1670)$ and the exotic $\pi_1(1600)$. A shoulder at around 2 GeV/c^2 can also be seen. We will need to perform a partial wave analysis to understand the details of this spectrum.

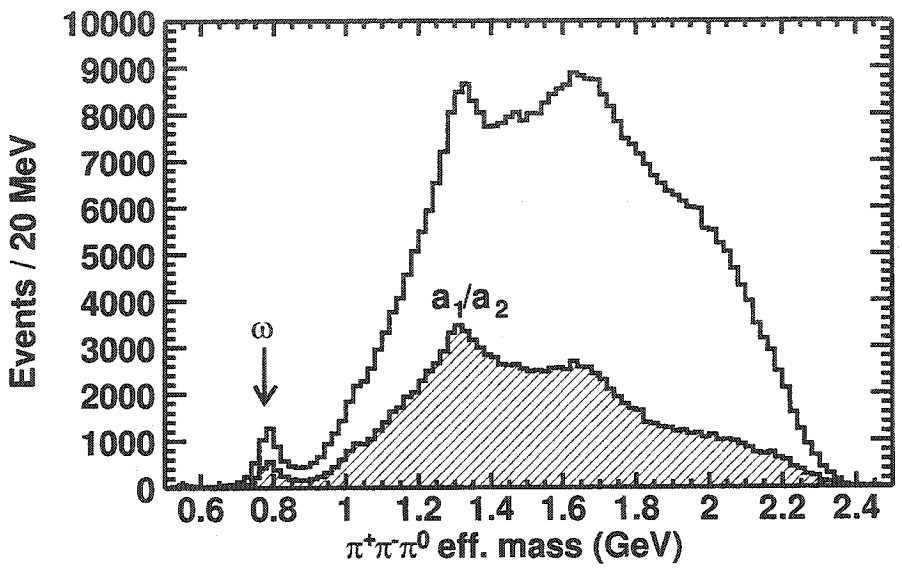

Figure 3.19: The $\pi^+\pi^-\pi^0$ effective mass. The shaded histogram shows events after the baryon cut and the t' cut. $\omega(782)$ dominates the spectrum below 1000 MeV/c^2. The combination of $a_1(1260)$ and $a_2(1320)$ is clearly shown in the 1300 MeV/c^2 mass region. The enhancement between 1600 MeV/c^2 and 1800 MeV/c^2 suggests the possible presence of $\pi_2(1670)$, $\omega(1650)$, $\omega_3(1670)$ and the exotic $\pi_1(1600)$.

CHAPTER 4
PARTIAL WAVE ANALYSIS

4.1 Introduction

To better understand the details of the $\pi^+\pi^-\pi^0$ spectrum as seen in figure 3.19, a full *partial wave analysis*(PWA) was performed on the final data sample. Partial wave analysis is a technique that uses the angular distribution of particles produced in hadronic reactions to determine the quantum numbers and decay properties of resonances which decay to those observed particles in the final state. It is the best method to analyze complicated systems where more than one resonance state may be present and overlapping. The PWA method discussed here is based on the *Isobar model* [62]. In this chapter, a brief discussion of the partial wave analysis formalism is given, followed by the results of the analysis.

4.2 Formalism

4.2.1 Intensity Distribution

Consider the production of a resonance R in the t-channel, followed by its decay into three pions,

$$\gamma p \rightarrow pR, \; R \rightarrow \pi^+\pi^-\pi^0 \tag{4.1}$$

as depicted in diagram 4.1.

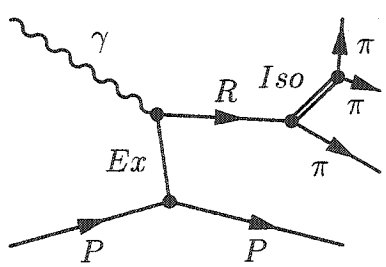

Figure 4.1: Diagram for reaction $\gamma p \rightarrow pR$, $R \rightarrow \pi^+\pi^-\pi^0$. Iso represents the isobar in the sequential decay of R.

Let W and w represent the mass of the resonance R and the mass of the

isobar, respectively. The Lorentz-invariant phase space element for this process is given by [84, 33, 35],

$$d\rho \propto d\Omega^* \, (p \, d\Omega \, dW) \, (q \, d\Omega_h \, dw) \tag{4.2}$$

where $\Omega^* = (\theta^*, \phi^*)$ represents the polar and azimuthal angles of R in the overall center-of-mass(CM) reference frame; $\Omega = (\theta, \phi)$ are the polar and azimuthal angles of the isobar in the R rest frame(RRF), and $\Omega_h = (\theta_h, \phi_h)$ are the polar and azimuthal angles of one of the isobar decay products in the isobar rest frame(IRF)(c.f. Appendix B), p denotes the momentum of the isobar in the three-pion rest frame(RRF) and q denotes the momentum of one of the decay products of the isobar in its helicity frame(IRF).

The differential cross section for reaction (4.1) thus can be written as,

$$\frac{d\sigma}{dt \, dW \, d\tau} \propto |\mathcal{M}|^2 pq \tag{4.3}$$

where

$$\tau = \{\Omega, \Omega_h, w\} \tag{4.4}$$

denotes collectively the kinematic variables that are relevant to partial wave analysis. The invariant amplitude $\mathcal{M}$ is a matrix element of the transition operator, $\hat{T}_{fi}$, which transforms the initial state $|i\rangle$ into the final state $|f\rangle$.

$$\mathcal{M} = \langle f|\hat{T}_{fi}|i\rangle \tag{4.5}$$

The isobar model [62] assumes that $\hat{T}_{fi}$ is the product of a production operator $\hat{T}_{mi}$ and a decay operator $\hat{T}_{fm}$, and the transition amplitude becomes

$$\mathcal{M} = \sum_m \langle f|\hat{T}_{fm}|m\rangle\langle m|\hat{T}_{mi}|i\rangle \tag{4.6}$$

where we have inserted a complete set $|m\rangle$, which represents a set of basis states with properties obeyed in strong interactions.

The *intensity distribution*, defined as

$$I(\tau) = |\mathcal{M}|^2 \tag{4.7}$$

can then be written as

$$I(\tau) = \sum_{\beta} |\sum_{\alpha} V_{\alpha\beta} A_{\alpha\beta}(\tau)|^2 \tag{4.8}$$

where τ is defined in equation (4.4); α represents a set of *internal quantum numbers*, such as the spin of the intermediate resonance, that interfere with each other; β represents a set of *external quantum numbers*, such as the spin orientation of the incoming and outgoing particles, whose values do not interfere.

$A_{\alpha\beta}(\tau)$ is called the *decay amplitude*, it can be calculated with appropriate hypothesis on an event by event basis [35, 55]. $V_{\alpha\beta}$ is called the *production amplitude*, it is unknown and is varied as a free parameter to best fit the observed intensity distribution. The unknown decay strength for each partial wave is also factored out from the intensity distribution and included in $V_{\alpha\beta}$.

In our analysis, these amplitudes are expressed in the *reflectivity* basis [35, 34] which takes into account parity conservation in the production process. The definition of the reflectivity basis and the mathematical simplification gained by using this basis are covered in detail in Appendix A. The use of the reflectivity basis introduces a new quantum number — the *reflectivity* ϵ.

In the reflectivity basis, the intensity distribution reads,

$$I(\tau) = \sum_{\epsilon,\kappa} |\sum_{\alpha} {}^{\epsilon}V_{\alpha\kappa}\, {}^{\epsilon}A_{\alpha\kappa}(\tau)|^2 \tag{4.9}$$

where κ is a sub-set of the external quantum numbers β of equation (4.8),

$$\beta = \{\epsilon, \kappa\} \tag{4.10}$$

Because parity conservation is taken into account in forming the reflectivity basis, amplitudes of different reflectivities do not interfere with each other [34].

4.2.2 Extended Maximum Likelihood Fit

An *extended maximum likelihood fit* [46, 80, 76, 86, 53] was used to determine the production amplitudes. The basics of the extended maximum likelihood method are described in Appendix C. Considering equation (C.6), we can construct the likelihood function for our specific problem as [55],

$$\mathcal{L} = e^{-\bar{N}_0} \prod_i^{N_0} I(\tau_i) \tag{4.11}$$

where $\bar{N}_0$ is the expected number of events if the same experiment were repeated many times,

$$\bar{N}_0 = \int I(\tau)\eta(\tau)pqd\tau \tag{4.12}$$

here $\eta(\tau)$ represents the experimental acceptance and $pqd\tau$ is the Lorentz-invariant phase space factor. Inserting equation (4.9) into equation (4.12) leads to,

$$\bar{N}_0 = \sum_{\epsilon,\kappa,\alpha,\alpha'} {}^{\epsilon}V_{\alpha\kappa}{}^{\epsilon}V^*_{\alpha'\kappa} \int {}^{\epsilon}A_\alpha(\tau){}^{\epsilon}A^*_{\alpha'}(\tau)\eta(\tau)pqd\tau \tag{4.13}$$

The integral over the decay amplitudes in equation (4.13) is often called the *accepted normalization integral*,

$${}^{\epsilon}\Phi^{acc}_{\alpha\alpha'} = \int {}^{\epsilon}A_\alpha(\tau){}^{\epsilon}A^*_{\alpha'}\eta(\tau)pqd\tau \tag{4.14}$$

and is evaluated using Monte Carlo simulation. The experimental acceptance, $\eta(\tau)$, is also determined from the Monte Carlo simulation,

$${}^{\epsilon}\Phi^{acc}_{\alpha\alpha'} = \frac{1}{N_{raw}} \sum_i^{N_{acc}} {}^{\epsilon}A_\alpha(\tau_i){}^{\epsilon}A^*_{\alpha'}(\tau_i) \tag{4.15}$$

where N_{raw} is the number of raw Monte Carlo events generated and the summation is over the accepted Monte Carlo events, that is, those that would be detected. The Lorentz-invariant phase space factor is taken care of by generating Monte Carlo events which are uniformly distributed in phase space.

The quantity which is being maximized in the fit is the logarithm of the ex-

tended likelihood function [11].

$$\ln \mathcal{L} = \sum_{i}^{N_0} \ln(\sum_{\epsilon,\kappa,\alpha,\alpha'} {}^{\epsilon}V_{\alpha\kappa}{}^{\epsilon}V^*_{\alpha'\kappa}{}^{\epsilon}A_{\alpha}(\tau_i){}^{\epsilon}A^*_{\alpha'}(\tau_i)) - \sum_{\epsilon,\kappa,\alpha,\alpha'} {}^{\epsilon}V_{\alpha\kappa}{}^{\epsilon}V^*_{\alpha'\kappa}{}^{\epsilon}\Phi^{acc}_{\alpha\alpha'} \tag{4.16}$$

The acceptance corrected number of events, $N_{corrected}$, can be calculated using the set of raw Monte Carlo events along with the production amplitudes obtained from the fit,

$$\bar{N}_{corrected} = \int I(\tau)pqd\tau = \sum_{\epsilon,\kappa,\alpha,\alpha'} {}^{\epsilon}V_{\alpha\kappa}{}^{\epsilon}V^*_{\alpha'\kappa}{}^{\epsilon}\Phi^{raw}_{\alpha\alpha'} \tag{4.17}$$

where ${}^{\epsilon}\Phi^{raw}_{\alpha\alpha'}$ is called the *raw normalization integral* and is given by

$${}^{\epsilon}\Phi^{raw}_{\alpha\alpha'} = \frac{1}{N_{raw}} \sum_{i}^{N_{raw}} {}^{\epsilon}A_{\alpha}(\tau_i){}^{\epsilon}A^*_{\alpha'}(\tau_i). \tag{4.18}$$

The acceptance corrected number of events attributed to a given state $|\alpha,\epsilon\rangle$ is

$$N_{|\alpha,\epsilon\rangle} = \sum_{\kappa} {}^{\epsilon}V_{\alpha\kappa}{}^{\epsilon}V^*_{\alpha\kappa}{}^{\epsilon}\Phi^{raw}_{\alpha\alpha}, \tag{4.19}$$

and the phase difference between two states $|\alpha,\epsilon\rangle$ and $|\alpha',\epsilon\rangle$ is [12]

$${}^{\epsilon}\phi_{\alpha\alpha'} = arg(\sum_{\kappa} {}^{\epsilon}V_{\alpha\kappa}{}^{\epsilon}V^*_{\alpha'\kappa}). \tag{4.20}$$

4.2.3 The PWA Program

This formalism was coded into a general PWA program by Cummings and Weygand [45, 46]. The minimization routine used in this program is the CERNLIB routine *Minuit* [97].

4.3 Monte Carlo

Monte Carlo event generation is a crucial part of the partial wave analysis. Both the accepted normalization integral and the raw normalization integral rely on Monte Carlo events. For this study, the Monte Carlo events were generated with

[11] In practice, $-\ln \mathcal{L}$ is minimized.

[12] The phase difference is meaningful only if these two states are produced coherently. In case of a multi-rank fit as discussed in section 4.5, there is no definitive way of defining the phase difference.

a phase space event generator called *ppgen*. The raw Monte Carlo events were fed into a GEANT based detector simulator called *GSIM*. GSIM is the standard CLAS simulator.

To reduce computing time and to match the Monte Carlo distributions to the data, the Monte Carlo events were generated with an exponential t dependence to the $\pi^+\pi^-\pi^0$ system, the slope used was $b = 3.0$. Events were generated in $10\,MeV/c^2$ three-pion mass bins. The fit was done with $80\,MeV/c^2$ bin size, however generating Monte Carlo events in narrower mass bins allows one to choose different bin sizes more conveniently later in the process and minimizes the effect of *bin migration* [13]. Events were generated from $1000\,MeV/c^2$ to $2200\,MeV/c^2$ in $\pi^+\pi^-\pi^0$ mass, with $200,000$ events in each bin. Figure 4.2 shows the over-all acceptance as a function of the $\pi^+\pi^-\pi^0$ invariant mass.

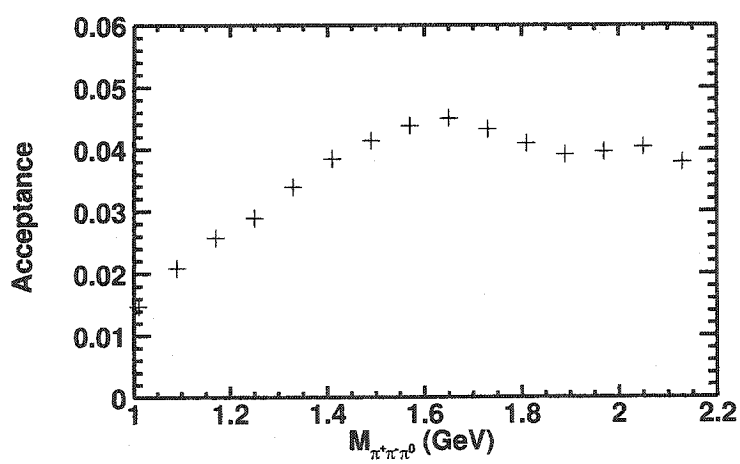

Figure 4.2: The over-all acceptance as a function of the $\pi^+\pi^-\pi^0$ invariant mass.

Also, the beam photon energy spectrum, figure 3.2, was used in generating the

[13] Due to finite mass resolution, events initially generated in a given bin can end up in neighboring bins after going through the detector simulator. This is referred to as bin migration. Bin migration biases the acceptance corrected number of events if not correctly accounted for. To minimize the bias caused by bin migration, events were generated in narrower mass bins than those used in the fit. After the bin size for the partial wave analysis fit was chosen, the Monte Carlo events in the corresponding bins were added and renormalized according to the number of data events in each bin. This procedure does not totally remove the bias produced by bin migration, however it reduces the bias and is very efficient.

Monte Carlo events. Doing so takes into account the cross section as a function of beam photon energy and makes the mass-dependent analysis a function of only the resonance parameters.

4.4 Allowed Partial Waves

The partial waves for describing the decay of the resonance R into $\pi^+\pi^-\pi^0$ final state are labeled by $\alpha = \{I^G J^{PC} M^\epsilon Isobar L\}$, where

- I is the isospin of R,
- G is the G-parity, as defined in equation (1.3), of R,
- J is the total angular momentum of R,
- P is the parity of R,
- C is the charge conjugation of R,
- M is the spin projection along the beam axis,
- ϵ is the reflectivity of R,
- $Isobar$ is the isobar used to describe the sequential decay of R,
- L is the orbital angular momentum between the isobar and the bachelor pion.

The $\pi^+\pi^-\pi^0$ system is necessarily a G-parity eigenstate, and its G-parity eigenvalue is fixed by the G-parity of the pions to be -1 [14]. Hence the isospin of R is determined by specifying the charge conjugation(C) of R, c.f. equation (1.12),

$$I = \begin{cases} 1 & \text{if } C = +1 \\ 0 & \text{if } C = -1. \end{cases} \tag{4.21}$$

Because the $\pi^+\pi^-\pi^0$ is a charge neutral system, both iso-vector($I = 1$) and iso-scaler($I = 0$) states are allowed.

[14] The G-parity of pion is -1, and G-parity is a multiplicative quantum number. Therefore, for a three-pion system the G-parity is -1.

The total spin, J, and orbital angular momentem, L, can be determined following the angular momentum addition rules, taking into account the spin of the isobar. The parity, P, is determined by the intrinsic parity of the isobar and the bachelor pion along with their relative orbital angular momentum,

$$P = P_{isobar} P_{bachelor} (-)^L \tag{4.22}$$

The spin projection, M, was restricted to $M \leq 2$ based on the belief that in peripheral photoproduction the helicity change at the baryon vertex does not impart more than $M = 1$ amplitudes on the meson resonances. However, this is not rigorously proved. Also, from a practical point of view, restricting M value reduces the number of partial waves significantly. Both reflectivities, $\epsilon = \pm 1$, were allowed. For $M = 0$ partial waves, only one reflectivity can exist(see Appendix A).

Inspired by figure 3.18, $\rho(770)$, $f_2(1270)$ and $\sigma(\pi\pi$ S-wave) were included as isobars. In constructing the decay amplitudes, the isospins of the isobar and the bachelor pion were taken into account by appropriate weighting with the Clebsch-Gordan coefficients in isospin space.

In principle, there are an infinite number of allowed partial waves which form a complete basis. Ideally one would like to use all possible partial waves and let the fit decide which ones are important. However, with finite statistics, only a few of the partial waves can be tried at a time. Also, one does not expect to see mesons with high spin in the $1\,GeV/c^2$ to $2\,GeV/c^2$ mass region [60]. Therefore we restricted the total spin, J, to be less than 4. The choice of the orbital angular momentum, L, was also limited to the lowest allowed value because of the centrifugal barrier raised by high L and the limited phase space in this mass region.

4.5 Rank Consideration

The spin projections of the beam photon and the target proton as well as the recoil proton are not measured. Therefore they need to be summed and averaged over in calculating the cross section. Since each of these particles has two possible spin projections, there are eight different production amplitudes associated with one

decay amplitude of a mesonic resonance R(c.f. diagram 4.1). However, reflection symmetry ties some of these production amplitudes together(Appendix A) and reduces the number to four. The number of production amplitudes corresponding to one decay amplitude of R is called *rank* [15]. The process we are analyzing is therefore a *rank-4* process.

Practically, a rank-4 process means for a given decay amplitude we need four independent complex parameters in each reflectivity in the partial wave analysis. This is a lot of parameters! With our limited statistics we cannnot determine such a large number of parameters.

If the resonance R were produced with one column of its spin-density matrix dominating, one could then ignore the other columns and treat it as a rank-1 process. This is exactly the assumption we made. This assumption allows us to reduce the number of free parameters in the fit by a factor of four for any partial wave set.

Reducing rank is also a common practice in hadron beam analysis [37]. It is worth noting that using rank-1 does not imply the spin-density structure of R is the same in each mass bin.

4.6 Parametrization of Background

The partial waves discussed in the last section correspond to events produced according to diagram 4.1. These are the events containing the physics that we are interested in. We will call these partial waves the *foreground waves* from now on.

However, as discussed in section 3.8, other diagrams contribute too. Diagram 4.3 depicts the most important background channel to our analysis. In this

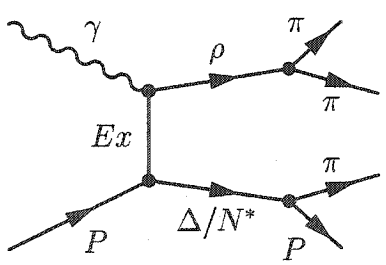

Figure 4.3: Feynman diagram for background reaction

[15]This is actually the dimension of the spin-density matrix $^{\pm}\rho$ in Appendix A.

diagram the beam photon excites the target proton to a baryon resonance(Δ or N^*) and the baryon resonance then decays to a proton and a pion. At the meson vertex, a mesonic resonance(a ρ for instance) is produced peripherally and decays in-turn into two pions. These background channels interfere with the foreground channels.

To suppress the contamination of these background events, we applied certain kinematic cuts in our data reduction procedure(c.f. section 3.8). However, those cuts can not get rid of all the background events. Therefore we have to accommodate events from background channels with appropriate parameterization in our partial wave analysis.

Different approaches were tried, including an isotropic background term in the fit as well as the SAID parameterization for the baryon resonances. These methods all worked to some level but were not satisfactory in the sense that the fitted distributions did not agree with the data very well.

After close examination of the problem and extensive tests, we decided to use a phenomenological parameterization for the background. In this approach, the baryon resonances are represented by simple Breit-Wigner shapes with their means and widths taken from the PDG particle table. Table 4.1 lists the baryon resonances used in the fit. These states were chosen because they are present as mass peaks in the data(see figure 3.15 [16]). The mesonic resonance at the upper vertex in

Baryon Resonance	Mass (MeV/c^2)	Width (MeV/c^2)
$\Delta^{++,+}$	1232	120
$N^{*+,0}$	1650	150
N^{*0}	1535	150

Table 4.1: List of baryon resonances used to parameterize the background channels.

diagram 4.3 was modeled as the $\rho(770)$ meson. All allowed spin projections of the $\rho(m = 0, \pm 1)$ along the quantization axis were included. The angular distribution between the baryon resonance and the ρ was taken to be exponential. The slope

[16]The $\Delta(1232)$ is clearly identified in the data, figure 3.15. However, the N^* states at $1650\,MeV/c^2$ and $1530\,MeV/c^2$ can not be unambiguously identified. Nevertheless, since we are parameterizing the baryon states with simple Breit-Wigner function and the widths of these overlapping N^* states are comparable, the minor difference between these N^* states can be ignored.

for this exponential term is obtained by a fit to the data. Symbolically the decay amplitude can be written as

$$A = A_\rho \times A_{baryon} \times e^{-bt/2}. \tag{4.23}$$

We will call these partial waves the *background waves* in later discussion.

The angular distribution between the proton and the pion in the baryon resonance decay was not included in constructing the decay amplitudes. The reason for doing so is two-fold. Firstly, the partial wave fit is done in the three-pion rest frame while integrating over the proton-pion mass. We believe this integration washes out most detailed information on the proton-pion angular distribution, therefore omitting these distributions in the decay amplitudes should not affect the fit too much. Secondly, incorporating these angular distributions would increase the number of parameters in the fit drastically. Therefore omitting them is a more practical choice given our limited statistics.

This parameterization of the baryon background channels works very well as will be demonstrated below. I would also like to point out that this is probably the first attempt to incorporate the baryon background channels in a partial wave analysis on a three-pion system produced with photons.

4.7 Local Maxima

As in many other fitting problems, we are also facing local maxima in our maximum likelihood fit. Due to the complexity of the likelihood space, sometimes this problem can be severe. Figure 4.4 shows an example.

To reduce the probability of taking a wrong answer which is associated with a local maximum, each fit was repeated fifty times for a given partial wave set. In each trial, the fitting parameters were initialized randomly and the solution corresponding to the largest likelihood value was taken as the final answer.

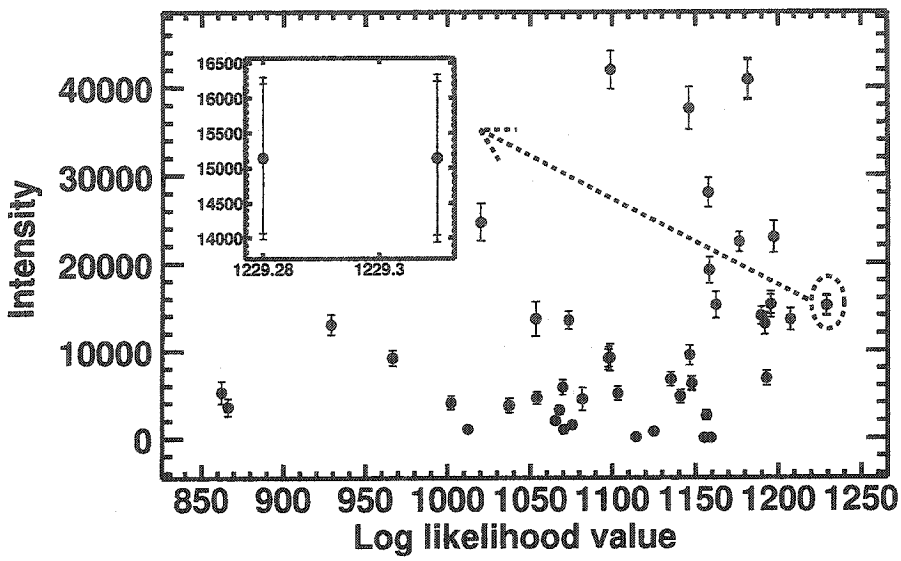

Figure 4.4: An example of the local maxima in a maximum likelihood fit. On the vertical axis is the acceptance corrected intensity of a given partial wave; on the horizontal axis is the log likelihood value. Fifty fits with the same partial wave set were tested, each time the fitting parameters were initialized randomly. Some of the solutions overlap as shown in the small window. Each point(or congregation of points) corresponds to a local maximum in the likelihood space. The solution with the largest log likelihood value was picked as the final answer.

4.8 Fit Results

In this section the partial wave analysis results for the $\pi^+\pi^-\pi^0$ system are presented. The PWA results are discussed in terms of the acceptance corrected yields for partial waves and the phase differences between partial waves.

4.8.1 Final Wave Set

The fit started with a relatively large partial wave set. After each fit, waves that were smaller than 1% of the total intensity were dropped. In a few cases, waves that were larger than 1% of the total were dropped either because those waves did not have recognizable structures, or because the presence of those waves worsened the agreement between the data and the fit predicted distributions. The objective

is to describe the data with the smallest partial wave set.

The background partial waves are listed in table 4.2. A total of twenty-one

Baryon resonance	m_ρ^ϵ
$\Delta^{++}(1232)$	$0^\pm$, $1^\pm$, $-1^\pm$
$\Delta^{+}(1232)$	$0^\pm$, $1^\pm$, $-1^\pm$
$N^{*+}(1650)$	$0^\pm$, $1^\pm$, $-1^\pm$
$N^{*0}(1650)$	0^+, 1^-, -1^+

Table 4.2: Background partial waves used in the final PWA fit. These partial waves were manifested in both reflectivities and allowed to interfere with the foreground waves. m_ρ is the spin projection of the ρ meson in its helicity reference frame.

background waves were used in the final fit. The construction of these partial waves was discussed in section 4.6. These background waves were manifested in both reflectivities [17], and they were allowed to interfere with the foreground partial waves in each reflectivity.

Table 4.3 lists the foreground partial waves used in the final fit. As mentioned earlier, with limited statistics only a few partial waves can be tried at a time. To reduce the ambiguity caused by too many parameters in the fit, the full $\pi^+\pi^-\pi^0$ mass range was divided into three regions, namely $1000 - 1560\,MeV/c^2$, $1480 - 1880\,MeV/c^2$ and $1800 - 2200\,MeV/c^2$. Adjacent mass regions overlap by one mass bin. The divisions were based on established knowledge of meson resonances from previous experiments. The number of partial waves increases from the lowest mass region to the highest region. This reflects the fact that the density of states increases with mass and that high spin resonances do not appear at low mass. In the low-mass region only $\rho\pi$ partial waves were included, while $f_2\pi$ waves were included above threshold.

4.8.2 Quality of Fit

Recalling equation (4.9), after the fit the production amplitudes, ${}^\epsilon V_{\alpha\kappa}$, are known. Equation (4.9) can then be used as a weighting function to give each ac-

[17] The decay amplitudes are the same for both reflectivities, but different production amplitudes were assigned for different reflectivities.

Foreground waves					
$\pi^+\pi^-\pi^0$ mass	I^G	J^{PC}	M^ϵ	L	Isobars
$1000 \sim 1560\, MeV/c^2$	1^-	1^{++}	$0^+, 1^\pm$	$0, 2$	$[\rho(770)]\pi$
(16 waves)	0^-	1^{--}	$0^-, 1^\pm$	1	$[\rho(770)]\pi$
	$\boldsymbol{1^-}$	$\boldsymbol{1^{-+}}$	$\boldsymbol{0^-, 1^+}$	$\boldsymbol{1}$	$\boldsymbol{[\rho(770)]\pi}$
	1^-	2^{++}	$0^-, 1^+$	2	$[\rho(770)]\pi$
	1^-	2^{-+}	$0^+, 1^\pm$	1	$[\rho(770)]\pi$
$1480 \sim 1880\, MeV/c^2$	1^-	1^{++}	$0^+, 1^\pm$	$0, 2$	$[\rho(770)]\pi$
(28 waves)	0^-	1^{--}	$0^-, 1^\pm$	1	$[\rho(770)]\pi$
	$\boldsymbol{1^-}$	$\boldsymbol{1^{-+}}$	$\boldsymbol{0^-, 1^+}$	$\boldsymbol{1}$	$\boldsymbol{[\rho(770)]\pi}$
	1^-	2^{++}	$0^-, 1^+$	2	$[\rho(770)]\pi$
	1^-	2^{-+}	$0^+, 1^\pm$	0	$[f_2(1270)]\pi$
			0^+	2	$[f_2(1270)]\pi$
			$0^+, 1^\pm$	$1, 3$	$[\rho(770)]\pi$
	$\boldsymbol{0^-}$	$\boldsymbol{2^{+-}}$	$\boldsymbol{0^-}$	$\boldsymbol{2}$	$\boldsymbol{[\rho(770)]\pi}$
	0^-	3^{--}	$0^-, 1^+$	3	$[\rho(770)]\pi$
	1^-	3^{++}	$0^-, 1^\pm$	1	$[f_2(1270)]\pi$
$1800 \sim 2200\, MeV/c^2$	1^-	1^{++}	$0^+, 1^\pm$	$0, 2$	$[\rho(770)]\pi$
(31 waves)	0^-	1^{--}	$0^-, 1^\pm$	1	$[\rho(770)]\pi$
	$\boldsymbol{1^-}$	$\boldsymbol{1^{-+}}$	$\boldsymbol{0^-, 1^+}$	$\boldsymbol{1}$	$\boldsymbol{[\rho(770)]\pi}$
	1^-	2^{++}	$0^-, 1^+$	2	$[\rho(770)]\pi$
	1^-	2^{-+}	$0^+, 1^\pm$	0	$[f_2(1270)]\pi$
			0^+	2	$[f_2(1270)]\pi$
			$0^+, 1^\pm$	$1, 3$	$[\rho(770)]\pi$
	$\boldsymbol{0^-}$	$\boldsymbol{2^{+-}}$	$\boldsymbol{0^-}$	$\boldsymbol{2}$	$\boldsymbol{[\rho(770)]\pi}$
	0^-	3^{--}	$0^-, 1^+$	3	$[\rho(770)]\pi$
	1^-	3^{++}	$0^-, 1^\pm$	1	$[f_2(1270)]\pi$
	1^-	4^{++}	$0^-, 1^-$	3	$[f_2(1270)]\pi$

Table 4.3: Foreground partial waves used in the final PWA fit. The meaning of the various quantum numbers is defined in section 4.4. The exotic partial waves are *italicized*.

cepted Monte Carlo event a weight. With proper normalization, the accepted Monte Carlo events with low weights are dropped. We thus obtain a set of accepted Monte Carlo events with which we can plot various mass and angular distributions. These distributions are called *fit predicted distributions*, and they should be a good representation of the data.

The goodness of fit is checked by comparing the fit predicted distributions with those of the data. For an acceptable fit, no large deviation in any of these

comparisons should be observed. Figure 4.5 through figure 4.7 show the comparison of invariant mass, Gottfried-Jackson angle and helicity angle distributions between the PWA predicted events and the data. For the majority of the distributions, the agreement is excellent. The largest deviation shows in $\cos\theta$ of the π^+ in the $\pi^+\pi^-$ helicity reference frame. This is possibly because of missing partial waves, or because the interference between the foreground waves and the baryonic background waves is not sufficiently accounted for. The dip in the ϕ angles in both the Gottfried-Jackson frame and the helicity frame is caused by CLAS acceptance. The overall agreement between the data and the fit is very good.

4.8.3 Partial Wave Intensities

Figure 4.8 shows the background-subtracted acceptance corrected yield [18] as a function of $\pi^+\pi^-\pi^0$ effective mass. Two peaks are clearly seen at around $1300\,MeV/c^2$ and $1700\,MeV/c^2$, respectively. Figure 4.9 shows the sum of all the background partial waves. A structure at $1600\,MeV/c^2$ can be seen. This bump is primarily due to one background partial wave [19] which does not interfere strongly with the foreground waves. The ratio of foreground to background is large at low mass and it decreases to about one at high mass.

Shown in figure 4.10 are the total intensities of the non-exotic isovector($I = 1$) waves. The $a_1(1260)(J^{PC} = 1^{++})$ and the $a_2(1320)(J^{PC} = 2^{++})$ can be identified immediately. A shoulder in the 1^{++} intensity at $1650\,MeV/c^2$ suggests excitation of the $a_1(1640)$. The 2^{-+} intensity shows complicated structure in the $1600\,MeV/c^2$ to $2000\,MeV/c^2$ region. The peak at $1700\,MeV/c^2$ is probably the $\pi_2(1670)$ but is likely mixed with other 2^{-+} state at higher mass [75].

Figure 4.11 shows the total intensities of the non-exotic isoscaler($I = 0$) waves, 1^{--} and 3^{--}. The peak in the 1^{--} distribution at $1700\,MeV/c^2$ is consistent with the $\omega(1650)$. Discrepancies between the solutions with different wave sets show substantial systematic errors for some mass bins. The peak in the 3^{--} intensity at $1700\,MeV/c^2$ is possibly the $\omega_3(1670)$.

The total intensities of the exotic partial waves, 1^{-+} and 2^{+-}, are shown in

[18] This is equivalently the sum of all the foreground partial waves.
[19] It is the $\Delta^{++}(1232) - \rho^-$ combination in the negative reflectivity with $m_\rho = 0$.

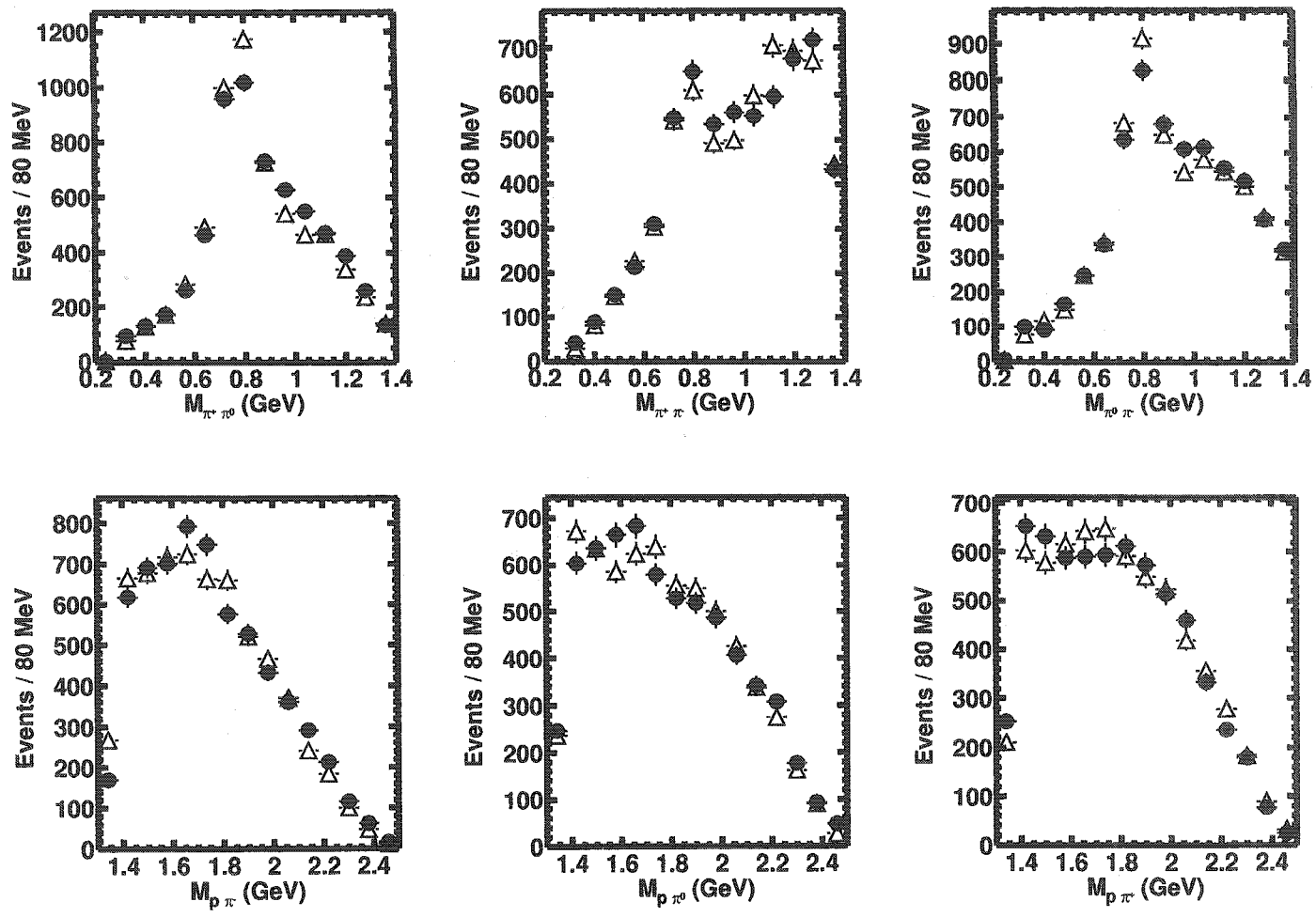

Figure 4.5: A comparison of $p\pi$ and $\pi\pi$ invariant masses between the PWA predicted events(triangle marker) and the data events(solid circle). Only statistical errors are shown in these plots.

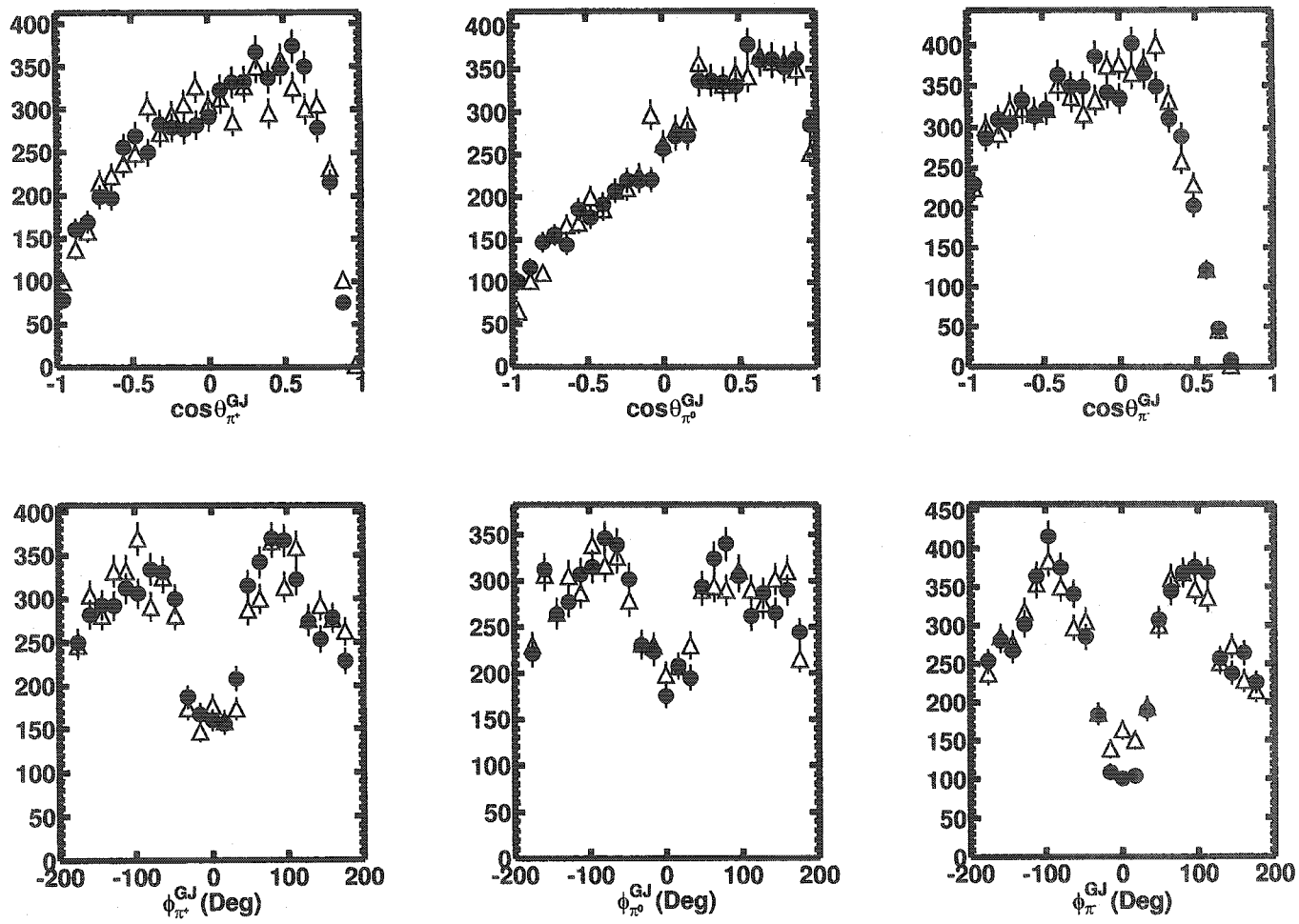

Figure 4.6: A comparison of $\cos\theta$ and ϕ of the pions in the Gottfried-Jackson frame between the PWA predicted events(triangle marker) and the data events(solid circle). Only statistical errors are shown in these plots.

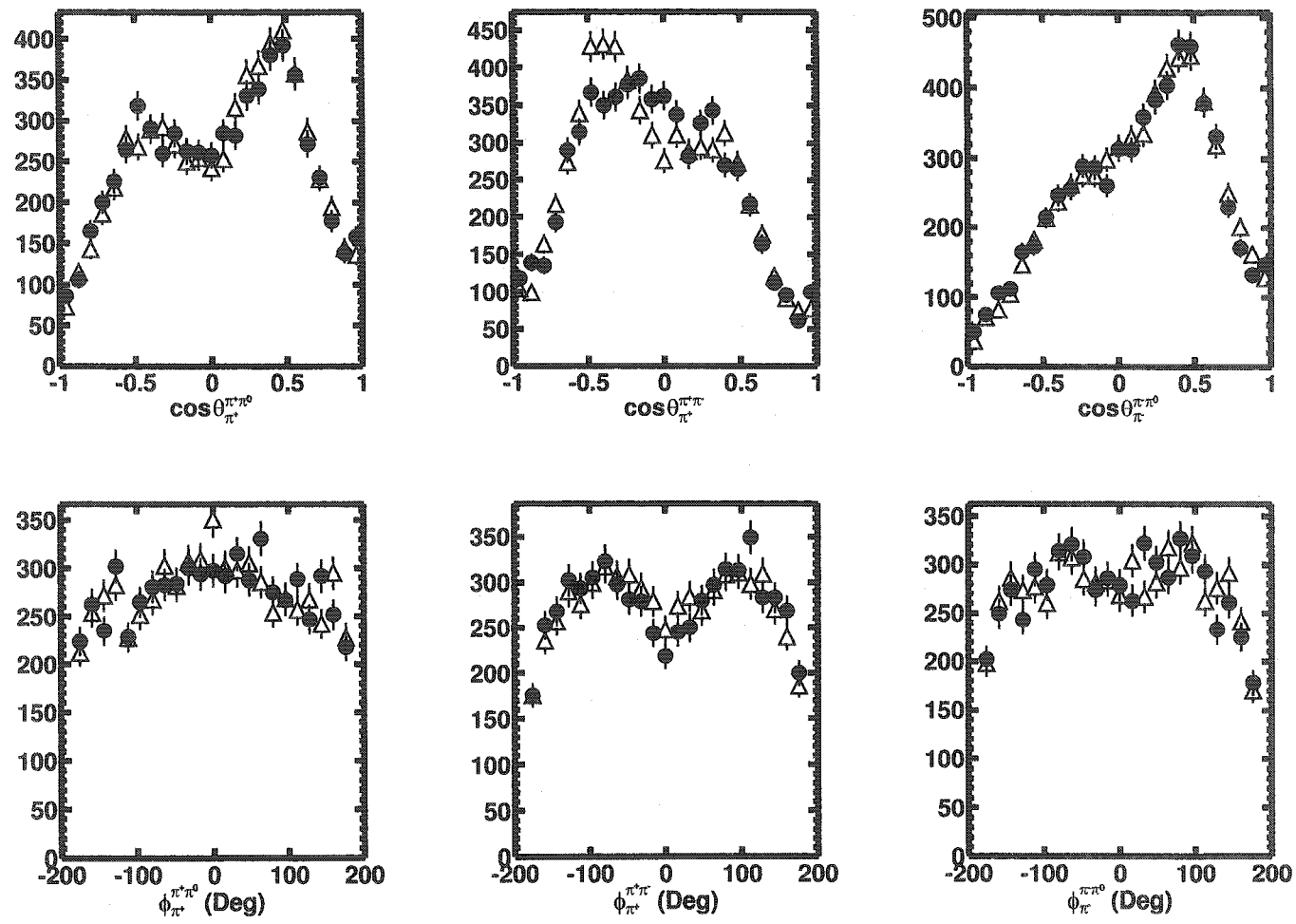

Figure 4.7: A comparison of $\cos\theta$ and ϕ of the pions in various helicity frames between the PWA predicted events(triangle marker) and the data events(solid circle). Angles are labeled as $\theta_{\pi}^{HelicityFrame}$. Only statistical errors are shown in these plots.

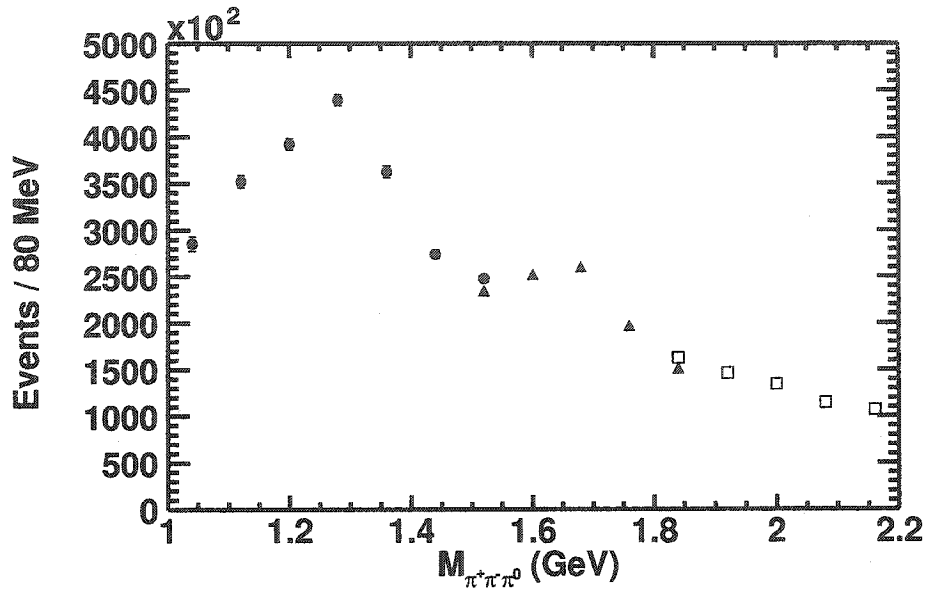

Figure 4.8: The acceptance corrected background-subtracted $\pi^+\pi^-\pi^0$ effective mass distribution. Three mass regions, as described earlier, are labeled with different markers. Two peaks at $1300\,MeV/c^2$ and $1700\,MeV/c^2$ are seen.

figure 4.12. The 1^{-+} spectrum shows a strong peak at $1700\,MeV/c^2$ near the exotic $\pi_1(1600)$ [5, 37, 65]. The 2^{+-} exotic isoscaler wave shows a peak at about $2\,GeV/c^2$.

Figure 4.13 shows the individual components of the 1^{++} partial waves contributing to the total 1^{++} intensity. Partial waves are labeled by $J^{PC}M^{\epsilon}L$. The lower lying peak at $1300\,MeV/c^2$ is dominated by the S waves and the total intensity in this mass region is roughly evenly distributed among all three S-wave partial waves. On the other hand, the higher lying peak at $1650\,MeV/c^2$ has a large contribution from the D waves, as expected from the hadroproduction data [38].

The individual 1^{--} partial waves are shown in figure 4.14. Both partial waves in the negative reflectivity show strong peaks at $1700\,MeV/c^2$. The positive reflectivity 1^{--} partial wave is relatively weaker.

Figure 4.15 shows the individual 1^{-+} exotic partial waves. Two 1^{-+} waves were used in the final PWA fit, one in each reflectivity. Both of these waves show strong peaks at $1700\,MeV/c^2$. The relative strengths of these two waves are comparable.

The discussion of the relative phases of these partial waves will be deferred to

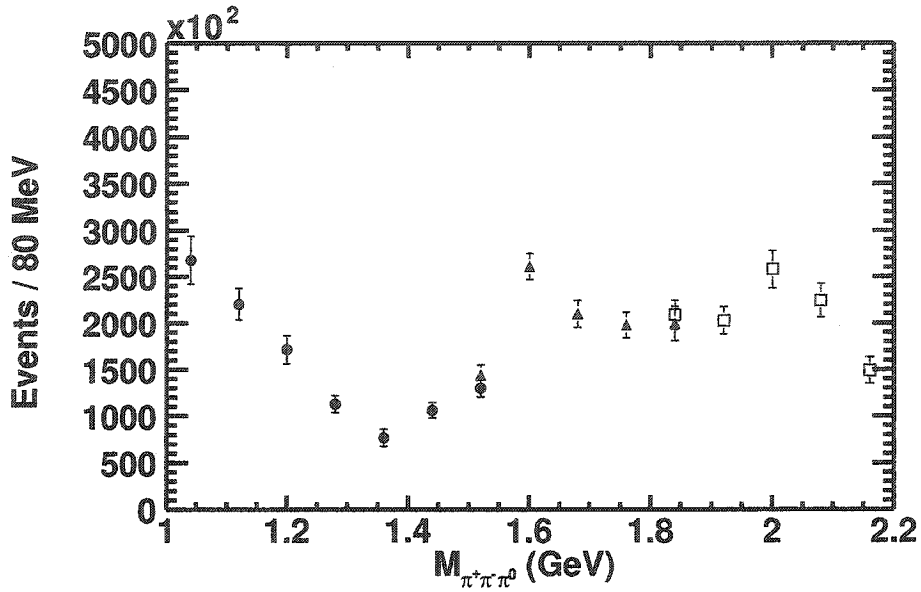

Figure 4.9: The acceptance corrected background intensity as a function of $\pi^+\pi^-\pi^0$ invariant mass. The structure at $1600\,MeV/c^2$ could possibly be attributed to the interference with the mesonic foreground waves.

the next chapter, where it will be combined with a discussion of the mass dependent analysis.

4.9 Leakage Study

To verify the exotic 1^{-+} signal, a *leakage study* on the two 1^{-+} partial waves was performed. In the leakage study, the accepted Monte Carlo events are weighted by equation (4.9) with the production amplitudes obtained from the PWA fit, just like in weighting the fit predicted data set. The difference is, in a leakage study, the production amplitude that corresponds to the partial wave which is being examined is set to zero. This set of events were then analyzed in the same manner as the data. A partial wave fit with the original wave set was performed on them. The purpose of the leakage study is to see if the strength of the partial wave under investigation was produced artificially, or *leaking* in from other partial waves and their interferences. This can occur if two partial waves in the fit have similar distributions.

Figure 4.16 shows the two 1^{-+} partial wave intensities from the leakage study. The intensities of both waves are very small compared with those shown in figure 4.15. This confirms that the signals seen in figure 4.15 are real.

A leakage study on the exotic 2^{+-} wave was also performed. The result is shown in figure 4.17. The leakage intensity makes a peak at around 1900 MeV/c^2. However, compared with the signal seen in figure 4.12, the leakage intensity is small.

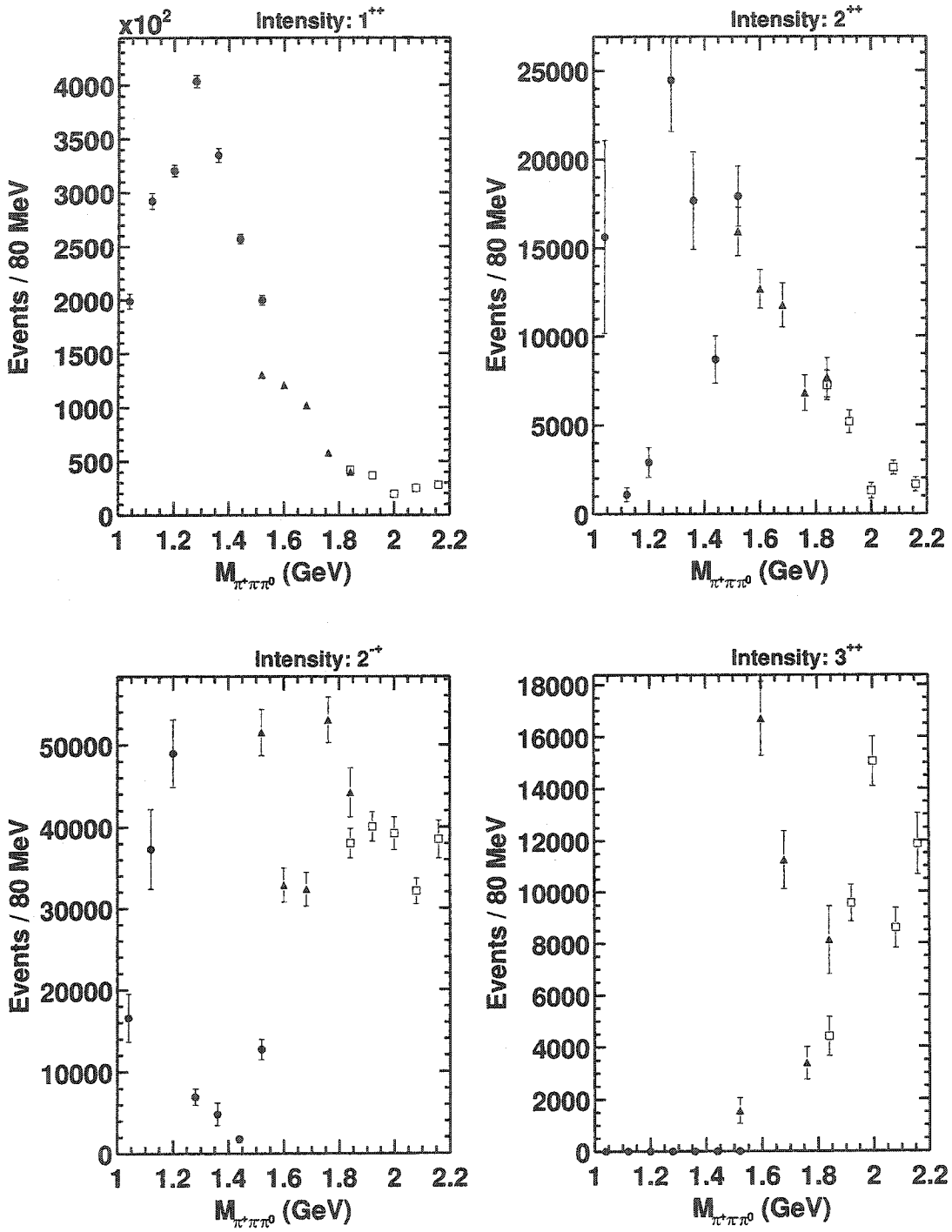

Figure 4.10: Total intensities of the non-exotic isovector parital waves. The $a_1(1260)1^{++}$ and the $a_2(1320)2^{++}$ are clearly identified. The shoulder in the 1^{++} at $1650\,MeV/c^2$ suggests production of the $a_1(1640)$. The 2^{-+} spectrum is more complicated. A peak at $1700\,MeV/c^2$ could be identified as the $\pi_2(1670)$, but possibly mixed with higher lying 2^{-+} state.

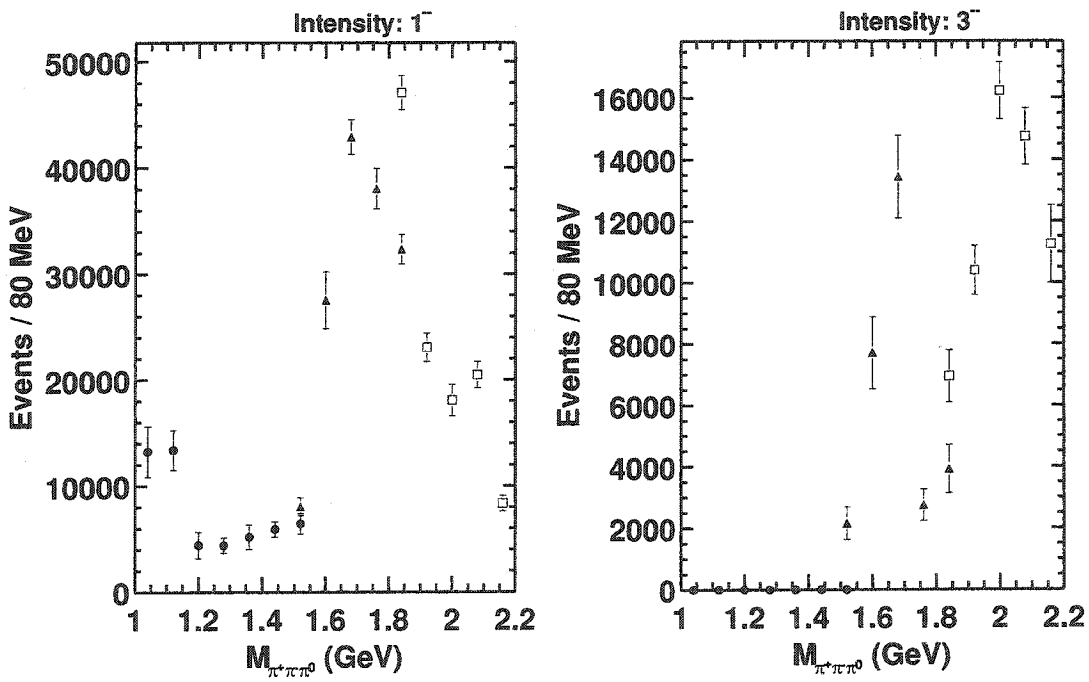

Figure 4.11: Total intensities of the non-exotic isoscaler partial waves. The peak at $1700\,MeV/c^2$ in the 1^{--} spectrum is consistent with the $\omega(1650)$. In the 3^{--} spectrum, a narrow peak at $1700\,MeV/c^2$ is possibly the $\omega_3(1670)$.

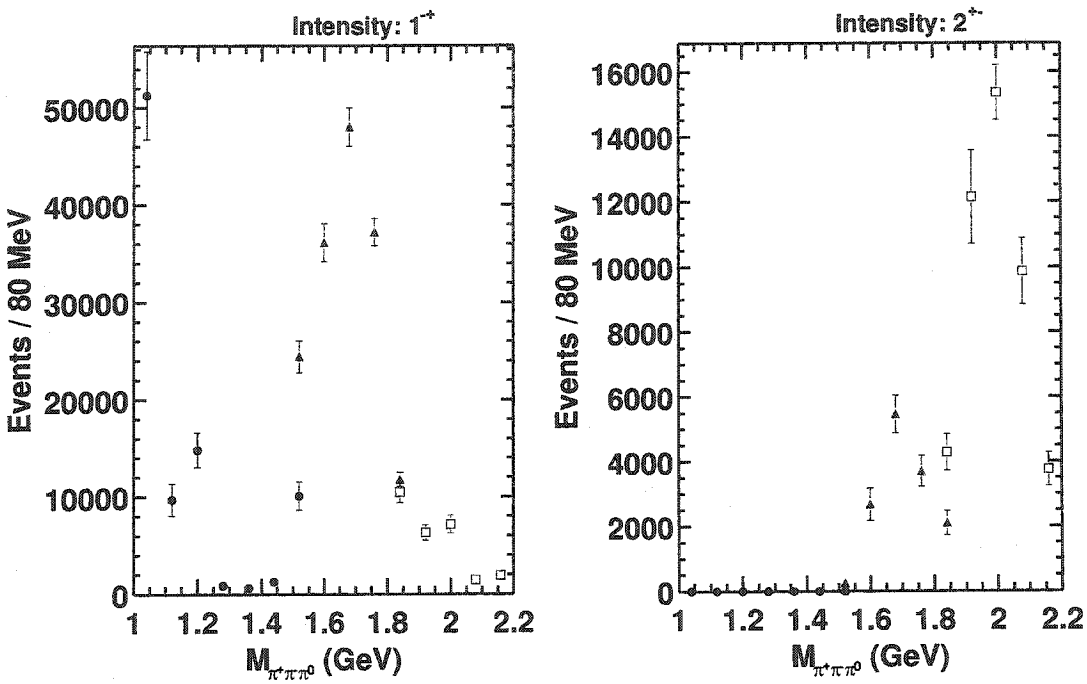

Figure 4.12: Total intensities of the exotic partial waves. The 1^{-+} spectrum shows a strong peak at $1700\,MeV/c^2$ with a $250\,MeV/c^2$ width, consistent with previous measurement of the $\pi_1(1600)$ state. The 2^{+-} exotic isoscaler spectrum shows an interesting peak at about $2\,GeV/c^2$.

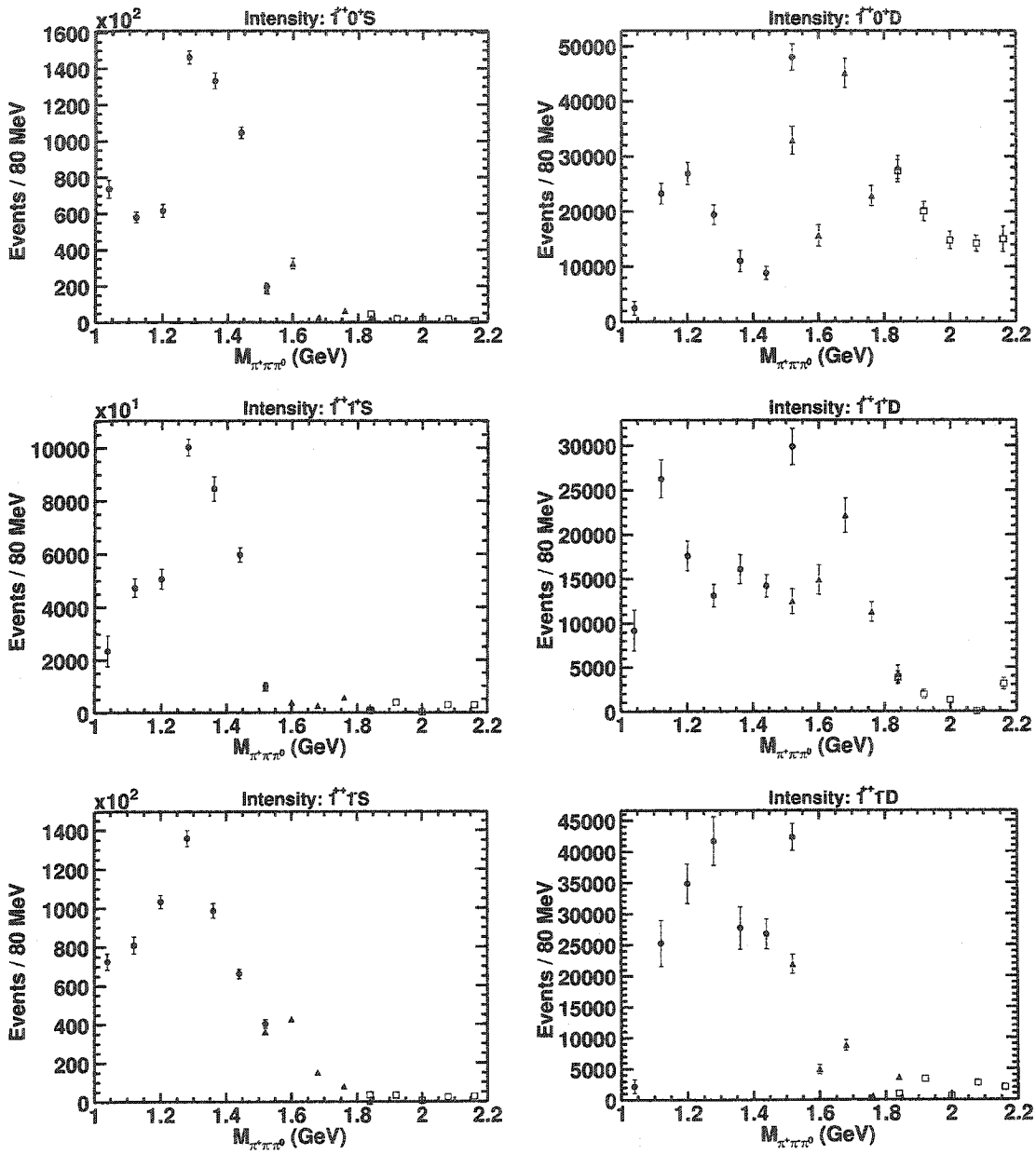

Figure 4.13: Individual 1^{++} partial waves contributing to the total intensity. Partial waves are labeled by $J^{PC}M^{\epsilon}L$. Both S and D waves were used in the fit. The lower lying peak at $1300\,MeV/c^2$ is dominated by the S waves, while a large fraction of the peak at $1650\,MeV/c^2$ comes from the D waves.

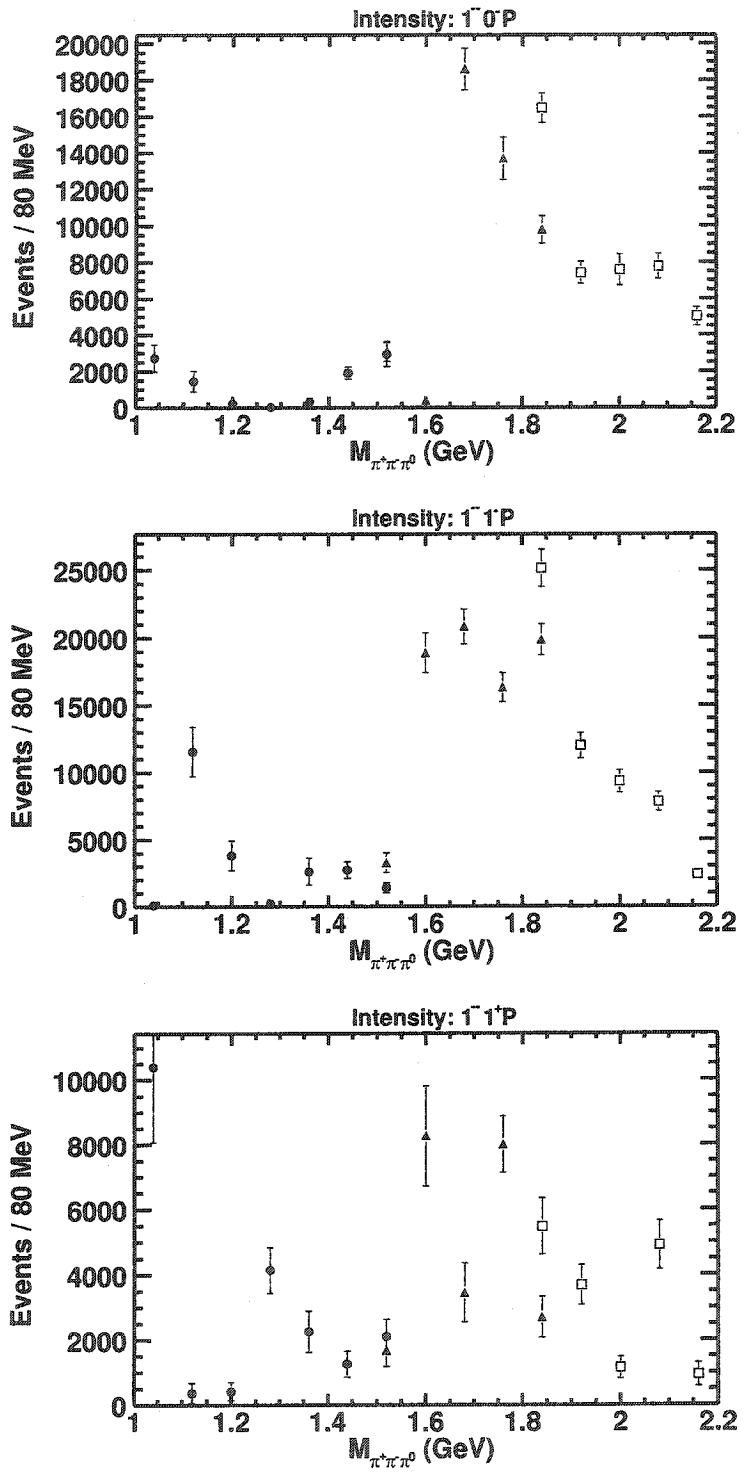

Figure 4.14: Individual 1^{--} isoscaler partial waves. Both waves in the negative reflectivity show strong peaks at $1700\,MeV/c^2$. The positive reflectivity partial wave is relatively smaller.

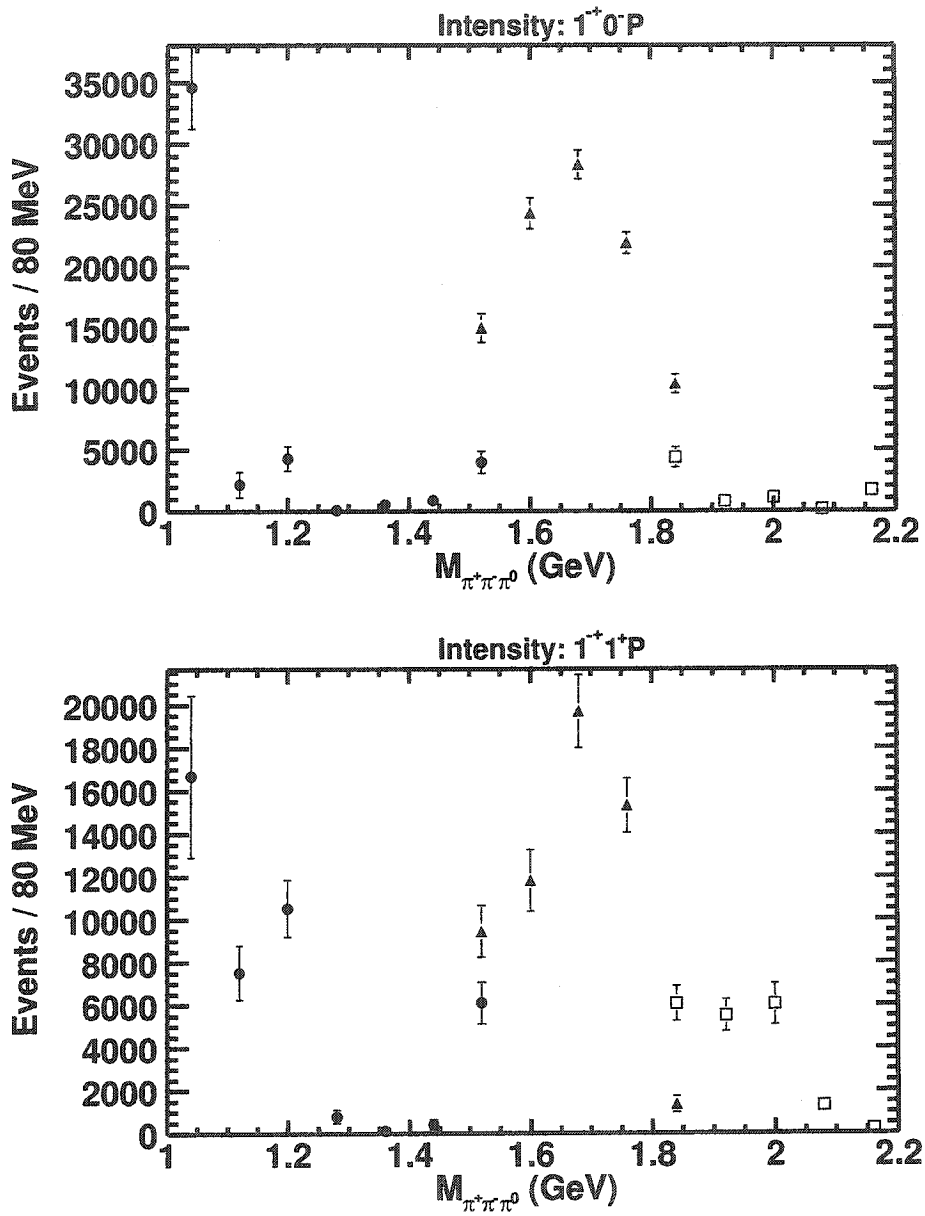

Figure 4.15: Individual 1^{-+} exotic partial waves. Two 1^{-+} waves were used in the final fit, one in each reflectivity. Both waves show peaks at $1700\,MeV/c^2$ with comparable strengths.

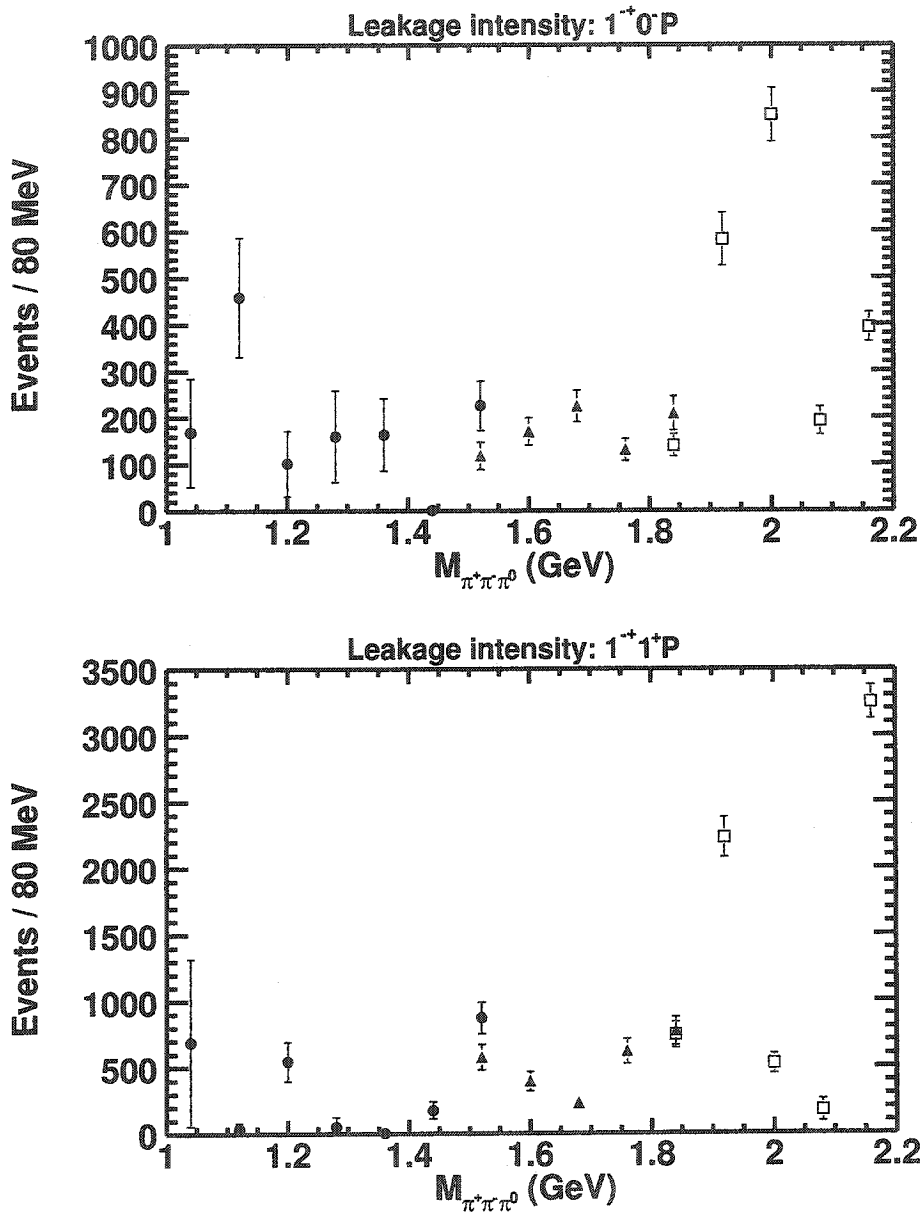

Figure 4.16: Leakage study of the 1^{-+} partial waves. The intensities of both $1^{-+}0^{-}P$ and $1^{-+}1^{+}P$ partial waves are very small compared with those shown in figure 4.15.

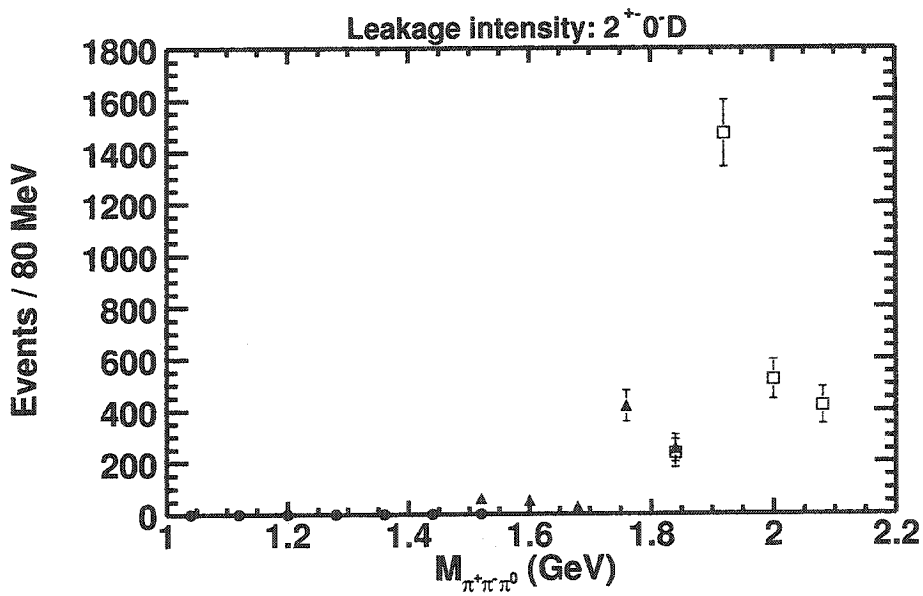

Figure 4.17: Leakage study of the 2^{+-} partial wave. The intensity is small compared with that shown in figure 4.12.

CHAPTER 5
MASS DEPENDENT ANALYSIS

In order to better understand the nature of the observed structures in the partial wave analysis results as shown in the previous chapter, a mass-dependent analysis was performed on some of the partial waves. In this chapter, a brief discussion of the mass-dependent analysis formalism is given, followed by the mass-dependent analysis result. The question of estimating the systematic errors is also addressed.

5.1 Introduction

As suggested by the name, the two-body decay amplitude of a resonance R is assumed to be a function of its mass in a mass-dependent analysis [35, 75],

$$A(W) = \sum_{\nu} N_{\nu} e^{i\phi_{\nu}} B_{\nu}(W) pq \tag{5.1}$$

where W denotes the invariant mass of the $\pi^+\pi^-\pi^0$ system, N is a normalization constant, ϕ is the production phase which is assumed to be a slowly varying function of the $\pi^+\pi^-\pi^0$ mass, and pq is the phase space factor as before. The summation runs over all the resonance poles for a given partial wave. $B(W)$ is the relativistic Breit-Wigner function given by [82, 55, 66]

$$B(W) = \frac{W_0\Gamma_0}{W_0^2 - W^2 - iW_0\Gamma_{\nu}(W)} \tag{5.2}$$

with

$$\Gamma_{\nu}(W) = \Gamma_0 \frac{k}{k_0} \frac{F_l^2(k)}{F_l^2(k_0)} \tag{5.3}$$

where W_0 and Γ_0 are the pole mass and width(FWHM) of a resonance, respectively. $F_l(k)$ is the Blatt-Weisskopf angular momentum barrier factor [63, 55]. k is the breakup momentum in the resonance rest frame, and k_0 is this breakup momentum at W_0.

The mass-dependent phase shift is then given by

$$\cot\delta(W) = \frac{k_0}{k}\frac{F_l^2(k_0)}{F_l^2(k)}\frac{W_0^2 - W^2}{W_0\Gamma_0} \tag{5.4}$$

and the overall phase for a given partial wave is

$$\Phi = \phi + \delta(W) \tag{5.5}$$

where ϕ is the production phase in equation (5.1). The phase difference between two partial waves is

$$\Delta(\Phi_{12}) = arg(A_1 \times A_2^*). \tag{5.6}$$

A least-square(χ^2) fit was used for the mass-dependent analysis with the χ^2 constructed out of the mass-independent PWA intensities and phase differences. The minimization program used is the CERNLIB routine MINUIT running in interactive mode [97].

5.2 Estimate of Systematic Errors

The error bars on the intensity distributions shown in the last chapter only included errors from the maximum likelihood fit. We will call these errors the *statistical errors* even though they actually reflect the shape of the maximum in the likelihood space. These statistical errors are defined and incorporated in the PWA in a mathematically rigorous manner.

On the other hand, due to the limitation of our model(for instance, the rank-1 spin-density matrix assumption made in section 4.5) and truncation of the basis in the partial wave analysis, *systematic errors* do exist and should be accounted for. Recalling the intensity plots in section 4.8.3, there are discrepancies between the solutions with different wave sets in some mass bins. In some cases, these discrepancies are quite large(for instance, in the $J^{PC} = 1^{--}$ intensity distribution in figure 4.11). This indicates that one major source of the systematic errors is the choice of partial waves in the PWA fit. In a maximum likelihood fit, there is no

quantitative way of determining which wave set is the best set [20]. Therefore, it is a common practice to settle on the smallest wave set that can describe the data even though other wave sets with a few more partial waves can describe the data as well. The systematic errors hence arise with truncation of the basis. Based on our PWA results, we can see that these systematic errors are strongly mass dependent.

Nevertheless, this also suggests a way to estimate the systematic errors. Once the final wave set(we shall call this wave set the *base set*) was deemed satisfactory, small partial waves that had been rejected previously in reaching the base set were added back in sequentially. Each time a partial wave was added, a partial wave fit was performed. For a given partial wave in a particular mass bin, this process gives a set of different results. These results were then used to calculate a variance,

$$\sigma_{sys}^2 = \bar{I}^2 - (\bar{I})^2 \tag{5.7}$$

where I represents the intensity of a partial wave in a given mass bin. The same procedure was followed to calculate the systematic errors on the phase differences between partial waves. Combined errors were formed by adding this variance and the statistical errors, σ_{sta}, in quadrature

$$\sigma^2 = \sigma_{sta}^2 + \sigma_{sys}^2. \tag{5.8}$$

A total of nine wave sets were tested, including the base set itself, for constructing the systematic errors. Each wave set had one more partial wave, either foreground wave or background wave, than its preceding wave set. The process stopped when there were too many waves and the statistical errors dramatically increased. Figure 5.1 shows the $J^{PC} = 1^{--}$ intensity distribution with the new error bars.

[20] In principle, the best wave set is the one composed of infinite number of basis states. However, with finite statistics this complete set is inaccessible.

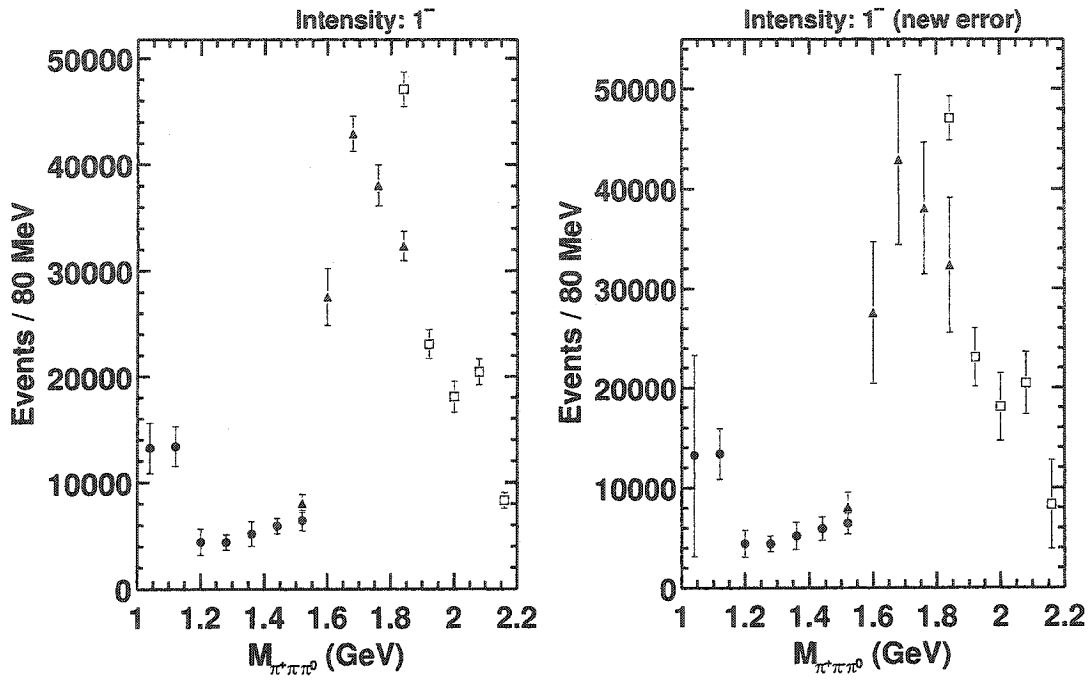

Figure 5.1: Total intensity of the $J^{PC} = 1^{--}$ waves. On the left is the intensity distribution with only the statistical errors. On the right is the intensity distribution with the new error bars constructed according to equation (5.7).

5.3 Mass Dependent Analysis Result

To further verify the exotic $J^{PC} = 1^{-+}$ signals and to extract the corresponding resonance parameters, a mass dependent analysis was performed on those partial waves. To facilitate the fit, some other non-exotic partial waves as well as the phase differences between them were also used. Table 5.1 lists the quantities that were included in the mass dependent fit. Highly correlated waves were chosen for the phase difference, as these exhibit the smallest error bars.

Only a fraction of the data points in each partial wave from the PWA fit were used in the mass dependent fit. In the overlapping mass bins [21], solutions corresponding to the middle mass region(plotted with triangle markers in the intensity

[21] As discussed in section 4.4, the full $\pi^+\pi^-\pi^0$ mass range was divided into three regions. Each region overlaps with its adjacent region by one mass bin. Thus, there are two overlapping mass bins centered at $1520\,MeV/c^2$ and $1840\,MeV/c^2$ respectively. Each mass region was fitted with different partial wave set.

$Intensity : 1^{-+}0^{-}P$
$Intensity : 1^{-+}1^{+}P$
$Intensity : 1^{++}1^{-}S$
$Intensity : 1^{++}1^{+}D$
$Intensity : 1^{--}1^{-}P$
$Phase : 1^{-+}0^{-}P - 1^{++}1^{-}S$
$Phase : 1^{++}1^{-}S - 1^{--}1^{-}P$

Table 5.1: Entries of the mass dependent fit. Partial waves are labeled by $J^{PC}M^{\epsilon}L$.

plots of section 4.8.3.) were chosen. This is also true for the other partial waves. This choice of solutions in the overlapping bins ensures the use of one set of PWA parameters in the middle mass region where both the 1^{-+} and the 1^{--} intensities peak.

However, choosing one solution over the other in the overlapping bins also introduces another kind of systematic error. To accommodate this, four [22] mass-dependent fits were performed which gave four sets of answers for the resonance parameters. This allows us to calculate the deviations between these answers which are associated with difference choices of PWA solutions in the overlapping mass bins. The errors calculated in this way are quoted as the systematic errors in presenting the resonance paramters.

Eight points were used for each of the two 1^{++} intensities, which extend from $1200\,MeV/c^2$ to $1800\,MeV/c^2$ in $\pi^+\pi^-\pi^0$ mass. For the two 1^{-+} partial waves, five points were used for each intensity. Four points were used for the 1^{--} intensity as well as for the two phase differences. This gives us a sample of 38 data points for the mass dependent fit.

For the 1^{-+} waves and the 1^{--} wave, one resonance pole was postulated, while for the 1^{++} waves two poles were used. This results in a total of seven poles in all the partial waves. Recalling equation (5.1), each resonance pole requires four independent parameters in the fit, including a constant production phase for each pole. Therefore it is a fit with twenty-eight free parameters on very limited number(38) of data points. To enlarge the number of degrees of freedom, some of the resonance

[22]Since we have two overlapping mass bins, there are four ways of picking solutions.

parameters were constrained in the fit. Specifically, the two 1^{-+} poles share the same pole mass and resonance width, and so do the four 1^{++} poles. Constraining parameters in this way reduces the total number of independent parameters to twenty-one [23], and the number of degrees of freedom(DOF) for this fit becomes seventeen.

The results of the mass dependent analysis are shown in figure 5.2 and figure 5.3. The mass of the exotic 1^{-+} state from our fit is $1690 \pm 5 \pm 7\, MeV/c^2$. It is higher than that previously measured in the $\eta'\pi^-$ channel($1597^{+45}_{-10}\, MeV/c^2$) [65], and in the $\rho(770)\pi^-$ channel($1593 \pm 8^{+29}_{-47}\, MeV/c^2$) [38], and is slightly higher than the mass obtained in the $b_1\pi$ channel($1664 \pm 8\, MeV/c^2$) [75]. This value is consistent with the result from the $f_1(1285)\pi^-$ channel($1709 \pm 24 \pm 41\, MeV/c^2$) [71]. The width of the 1^{-+} state from our fit is $\Gamma = 268 \pm 14 \pm 42\, MeV/c^2$, falling within a wide range of previously measured widths.

The 1^{++} waves were fitted with two resonance poles. The lower lying pole has a mass of $1278 \pm 6 \pm 6\, MeV/c^2$ and a width of $227 \pm 9 \pm 6\, MeV/c^2$. This mass is slightly higher than the PDG average of $1230 \pm 40\, MeV/c^2$ for the $a_1(1260)$ state [60], while the width is narrower than most of the measurements listed in the PDG particle table. The higher lying pole has a mass of $1704 \pm 9 \pm 24\, MeV/c^2$ and a width of $322 \pm 28 \pm 15\, MeV/c^2$, which are consistent with a previously observed $a_1(1640)$ state with a mass of $1714 \pm 9 \pm 36\, MeV/c^2$ and a width of $308 \pm 37 \pm 62\, MeV/c^2$ [38]. But its mass is higher than the previously measured value of $1640 \pm 12 \pm 30\, MeV/c^2$ [18].

The 1^{--} isoscaler state shows a mass of $1727 \pm 9 \pm 2\, MeV/c^2$ and a width of $167 \pm 23 \pm 26\, MeV/c^2$. This mass is substantially higher than the PDG average of $1649 \pm 24\, MeV/c^2$ for the $\omega(1650)$ state [60]. However, it agrees with the newest measurements of $1700 \pm 20\, MeV/c^2$ in the $\omega\eta$ channel [56] and $1705 \pm 26\, MeV/c^2$ in the $\omega\pi^+\pi^-$ channel [9]. The width is narrower than the PDG average of $220 \pm 35\, MeV/c^2$. The mass dependent fit results are tabulated in table 5.2.

The number of degrees of freedom(NDF) for this fit is 17. The χ^2 per degree of freedom is 1.72, corresponding to a 5% confidence level. The relatively low confidence level suggests that the errors used in the mass dependent fit are probably

[23] Because the absolute phase is unmeasurable, one production phase was set to zero in the fit.

$I^G J^{PC}$	$Mass\,(MeV/c^2)$	$Width\,(MeV/c^2)$	$Yield$
1^-1^{-+}	$1690 \pm 5 \pm 7$	$268 \pm 14 \pm 42$	219677 ± 3198
1^-1^{++}	$1278 \pm 6 \pm 6$	$227 \pm 9 \pm 6$	610564 ± 7008
	$1704 \pm 9 \pm 24$	$322 \pm 28 \pm 15$	158351 ± 3358
0^-1^{--}	$1727 \pm 9 \pm 2$	$167 \pm 23 \pm 26$	67904 ± 2699
0^-2^{+-}	$2021 \pm 17 \pm 6$	$184 \pm 25 \pm 26$	51842 ± 1014

Table 5.2: List of resonance parameters obtained from the mass dependent analysis. Errors quoted are the statistical errors and systematic errors respectively. Yield is the acceptance corrected number of events integrated from the $\rho\pi$ threshold to the maximum mass allowed by phase space.

underestimated. This is not surprising since there are contributions from the PWA model dependence that cannot be estimated.

For the other exotic wave, $J^{PC}M^{\epsilon}L = 2^{+-}0^-D$, a mass dependent fit on the intensity was carried out. No phase difference was used in this fit due to the lack of other strong partial waves in this mass region. The result is shown in figure 5.4. It reveals a narrow peak at about $2\,GeV/c^2$. The mass and width are [24] $M = 2021 \pm 17 \pm 6\,MeV/c^2$ and $\Gamma = 184 \pm 25 \pm 26\,MeV/c^2$, respectively. The χ^2 of this fit is 0.56. For a fit of two degrees of freedom, this χ^2 corresponds to a confidence level of 70%.

[24] Since there are only two possible choices of solutions in the overlapping bin in this case, the systematic errors quoted here are the average of the deviations between these two solutions.

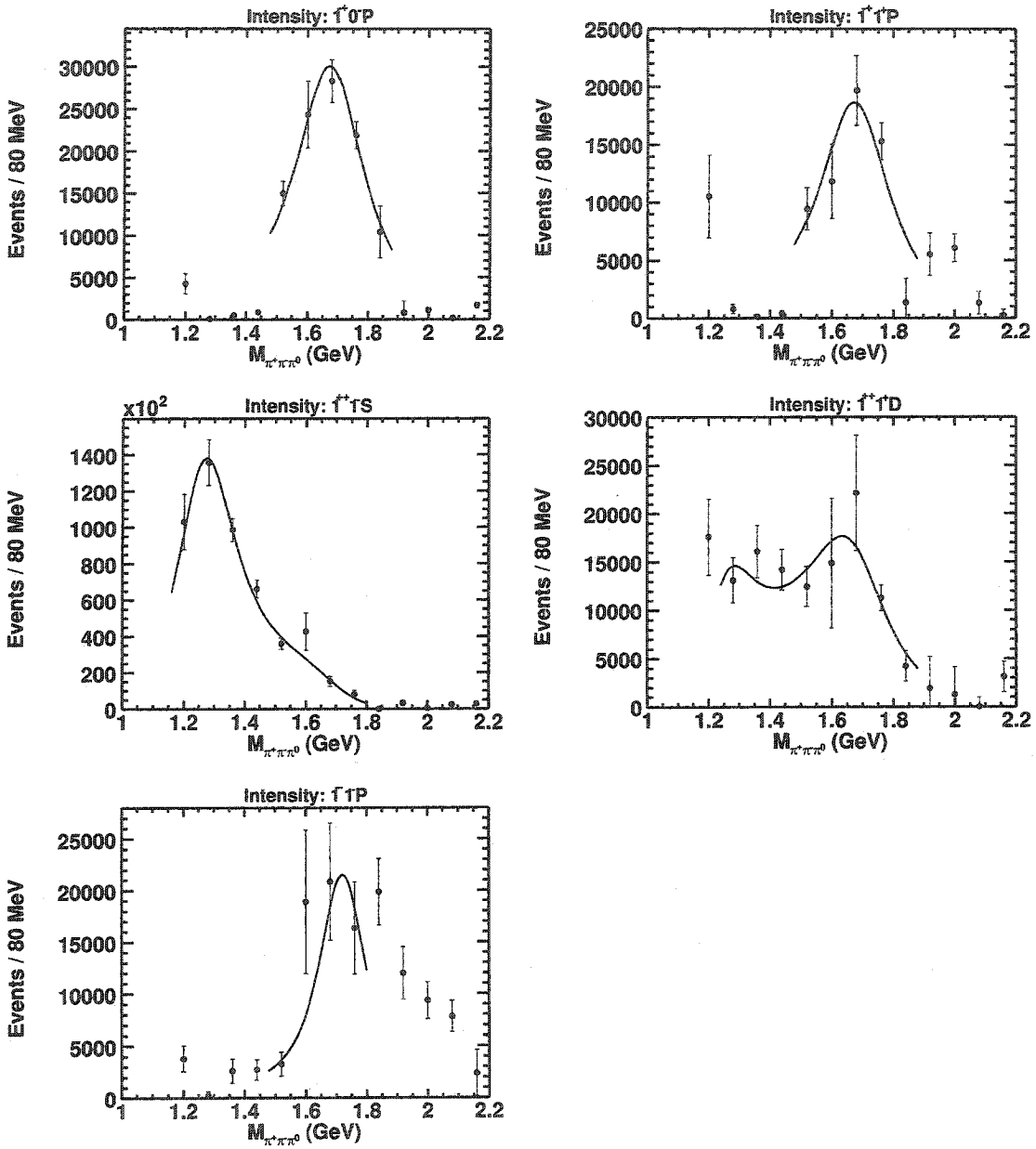

Figure 5.2: Mass dependent fit results on the intensity distributions. The error bars on the data points are described in the text. Partial waves are labeled by $J^{PC}M^{\epsilon}L$.

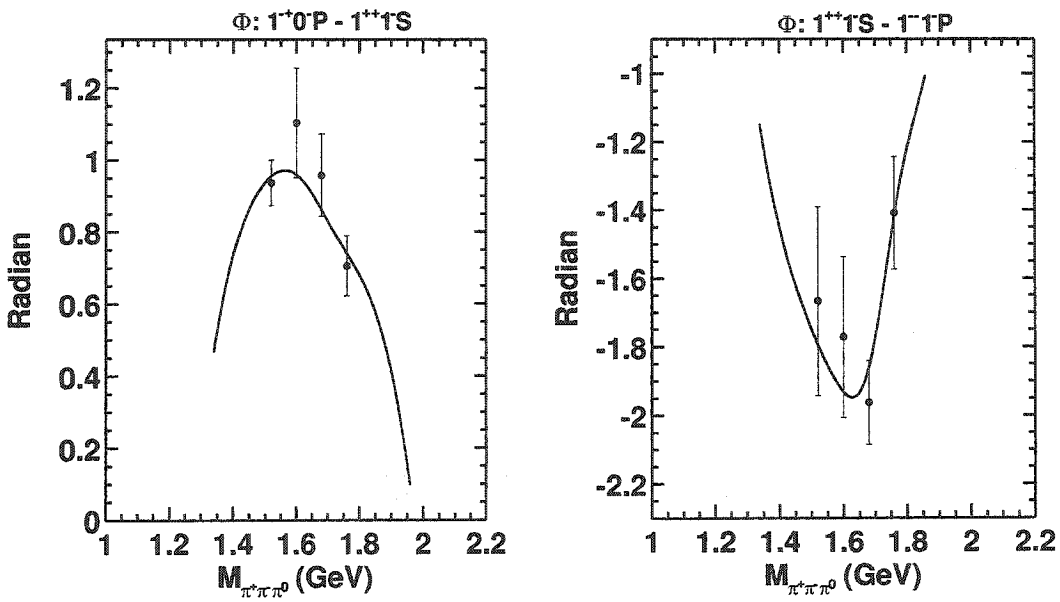

Figure 5.3: Mass dependent fit results on the phase differences. The error bars on the data points are described in the text. Partial waves are labeled by $J^{PC}M^{\epsilon}L$.

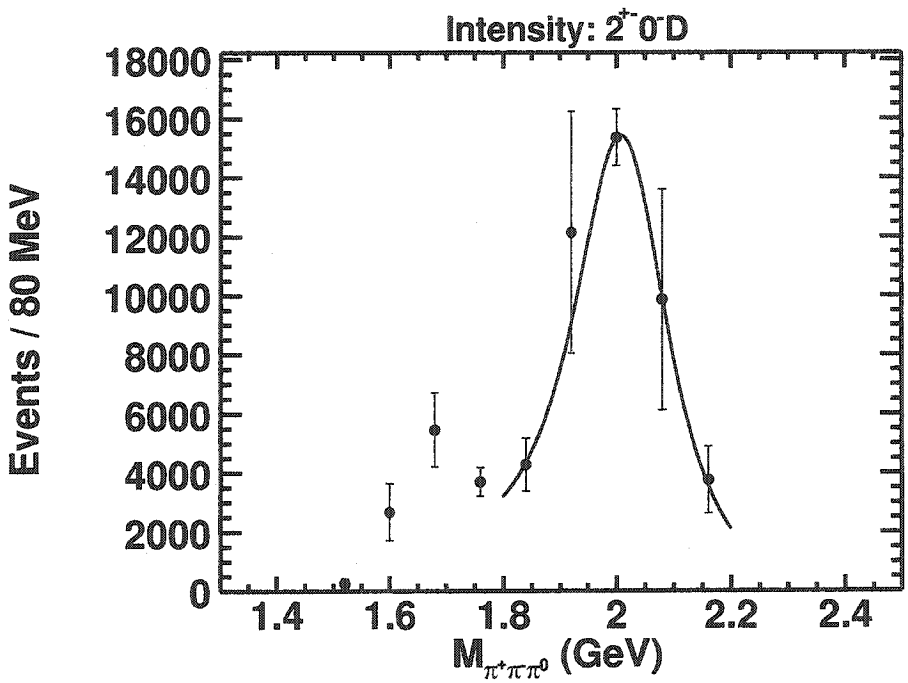

Figure 5.4: Mass dependent fit result on the 2^{+-} intensity. The error bars on the data points are described in the text.

CHAPTER 6
DISCUSSION AND CONCLUSIONS

A partial wave analysis was performed on a sample of $140K$ $\pi^+\pi^-\pi^0$ events from the reaction

$$\gamma p \rightarrow p\pi^+\pi^-\pi^0 \tag{6.1}$$

with beam photon energy in the range $[4.8, 5.5]\,GeV$. The primary goal of this analysis was to confirm the photo-excitation of the $J^{PC} = 1^{-+}$ exotic meson resonance in the $1 - 2\,GeV/c^2$ region in $\pi^+\pi^-\pi^0$ mass. This set of data also provided a good opportunity to study other mesonic states in this mass range by meanings of partial wave analysis.

The PWA fit revealed a rather complicated meson spectroscopy, as shown in chapter 4. The 1^{++} $a_1(1260)$ dominates the low mass region(see figure 4.10). There is good reason [41, 43] to believe that in photoproduction the *Deck effect* [49] for producing the $a_1(1260)$ is greatly suppressed. Therefore, the 1^{++} signal seen here is very likely to be the true $a_1(1260)$.

In an earlier photon beam experiment [43], the reaction $\gamma p \rightarrow \Delta\rho\pi \rightarrow 2\pi^+2\pi^-p$ was studied and no evidence for charge-exchange photoproduction of the $a_1(1260)$ was found. Our reaction channel differs greatly from that channel in the exchange mechanism. In our channel, the exchange particle has to be neutral and single π^0 exchange is excluded for the most part [25]. The exchange particle is likely to be ω or ρ, with ω-exchange being dominant [17, 52]. Therefore, it is tempting to speculate that the discrepancy in the $a_1(1260)$ signals from these two experiments may be attributed to the exchange mechanism.

There is large discrepancy in the measured mass and width of the $a_1(1260)$

[25] In our study, the one-pion-exchange(OPE) model may not hold for the following reason: if vector-dominance-model(VDM) is assumed, the incident photon couples electromagnetically to an ρ^0 meson which is an isovector in its neutral state. The resulting system under study, $\pi^+\pi^-\pi^0$, is necessarily a G-parity eigenstate. Therefore its isospin is fixed by its J^C combination, cf. equations 1.10. Since charge and isospin are conserved quantities in strong interaction, the exchange particle can not be isovector, for instance a π^0, for producing a neutral isovector final state. Mathematically, $|10\rangle = 0 \times (|10\rangle + |10\rangle)$, where $|10\rangle$ denotes $|I = 1, I_3 = 0\rangle$.

from previous experiments. The PDG averaged $1230 \pm 40\, MeV/c^2$ for its mass and $250 - 600\, MeV/c^2$ for its width. Our mass dependent analysis showed a mass of $1278 \pm 6 \pm 6\, MeV/c^2$ and a width of $227 \pm 9 \pm 6\, MeV/c^2$ for this state. The mass agrees with the PDG averaged value within errors, and the width is narrower than most of the measurements listed in the PDG particle table. No previous photoproduction experiments measured the properties of $a_1(1260)$.

At around $1700\, MeV/c^2$, a shoulder was seen in the 1^{++} wave. This is possibly the radial excitation of the $a_1(1260)$ — the $a_1(1640)$ [25]. An earlier experiment at BNL [73] observed a prominent 1^{++} state at $1.7\, GeV/c^2$ in the $f_1(1285)\pi$ channel with a width of $\sim 400\, MeV/c^2$. The VES group [11] also found a strong isovector 1^{++} state at $M \approx 1700\, MeV/c^2$ in the $\rho\pi$ D-wave, but did not find well defined signals in the $\rho\pi$ S-wave nor in the $\sigma\pi$ P-wave. More recently, a study [18] of the reaction $\bar{p}p \to 4\pi^0$ revealed a $J^{PC} = 1^{++}$ resonance with a mass of $1640 \pm 12 \pm 30\, MeV/c^2$ and a width of $300 \pm 22 \pm 40\, MeV/c^2$. These values are quoted by the PDG particle table for the $a_1(1640)$ resonance. The preferred decay modes of the $a_1(1640)$ from that analysis were $\sigma\pi$ P-wave and $f_2(1270)\pi$ P-wave.

The latest report on the $a_1(1640)$ state was from experiment E852 at BNL [38]. In that study, a partial wave analysis was performed on the $\pi^+\pi^-\pi^-$ system and a 1^{++} peak at around $1700\, MeV/c^2$ in the $\rho\pi$ D-wave was observed. Their fit results for the mass and width of the $a_1(1640)$ state were $1714 \pm 9 \pm 36\, MeV/c^2$ and $308 \pm 37 \pm 62\, MeV/c^2$. The present data also show strong D-wave decay of the $a_1(1640)$. Our mass dependent analysis gave a mass of $1704 \pm 9 \pm 24\, MeV/c^2$ and a width of $322 \pm 28 \pm 15\, MeV/c^2$ for this state. The mass from our fit is higher than the PDG value, but both the mass and the width are in good agreement with the BNL [38] measurement.

The 2^{++} waves showed a narrow peak around $1300\, MeV/c^2$, which is consistent with excitation of the $a_2(1320)$. However, because of the lack of phase information and our relatively large bin size($80\, MeV/c^2$), we could not extract the resonance parameters from this signal.

The strength found in the isoscaler 1^{--} waves suggests excitation of the $\omega(1650)$ state. The $\omega(1650)$ is a well known state. The PDG average for its mass

and width are $1649 \pm 24\, MeV/c^2$ and $220 \pm 35\, MeV/c^2$ respectively. Our mass dependent fit gave a mass of $1727 \pm 9 \pm 2\, MeV/c^2$ and a width of $167 \pm 23 \pm 26\, MeV/c^2$ for the 1^{--} state. This mass is substantially higher than the PDG average.

However, the flux-tube model predicts an isoscaler hybrid 1^{--} at about the same mass as the 1^{-+} hybrid [81]. Thus hybrid excitation could contribute to the 1^{--} in this mass region. There was one previous observation of a narrow $J^{PC} = 1^{--}$ state [13] with $M = 1870 \pm 10\, MeV/c^2$ and $\Gamma = 10 \pm 5\, MeV/c^2$. Though isospin and G-parity of that state could not be determined in their study. Looking back at figure 4.11, there was large discrepancy in the 1^{--} intensity distribution in one mass bin above $1800\, MeV/c^2$. A mass dependent fit with two resonance poles for the 1^{--} wave was tried in attempt to accommodate a second state above $1800\, MeV/c^2$. But the phase data do not support such a fit. Nevertheless, it is possible that what we see here is a mixture of the conventional $\omega(1650)$ state and a higher lying hybrid 1^{--} state. Most recent measurements [56, 9] also showed a higher mass for $\omega(1650)$ than the PDG average.

The exotic 1^{-+} partial waves showed a strong peak at $1700\, MeV/c^2$. Its intensity is about 10% of the total intensity in that mass region. The excitation of the $\pi_1(1600)$ is confirmed by a mass-dependent fit which gave a mass of $1690 \pm 5 \pm 7\, MeV/c^2$ and a width of $268 \pm 14 \pm 42\, MeV/c^2$ for this 1^{-+} state. This mass is consistent with the previously measured value of $1709 \pm 24 \pm 41\, MeV/c^2$ for the $\pi_1(1600)$ in the $f_1(1285)\pi$ channel [71], but higher than those measured in $\eta'\pi^-$ channel($1597^{+45}_{-10}\, MeV/c^2$) [65], $\rho(770)\pi^-$ channel($1593 \pm 8^{+29}_{-47}\, MeV/c^2$) [38] and $b_1\pi$ channel($1664 \pm 8\, MeV/c^2$) [75].

There were theoretical predictions that the J^{PC} exotics should be produced copiously in photoproduction [7, 8]. However, those calculations were based on a single-pion-exchange(OPE) assumption. As discussed earlier in this chapter, the OPE model probably does not hold in our reaction channel. Therefore the production mechanism for the photoproduction of exotic mesons should be more carefully examined on the theory side.

The present data provide the first evidence for strong photoproduction of an exotic meson. Narrow peaks were observed in the three-pion system in an earlier

photon beam experiment [42]. Their results on the mass and width of those peaks were $M = 1763 \pm 20$, $\Gamma = 192 \pm 60\, MeV/c^2$ in the $\gamma p \to \Delta^{++}\pi^+\pi^-\pi^-$ channel and $M = 1787 \pm 18\, MeV/c^2$, $\Gamma = 118 \pm 60\, MeV/c^2$ in the $\gamma p \to n\pi^+\pi^-\pi^-$ channel. An amplitude analysis on those data yielded inconclusive results [26]. There has been speculation that what they observed were exotic signals. The mass for the 1^{-+} state from our analysis is significantly lower than their values, which suggests the possibility that the signals observed in that experiment were not the 1^{-+} exotic.

In addition to the $J^{PC} = 1^{-+}$ exotic state, we also observed a narrow peak at about $2\, GeV/c^2$ in the exotic isoscaler 2^{+-} wave. A mass dependent fit to its intensity was performed and gave a mass of $2021 \pm 17 \pm 6\, MeV/c^2$ and a width of $184 \pm 25 \pm 26\, MeV/c^2$ for this state. This is the first observation of a $J^{PC} = 2^{+-}$ exotic isoscaler state. However, due to lack of other strong signals in this mass region, no phase information could be used in the mass dependent fit. Therefore, the resonant nature of the 2^{+-} signal could not be established.

Assuming this 2^{+-} signal is real, an interesting observation can then be made. The mass splitting between hybrid mesons due to orbital-spin interactions were calculated by Merlin and Paton [78]. Their calculation showed that the isoscaler hybrid 2^{+-} should have a lower mass than the isovector hybrid 1^{-+}, and the mass splitting between these two is small($\sim 150\, MeV/c^2$). This is contrary to the results from our mass dependent analysis, which showed a $\sim 300\, MeV/c^2$ difference in mass between these two states with the 1^{-+} lying lower than the 2^{+-}. This contradiction is suggestive that the 1^{-+} and the 2^{+-} can not both be hybrids.

More thorough study can be done with larger statistics and better mass resolution. Higher beam energy can also benefit this kind of study in at least two respects. Firstly, higher beam energy will further separate the baryon channels from the meson channels in phase space and make the baryon background easier to deal with. Secondly, higher beam energy gives larger phase space which will allow us to access more states at the high end of the $\pi^+\pi^-\pi^0$ mass spectrum.

To conclude, we have for the first time successfully applied a full partial wave analysis on the three-pion photoproduction data. Our parametrization of the baryon

[26] The total angular momentum J of those states could not be determined, but other quantum number were assigned as $I^G J^{PC} = 1^-?^{-+}$.

background is probably the first attempt to incorporate the baryon channels in a partial wave analysis of this type. We have confirmed the exotic $J^{PC} = 1^{-+}$ meson and extracted its resonance parameters. The photon coupling for this state is quite large. We have also established the 1^{++} $a_1(1260)$, the 1^{++} $a_1(1640)$ and the 1^{--} $\omega(1650)$ states in photoproduction and extracted their resonance parameters. The results of this analysis will provide valuable input to our knowledge of meson spectroscopy in the $1-2\,GeV/c^2$ mass range and to a better understanding of QCD in the non-perturbative region.

BIBLIOGRAPHY

[1] K. Abe *et al.*, *Study of the $\rho'(1600)$ Mass Region Using $\gamma p \to \pi^+\pi^- p$ at $20\,GeV$*, Phys. Rev. Lett **53:751**, 1984

[2] K. Abe *et al.*, *Test of S-Channel Helicity Conservation in Inelastic ρ^0 Diffraction in $20 - GeV$ Photoproduction*, Phys. Rev. D **32:2288**, 1985

[3] A. Abele *et al.*, *Exotic $\eta\pi$ State in $\bar{p}d$ Annihilation at Rest into $\pi^-\pi^0\eta p_{spectator}$*, Phys. Lett. B **423:175**, 1998

[4] A. Abele *et al*, *Evidence for a $\pi\eta$-P-Wave in $\bar{p}p$-Annihilations at Rest into $\pi^0\pi^0\eta$*, Phys. Lett. B **446:349**, 1999

[5] G. S. Adams *et al.*, *Observation of a New J^{PC} Exotic State in the Reaction $\pi^- p \to \pi^+\pi^-\pi^- p$ at $18\,GeV/c$*, Phys. Rev. Lett. **81:5760**, 1998

[6] G. S. Adams *et al.*, *The CLAS Cerenkov Detector*, NIM A **465:414**, 2001

[7] A. Afanasev and P. R. Page, *Photoproduction and Electroproduction of $J^{PC} = 1^{-+}$ Exotics*, Phys. Rev. D **57:6771**, 1998

[8] A. Afanasev and A. Szczepaniak, *Charge Exchange $\rho^0\pi^+$ Photoproduction and Implications for Searches of Exotic Meson*, Phys. Rev. D **61:114008**, 2000

[9] P. R. Akhmetshin *et al.*, *Study of the Process $e^+e^- \to \pi^+\pi^-\pi^+\pi^-\pi^0$ with CMD-2 Detector*, Phys. Lett. B **489:125**, 2000

[10] M. Amarian *et al.*, *The CLAS Forward Electromagnetic Calorimeter*, NIM A **460:239**, 2001

[11] D. V. Amelin *et al.*, *Study of Resonance Production in Diffractive Reaction $\pi^- A \to \pi^+\pi^-\pi^- A$*, Phys. Lett. B **356:595**, 1995

[12] E. Anciant *et al.*, *Tagger Hit Reconstruction Software and Tagger Calibration Overview*, CLAS Note **99:004**, 1999

[13] A. Antonelli *et al.*, *Measurement of the Total $e^+e^- \to$ hadrons Cross Section Near the $e^+e^- \to N_{\bar{N}}$ Threshold*, Phys. Lett. B **365:427**, 1996

[14] M. Atkinson *et al*, *Photoproduction of an Isoscaler 3π Resonance at $1.67\,GeV$*, Phys. Lett. B **127:132**, 1983

[15] M. Atkinson *et al.*, *Photoproduction of $\pi^+\pi^-\pi^0$ on Hydrogen with Linearly Polarized Photons of Energy $20 - 70\,GeV$*, Nucl. Phys. B **231:15**, 1984

[16] M. Atkinson *et al.*, *A Spin-Parity Analysis of the $\omega\pi^0$ Enhancement Photoproduction in the Energy Range* 20 *to* 70 GeV, Nucl. Phys. B **243:1**, 1984

[17] I. G. Aznauryan, *On the Possibilities to Study the Exotic State* 1^{-+} *in the Experiments on Photoproduction of the* $\pi\eta$, $\pi\eta'$ *Systems*, Z. Phys. C **68:459**, 1995

[18] C. A. Baker *et al.*, *Evidence for a* $J^{PC} = 1^{++}, I = 1$ *Meson at* 1640 MeV, Phys. Lett. B **449:114**, 1999

[19] A. Baldini *et al.*, *Landolt-Börnstein: Numerical Data and Functional Relationships in Science and Technology*, New Series GG 1 Vol. 12 SVOL b, 1987

[20] G. S. Bali *et al.*, *Static Potentials and Glueball Masses From QCD Simulations with Wilson Sea Quarks*, Phys. Rev. D **62:054503**, 2000

[21] J. Ballam *et al.*, *Vector-Meson Production by Polarized Photons from 2.8. 4.7 and 9.3 GeV*, Phys. Rev. D **7:3150**, 1973

[22] F. J. Barbosa *et al.*, *A Drift Chamber System for a Toroidal Detector*, NIM A **323:191**, 1992

[23] T. Barnes *et al.*, *$Q\bar{Q}G$ Hybrid Mesons in the MIT Bag Model*, Nucl. Phys. B **224:241**, 1983

[24] T. Barnes *et al.*, *Hybrid and Conventional Mesons in the Flux Tube Model: Numerical Studies and their Phenomenological Implications*, Phys. Rev. D **52:5242**, 1995

[25] T. Barnes *et al.*, *Higher Quarkonia*, Phys. Rev. D **55:4157**, 1997

[26] T. Barnes, *Exotic Mesons, Theory and Experiment*, arxiv:hep-ph/0007296 v1, 2000

[27] M. Battaglieri *et al.*, *First Level Trigger Optimisation in Vector Meson Photoproduction*, CLAS Note **97:006**, 1997

[28] C. Bernard *et al.*, *Exotic Mesons in Quenched Lattice QCD*, Phys. Rev. D **56:7039**, 1997

[29] G. R. Blackeet *et al.*, *The Photoproduction of the $b_1(1235)\pi$ System*, hep-ex/9708032

[30] D. S. Carman *et al.*, *The Region One Drift Chamber for the CLAS Spectrometer*, NIM A **419:315**, 1998

[31] M. Chanowitz and S. Sharpe, *Hybrids: Mixed States of Quarks and Gluons*, Nucl. Phys. B **222:211**, 1983

[32] A. Chodos *et al.*, *New Extended Model of Hadrons*, Phys. Rev. D **9:3471**, 1974

[33] S. U. Chung, *Spin Formalisms*, CERN Report **71-8**, 1971

[34] S. U. Chung and T. L. Trueman, *Positivity Conditions on the Spin Density Matrix: A Simple Parametrization*, Phys. Rev. D **11:633**, 1975

[35] S. U. Chung, *Formulas for Partial-Wave Analysis, Version II*, BNL Report **BNL-QGS-93-05**, 1993

[36] S. U. Chung, *C- and G-parity: A New Definition and Applications*, BNL internal report **BNL-QGS-98-1001**, 1998

[37] S. U. Chung *et al.*, *Evidence of Exotic J^{PC} Meson Production in the Reaction $\pi^- p \to \eta\pi^- p$ at* $18\,GeV/c$, Phys. Rev. D **60:92001**, 1999

[38] S. U. Chung *et al.*, *Exotic and $q\bar{q}$ Resonances in the $\pi^+\pi^-\pi^-$ System Produced in $\pi^- p$ Collisions at* $18\,GeV/c$, Phys. Rev. D **65:072001**, 2002

[39] R. Clark *et al.*, The Hall D Collaboration, *Hall D Conceptual Design Report*, 2nd Ed., 2003

[40] F. E. Close and P. R. Page, *The Production and Decay of Hybrid Mesons by Flux Tube Breaking*, Nucl. Phys. B **443:233**, 1995

[41] G. T. Condo *et al.*, *Charge-Exchange Photoproduction of the $a_2^-(1320)$ in Association with Δ^{++} at* $19.3\,GeV/c$, Phys. Rev. D **41:3317**, 1990

[42] G. T. Condo *et al.*, *Photoproduction of an Isovector $\rho\pi$ State at* $1775\,MeV$, Phys. Rev. D **43:2787**, 1991

[43] G. Condo *et al.*, *Further Results from Charge-Exchange Photoproduction*, Phys. Rev. D **48:3045**, 1993

[44] H. Cramér, *Mathematical Methods of Statistics*, Princeton University Press, 1946

[45] J. P. Cummings and D. P. Weygand, *The New BNL Partial Wave Analysis Programs*, BNL Report **BNL-64637**, 1997

[46] J. P. Cummings and D. P. Weygand, *An Object-Oriented Approach to Partial Wave Analysis*, submitted to NIM A, arXiv:physics/0309052 v1, 2003

[47] D. Curry *et al.*, *Level One Trigger Monitor*, CLAS Note **00:002**, 2000

[48] M. Davier *et al.*, *The Reaction $\gamma p \to \pi^+\pi^-\pi^+\pi^- p$ at High-Energy and γ Dissociation into 4π*, Nucl. Phys. B **58:31**, 1973

[49] Robert T. Deck, *Kinematical Interpretation of the First πp Resonance*, Phys. Rev. Lett. **13:169**, 1964

[50] J. Donoghue, E. Golowich and B. Holstein, *Dynamics of the Standard Model*, Cambridge University Press, 1994

[51] V. Dorofeev, *The $J^{PC} = 1^{-+}$ Hunting Season at VES*, AIP Conf. Proc. **619:143**, 2002

[52] O. Dumbrajs *et al.*, *Compilation of Coupling Constants and Low-Energy Parameters. 1982 Edition*, Nucl. Phys. B **216:277**, 1983

[53] A. W. F. Edwards, *Likelihood, Expanded Edition*, The Johns Hopkins University Press, 1992

[54] Y. Eisenberg *et al.*, *Study of High-Energy Photoproduction with Positron-Annihilation Radiation. I. Three-Prong Events*, Phys. Rev. D **5:15**, 1972

[55] Paul M. Eugenio, *Search for New Mesons in the $\omega\eta$ and $\omega\pi^0$ Systems Produced in the Reaction $\pi^- p \to \pi^+\pi^- 4\gamma n$ at $18\,GeV/c$*, Ph.D. Dissertation, University of Massachusetts Amherst, 1998

[56] P. Eugenio *et al.*, *Observation of a New $J^{PC} = 1^{+-}$ Isoscaler State in the Reaction $\pi^- p \to \omega\eta n$ at $18\,GeV/c$*, Phys. Lett. B **497:190**, 2001

[57] R. P. Feynman, *Photon-Hadron Interactions*, Addison Wesley Longman, Inc., 1998

[58] M. Gell-Mann, *A Schematic Model of Baryons and Mesons*, Phys. Lett. **8:214**, 1964

[59] S. Godfrey and J. Napolitano, *Light Meson Spectroscopy*, Review of Modern Physics **71:1411**, 1999. Also available as hep-ph/981141.

[60] K. Hagiwara *et al.*, *Review of Particle Physics*, Phys. Rev. D **66:010001**, 2002

[61] Francis Halzen and Alan D. Martin, *Quarks & Leptons*, John Wiley & Sons, Inc., 1984

[62] D. J. Herndon *et al.*, *Generalized Isobar Model Formalism*, Phys. Rev. D **11:3165**, 1975

[63] F. von Hippel and C. Quigg, *Centrifugal-Barrier Effects in Resonance Partial Decay Widths, Shapes, and Production Amplitudes*, Phys. Rev. D **5:624**, 1972

[64] N. Isgur and J. Paton, *A Flux-Tube Model for Hadrons in QCD*, Phys. Rev. D **31:2910**, 1985

[65] E. Ivanov *et al.*, *Observation of Exotic Meson Production in the Reaction* $\pi^- p \to \eta' \pi^- p$ *at* $18\,Gev/c$, Phys. Lett. **86:3977**, 2001

[66] J. D. Jackson, *Remarks on the Phenomenological Analysis of Resonances*, Nuovo Cimento **34:1644**, 1964

[67] M. Jacob and G. C. Wick, *On the General Theory of Collisions for Particles with Spin*, Ann. Phys. **7:404**, 1959; Ann. Phys. **281:774**, 2000

[68] Y. Khokhlov, *Study of X(1600)* 1^{-+} *Hybrid*, Nucl. Phys. A **663&664:596c**, 2000

[69] J. Kogut and L. Susskind, *Vacuum Polarization and the Absence of Free Quarks in Four Dimensions*, Phys. Rev. D **9:3501**, 1974

[70] R. Kokoski and N. Isgur, *Meson Decays by Flux Tube Breaking*, Phys. Rev. D **35:907**, 1987

[71] J. Kuhn, *An Analysis of the* $\eta\pi^-\pi^-\pi^+ p$ *Final State Produced in the Reaction* $\pi^- p \to \eta\pi^-\pi^-\pi^+ p$ *at* $18\,GeV/c$, Ph.D. Dissertation, Rensselaer Polytechnic Institute, 2000

[72] D. Lawrence and M. Mestayer, *CLAS Drift Chamber Calibration: Software and Procedures*, CLAS Note **99:018**, 1999

[73] J. H. Lee *et al.*, *Spin-Parity Analysis of the* $f_1(1285)\pi^-$ *System in the reaction* $\pi^- p \to f_1(1285)\pi^- p$ *at* $18\,GeV/c$, Phys. Lett. B **323:227**, 1994

[74] J. Li, *The New Tagger Calibration Program*, CLAS Note **03:004**, 2003

[75] M. Lu, *Exotic Mesons in the* $\omega\pi^-\pi^0$ *System Produced in* $\pi^- p$ *Interactions at* $18\,GeV/c$, Ph.D. Dissertation, Rensselaer Polytechnic Institute, 2003

[76] Louis Lyons, *Statistics for Nuclear and Particle Physicists*, Cambridge University Press, 1999

[77] S. K. Matthews *et al.*, *A Composite Thin Vacuum Window for the CLAS Photon Tagger at Jefferson Lab*, NIM A **421:23**, 1999

[78] J. Merlin and J. Paton, *Spin Interactions in the Flux-Tube Model and Hybrid Meson Masses*, Phys. Rev. D **35:1668**, 1987

[79] M. Mestayer *et al.*, *The CLAS Drift Chamber System*, NIM A **449:81**, 2000

[80] Jay Orear, *Notes on Statistics for Physicists, Revised*, $http://nedwww.ipac.caltech.edu/level5/Sept01/Orear/Orear_contents.html$, 2001

[81] P. R. Page *et al.*, *Hybrid Meson Decay Phenomenology*, Phys. Rev. D **59:034016**, 1999

[82] Donald H. Perkins, *Introduction to High Energy Physics*, 4th Ed., Cambridge University Press, 1999

[83] Martin L. Perl, *High Energy Hadron Physics*, John Wiley & Sons, Inc., 1974

[84] H. Pilkuhn, *The Interactions of Hadrons*, North-Holland publishing Co., 1967

[85] L. M. Qin *et al.*, *Prototype Studies and Design Considerations for the CLAS Region 2 Drift Chambers*, NIM A **411:265**, 1998

[86] Byron P. Roe, *Probability and Statistics in Experimental Physics*, Springer, 1998

[87] C. W. Salgado, *Photon Trigger*, CLAS Internal Technical Note, 2001

[88] E. S. Smith *et al.*, *The Time-Of-Flight System for CLAS*, NIM A **432:265**, 1999

[89] E. S. Smith *et al.*, *Calibration of the CLAS TOF System*, CLAS Note **99:011**, 1999

[90] D. I. Sober *et al.*, *The Bremsstrahlung Tagged Photon Beam in Hall B at JLab*, NIM A **440:263**, 2000

[91] S. Taylor *et al.*, *The CLAS Start Counter*, NIM A **462:484**, 2001

[92] F. Viron, *Some Decay Modes of* 1^{-+} *Hybrid Mesons*, Phys. Rev. Lett. **53:2207**, 1984

[93] S. Zhu, *The Masses and Decay Widths of the Heavy Hybrid Mesons*, arxiv:hep-ph/9812405 v3, 1999

[94] S. Zhu, *Some Decay Modes of* 1^{-+} *Hybrid Meson in QCD Sum Rule Revisited*, Phys. Rev. D **60:097502**, 1999

[95] G. Zweig, *An SU3 Model for Strong Interaction Symmetry and its Breaking II*, CERN Report **8419/TH:412**, 1964

[96] *CEBAF Hall B Conceptual Design Report*, 1990

[97] *Minuit Manual*, CERN Program Library Long Writeup **D506**, 1992

APPENDIX A

Reflectivity Basis and Rank Considerations

It is customary to use the spin density matrix, denoted by ρ, in the study of the production of resonances. The reflectivity basis is one of the parametrizations which diagonalizes ρ and guarantees the symmetries imposed by parity conservation in the production process.

Consider the reaction

$$\gamma p \to Rp' \tag{A.1}$$

We choose the Gottfried-Jackson(GJ)[27] frame as the reference frame for convenience. The reflection operator is defined as [34]:

$$\Pi_y = e^{-i\pi J_y}\Pi \tag{A.2}$$

where Π is the parity operator. Particles with spin usually are not in reflectivity eigenstates. However, we can construct a reflectivity eigenstate from an angular momentum eigenstate $|\alpha m\rangle$ for R as,

$$|\epsilon\alpha m\rangle = [|\alpha m\rangle - \epsilon P(-)^{J-m}|\alpha - m\rangle]\Theta(m) \tag{A.3}$$

$$\Theta(m) = \begin{cases} \frac{1}{\sqrt{2}} & m > 0 \\ \frac{1}{2} & m = 0 \\ 0 & m < 0 \end{cases}$$

where α collectively stands for quantum numbers such as J^{PC}, etc., P is the intrinsic parity of R and $m = |J_z|$ is the absolute value of the spin projection, such that

$$\Pi_y|\epsilon\alpha m\rangle = \epsilon(-)^{2J}|\epsilon\alpha m\rangle \tag{A.4}$$

[27]The Gottfried-Jackson frame is defined in the rest frame of the resonance(R). In which the z axis is along the direction of the incident particle and the y axis is normal to the production plane.

$$\epsilon = \begin{cases} \pm 1 & \text{for bosons} \\ \pm i & \text{for fermions} \end{cases}$$

The intensity distribution can be written as[28]

$$I(\tau) \propto \sum_{\epsilon} \sum_{\substack{k \\ (\lambda_\gamma \lambda_p \lambda_{p'})}} \left| \sum_{\alpha m} \langle \epsilon \alpha m,\, \vec{p}_{p'} \lambda_{p'} | T^J | \vec{p}_\gamma \lambda_\gamma,\, \vec{p}_p \lambda_p \rangle A^\alpha_m(\tau) \right|^2 \tag{A.5}$$

where $A^\alpha_m(\tau)$ is the decay amplitude of R and T^J is the transition operator. For strong and electromagnetic interactions, T^J is reflection invariant,

$$T^J = \Pi_y^{-1} T^J \Pi_y \tag{A.6}$$

Let ${}^\epsilon V^k_{\alpha m}$ denote the production amplitude times a decay constant where k labels the helicities as indicated in equation A.5

$${}^\epsilon V^k_{\alpha m} = \langle \epsilon \alpha m,\, \vec{p}_{p'} \lambda_{p'} | T^J | \vec{p}_\gamma \lambda_\gamma,\, \vec{p}_p \lambda_p \rangle \tag{A.7}$$

Inserting A.6 in A.7, and considering the transformation property of a single particle helicity state under the reflection operation [67],

$$\Pi_y | \vec{p} s \lambda \rangle = P(-)^{s-\lambda} | \vec{p} s \lambda \rangle \tag{A.8}$$

where P is the intrinsic parity, s is the spin and λ is the helicity of the particle under investigation, we obtain

$${}^\epsilon V^{-k}_{\alpha m} = \epsilon^* P_\gamma P_p P_{p'} (-)^{s_\gamma - \lambda_\gamma + s_p - \lambda_p + s_{p'} - \lambda_{p'}} {}^\epsilon V^k_{\alpha m} \tag{A.9}$$

which can be readily reduced to

$${}^\epsilon V^{-k}_{\alpha m} = -\epsilon (-)^{\lambda_\gamma + \lambda_p + \lambda_{p'}} {}^\epsilon V^k_{\alpha m} \tag{A.10}$$

[28] Here we adopted the isobar model which allows us to separate the production from the decay of R.

For positive reflectivity, $\epsilon = +1$, we then have(± 1 denotes the sign of the helicity)

$$
\begin{aligned}
{}^{1}V_{\alpha m}^{-1-1-1} &= -\,{}^{1}V_{\alpha m}^{111} \\
{}^{1}V_{\alpha m}^{-1-11} &= +\,{}^{1}V_{\alpha m}^{11-1} \\
{}^{1}V_{\alpha m}^{-11-1} &= +\,{}^{1}V_{\alpha m}^{1-11} \\
{}^{1}V_{\alpha m}^{-111} &= -\,{}^{1}V_{\alpha m}^{1-1-1}
\end{aligned}
$$

For negative reflectivity, $\epsilon = -1$, we have

$$
\begin{aligned}
{}^{1}V_{\alpha m}^{-1-1-1} &= +\,{}^{1}V_{\alpha m}^{111} \\
{}^{1}V_{\alpha m}^{-1-11} &= -\,{}^{1}V_{\alpha m}^{11-1} \\
{}^{1}V_{\alpha m}^{-11-1} &= -\,{}^{1}V_{\alpha m}^{1-11} \\
{}^{1}V_{\alpha m}^{-111} &= +\,{}^{1}V_{\alpha m}^{1-1-1}
\end{aligned}
$$

The spin density matrix ${}^{\epsilon}\rho_{mm'}^{\alpha\alpha'}$ now takes block diagonal form [34],

$$
{}^{\epsilon}\rho = \begin{pmatrix} {}^{+}\rho & 0 \\ 0 & {}^{-}\rho \end{pmatrix} \tag{A.11}
$$

and states of different reflectivities do not interfere with each other.

APPENDIX B
Reference Frames

The sequential decay of a resonance R into three pions,

$$R \rightarrow Isobar + \pi \rightarrow \pi + \pi + \pi \tag{B.1}$$

can be described in terms of the following variables: $\Omega = (\theta, \phi)$ and $\Omega_h = (\theta_h, \phi_h)$. The first two variables, θ and ϕ, are the polar and azimuthal angles of the isobar in the R rest frame(RRF) respectively. The coordinate system in RRF is chosen to be that of the Gottfried-Jackson frame, i.e., the z-axis is along the beam direction and the y-axis is normal to the production plane, $\hat{y} = \vec{beam} \times \vec{target}$. The other two variables, θ_h and ϕ_h, are the polar and azimuthal angles of one of the isobar decay products in the isobar rest frame(IRF). The coordinate system in the IRF is oriented so that the direction of the isobar in the RRF defines the z_h-axis. The y_h-axis is normal to the decay plane of R defined by the directions of the beam and the isobar in the RRF, $\hat{y_h} = \hat{z} \times \hat{z_h}$. Both reference frames are completed by orienting the x-axis to form right-handed coordinate systems. A sketch of the reference frames is given in Figure B.

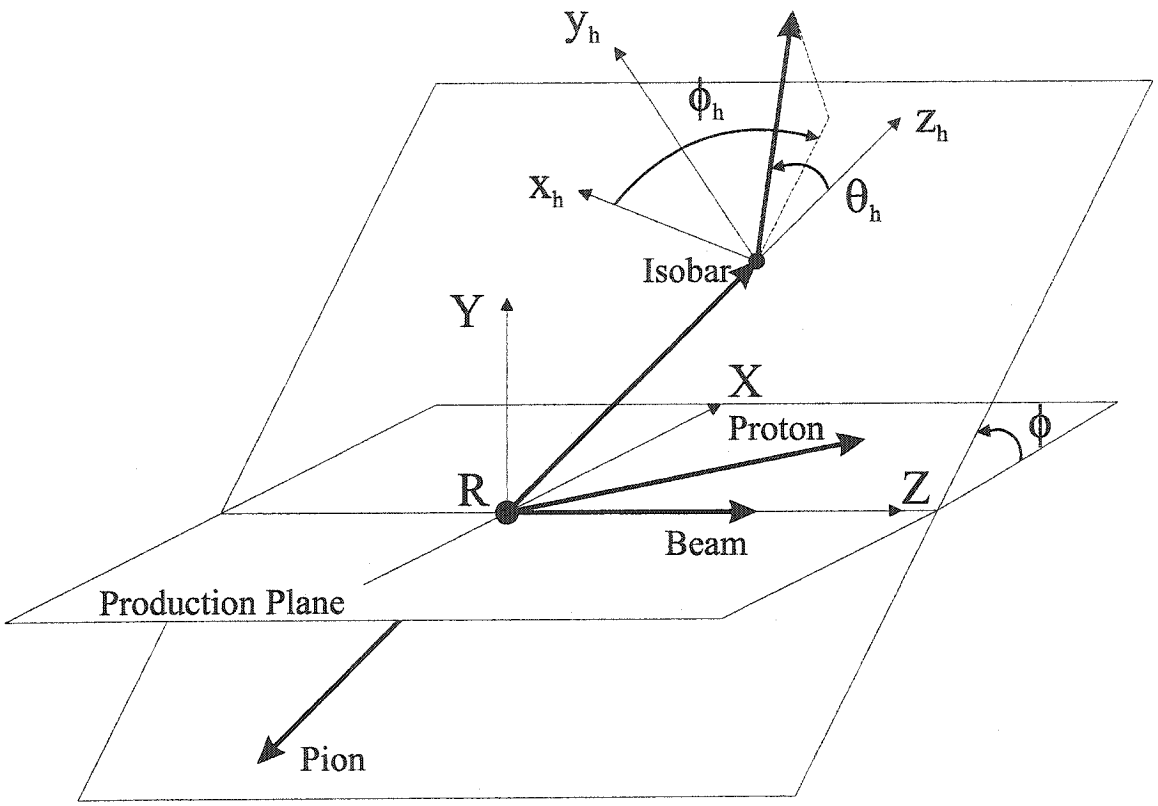

Figure B.1: The reference frames used to describe the sequential decay of a resonance R into three pions. The recoil proton lies in the XZ(production)-plane. The decay plane of the resonance R is defined by the beam and the isobar.

APPENDIX C
Extended Maximum Likelihood Method

We give an overview of the extended maximum likelihood method here following that of Orear [80].

Let $f(a;x)$ be an observed experimental distribution, where x is a set of observables and a is a parameter to be determined. Note that a can be discrete but is usually continuous, corresponding to an infinite set of physics hypotheses. The standard likelihood function, $\mathcal{L}(a)$, is defined as[29]

$$\mathcal{L}(a) = \prod_{i}^{N} f(a;x_i) \tag{C.1}$$

where N is the total number of observed experimental points. $\mathcal{L}(a)$ is the joint probability density of getting a particular experimental result x assuming $f(a;x)$ is the normalized distribution function[30],

$$\int_{x_{min}}^{x_{max}} f(a;x)dx = 1 \tag{C.2}$$

The most probable value of a corresponding to the maximum value of $\mathcal{L}(a)$ is called the maximum-likelihood solution a^*.

In the more general cases, there are M parameters, $a_1, ..., a_M$, to be determined. To obtain the set of maximum-likelihood solutions, a_j^*, one solves the M simultaneous equations:

$$\frac{\partial ln\mathcal{L}(a_1...a_M)}{\partial a_j}\Big|_{a_j=a_j^*} = 0 \tag{C.3}$$

It was shown by Cramér [44] that in the limit of large N, a^* converges to the true value a_0 and no other procedure of estimation can give a more accurate answer[31].

[29]Notice this equation as it stands is the probability density of observing our particular set of events *in this order*. There should be a $N!$ on the right hand side of the equation. However, since we are only interested in the relative ratio, a multiplicative constant is irrelevant.

[30]Proper normalization is essential here because otherwise one could arbitrarily increase a, and $\mathcal{L}(a)$ does not have absolute maximum anymore.

[31]This is the so-called *Maximum-Likelihood Theorem*

The extended maximum-likelihood method is a variant of the standard maximum-likelihood method. In the extended maximum-likelihood method our parameter list includes one additional parameter which measures the overall normalization. The extended likelihood function is thus constructed by putting together (i) the probability of observing a sample of N events and (ii) the probability that this sample of N events has the x-distribution:

$$\mathcal{L}(a) = \left(\frac{e^{-\bar{N}}\bar{N}^N}{N!}\right)\prod_i^N \frac{f(a;x_i)}{\int f(a;x)dx} \tag{C.4}$$

notice that the expected value of N is

$$\bar{N} = \int_{x_{min}}^{x_{max}} f(a;x)dx \tag{C.5}$$

dropping the factors that depend only on N,

$$\mathcal{L}(a) = e^{-\bar{N}}\prod_i^N f(a;x_i) \tag{C.6}$$